communications earth & environment

ARTICLE

https://doi.org/10.1038/s43247-022-00612-5 OPEN

Megashears and hydrothermalism at the Martian crustal dichotomy in Valles Marineris

Joanna Gurgurewicz [1✉], Daniel Mège [1], Frédéric Schmidt [2,3], Sylvain Douté [4] & Benoit Langlais [5]

Observations of ancient deep deformation systems on Mars are important for constraining planetary dynamics, as well as to identify potential mineral resources. However, such systems were thought to be unexposed and inaccessible to analysis. Here, we apply structural and hyperspectral analyses, and correlate results with magnetic anomaly patterns, to investigate two large right-lateral brittle-ductile shear zones and fault megabreccia exposed in the deepest parts of Valles Marineris. The shear zones follow the trace of the edge of the Borealis impact basin, thought to represent the planetary dichotomy boundary. We identify hydrothermally altered mafic igneous rocks in the sheared basement. We suggest that the shear system was initiated as basin ring fault system in the pre-Noachian, with further reactivation up until the Hesperian, and may still be a potential source of marsquakes. Hydrothermal circulation through the shear zones may have initiated primary mineralizations which are promising for base and rare metal exploration.

[1] Centrum Badań Kosmicznych Polskiej Akademii Nauk (CBK PAN), Bartycka 18A, 00-716 Warszawa, Poland. [2] Université Paris-Saclay, CNRS, GEOPS, 91405 Orsay, France. [3] Institut Universitaire de France (IUF), Paris, France. [4] Université Grenoble Alpes, CNRS, CNES, IPAG, 38000 Grenoble, France. [5] Nantes Université, Université d'Angers, Le Mans Université, CNRS, UMR 6112, Laboratoire de Planétologie et Géosciences, 44000 Nantes, France. ✉email: jgur@cbk.waw.pl

The Hesperian and Amazonian tectonics of Mars are well characterized owing to plentiful exposures. However, the pre-Noachian and Noachian rocks are obscured by extensive resurfacing in many regions. Where exposed, tectonics is seen to be locally complex[1,2] as expected from remote geochemistry and geophysics[3]. In this paper, we report on two large shear zones exposed in a deep erosional window that formed in the brittle-ductile domain of the crust early in Mars history and located in the area between the northern Valles Marineris trough system and the planetary dichotomy boundary (PDB).

The Valles Marineris trough system is exposed atop a broad topographic dome that is superimposed on the Tharsis rise[4]. The dome's large free-air gravity anomaly[5] is consistent with an upward flexural response of crust thickened between the Late Noachian and Early Hesperian. Trough nucleation[6,7] has been interpreted as the consequence of differential loading of the thickening Tharsis volcanic pile over the pre-existing step in basement topography that has been associated with the Borealis basin, which may have formed by an oblique impact event early in Mars history, probably around 4.5 Ga[4,8,9]. Extrusive volcanic activity associated with the early growth of Tharsis could have led to differential (north-south) loading of the crust across the PDB, producing a circumferential flexural uplift some 500–1000 km wide[4], growth of large-scale igneous dikes[6,10], dilational normal faulting[11,12], and subsidence of crustal blocks parallel to them[4,6,7]. During the Hesperian, the troughs were partly filled by the Interior Layered Deposits (ILD), consisting of sequences of sulfate-rich layers formed by chemical evolution in an acidic environment of atmospherically-deposited ice, dust, and sulfur-rich volcanics[13,14], leading to continued or renewed subsidence. The ILD were then locally eroded down by several kilometers. The reported shear zones are located in areas where ILD erosion attains ~6 km vertically. However, the exposed surface is not the surface of the Hesperian plateau. We show that it is a deeper crustal level in which complex deformation and intrusive activity is apparent, opening a window into the proto-Valles Marineris history.

Results and discussion

Identification of a basement unit in northern Valles Marineris. The deepest parts of eastern Ophir and Hebes Chasmata (Fig. 1) display complex terrains that have not been characterized before. These terrains are fully covered by MRO/HiRISE images. Mapping at the HiRISE scale (Fig. 1 and Supplementary Figs. 1, 2) reveals highly deformed light-toned rocks. Most of them form a massive unit, with fracture patterns reminiscent of crystalline rocks. This rock unit also contains dikes and other intrusions. The layering of distinct colors indicates that its composition is not uniform, and suggests mechanical contrasts that may influence the deformation style. Although generally light-toned, the morphology of these rocks is distinct from that of the nearby ILD, also light-toned. Supplementary Figs. 3–7 illustrate this diversity of terrains. These terrains were not identified in earlier geologic maps of Valles Marineris, in which they were attributed to Amazonian landslide-related or other surficial processes (see Supplementary Discussion).

Nonlinear unmixing[15] of hyperspectral data from MRO/CRISM (see Methods section) applied to three regions of interest (ROI) where the basement rock is well exposed (see Supplementary Methods and Supplementary Data 1 [16]) shows that the rock is mafic and contains olivine, pyroxenes, and plagioclases, associated with various sulfates (Fig. 2). It gives a primary rock composition similar to one of the bright rocks exposed in other places of Valles Marineris[17] and at the outer Hellas impact ring structure[18]. Should the retrieved primary mineral abundances from the analyzed CRISM data be representative of the exposed rock, from conventional igneous rock nomenclature, it would be of olivine-gabbronorite (ROI1) or troctolite (ROI2 and ROI3) composition. In that case, the primary mineral assemblage gives a magmatic origin, with copiapite, jarosite, and szomolnokite additionally suggesting hydrothermal alteration of sulfides. A similar assemblage of sulfates found in

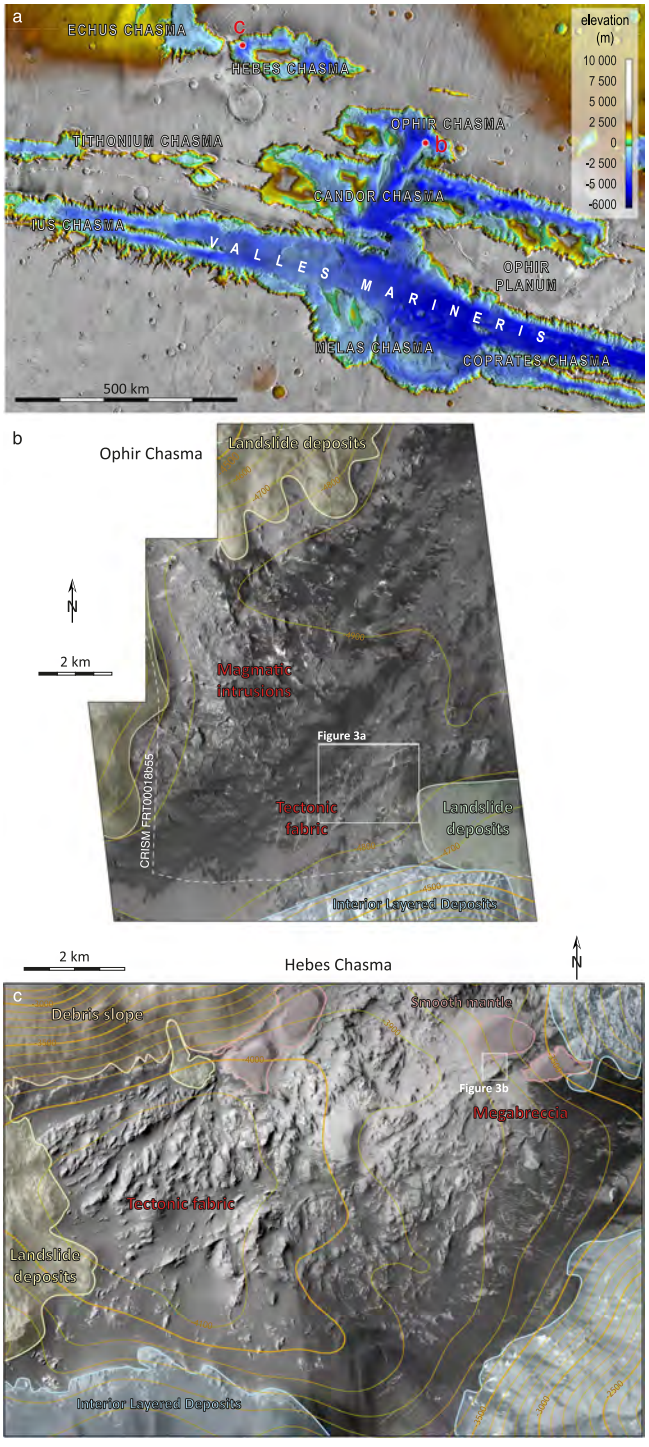

Fig. 1 Location map and interpreted CTX mosaic[91] of the two study areas in Valles Marineris. a Location map: THEMIS Day IR Global Mosaic[92] merged with the 128 ppd MOLA digital terrain model[93]. The white dashed line indicates a continuation of the Hebes tectonic fabric as a graben system onto the plateau above the chasma. **b** Interpreted CTX mosaic[91] of Ophir Chasma. **c** Interpreted CTX mosaic[91] of Hebes Chasma. The topographic information (contours, in meters) in (**b**) and (**c**) is extracted from an HRSC topographic mosaic of Valles Marineris (credit: ESA/DLR/Freie Univ. Berlin).

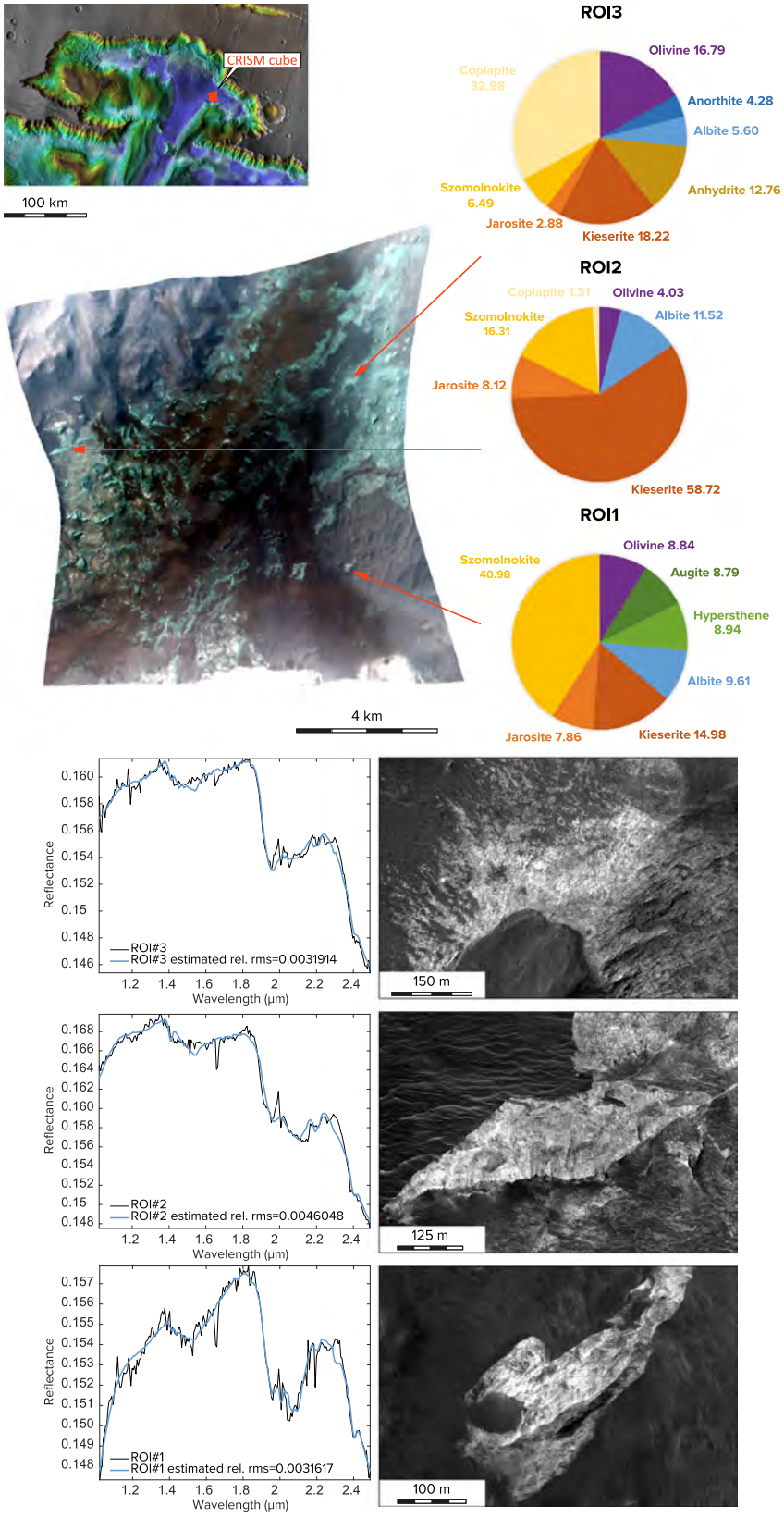

Fig. 2 Results of nonlinear spectral unmixing applied to the three selected regions of interest (ROI). Location of the three ROIs on CRISM image FRT00018b55 (bands R: 233, G: 78, B: 13), mineral relative abundances, the best fit plots with the relative RMS indicated, and corresponding HiRISE images of ROI1 (ESP_051999_1755_RED), ROI2 (ESP_039525_1755_RED), and ROI3 (ESP_039525_1755_COLOR). The result of a mixture containing pure albite and anorthite (ROI3) is interpreted as a plagioclase (albite-anorthite) solid solution. The same stands for the kieserite-szomolnokite solid solution. Credits: CRISM data: NASA/Johns Hopkins University Applied Physics Laboratory; HiRISE images: NASA/JPL/the University of Arizona. The background of the location map is THEMIS Day IR Global Mosaic[92] merged with the 128 ppd MOLA digital terrain model[93].

Noctis Labyrinthus was also interpreted as the result of hydrothermal activity[19]. Anhydrite, identified in veins in Gale crater[20] and interpreted as originating from basaltic rock weathering, could alternatively be of primary origin[21], storing magmatic sulfur prior to breaking down and releasing it to the hydrothermal sulfates[22]. Kieserite may come from the nearby ILD[23], either transported by wind, or present in some small ILD outliers on the chasma floor. The difference between the composition of ROI1 and ROI2-3 confirms that the exposed basement does not have a uniform composition; in fact, HiRISE image analysis suggests a larger diversity of rock types, as illustrated by vertical banding (Supplementary Fig. 7). Gabbronorite and troctolite composition, layering, and the presence of minerals coming from alteration of sulfides make a geological assemblage that characterizes some magmatic cumulates on Earth, e.g., at the Longwood Range in New Zealand[24].

The retrieved mineralogical composition is markedly distinct from the ILD composition[23]. Aside from compositional information, the thickness of the dikes, tens of meters, and the presence of other intrusive bodies at the surface also indicate that the observed surface is exhumed, with probable kilometers of crust removed by erosion prior to ILD deposition, like dikes of similar thickness exposed on terrestrial continental shields[7]. Chasma formation was therefore driven not only by tectonic extension, but also substantial erosion, that the upper Hesperian ILD age[25] constraints to not later than lower Hesperian. The age of the basement rocks themselves must be older, perhaps Noachian or pre-Noachian. Both in the Ophir and Hebes Chasmata, this basement is discontinuously exposed, partly blanketed by low albedo deposits, including mottled terrain, a smooth mantle of probably airfall origin, and dune fields (Supplementary Figs. 1–3). This generally smooth material, devoid of large impact craters, explains why earlier mappers considered it to be of the Amazonian age (see Supplementary Discussion).

Brittle-ductile shear zones and fault megabreccia in the basement unit. We now focus on the deformation affecting the light-toned, mafic basement unit underlying the dark mantle terrains. Structural analysis (Fig. 3 and Supplementary Figs. 1, 2) reveals S-C and S-C-C' structures that point to right-lateral kinematics, with the main shears (C) oriented N055E (Ophir) and N065E (Hebes). Their formation implies shearing in a brittle-ductile regime. In the Hebes shear zone, fractures having walls separated laterally by up to one hundred meters are observed on a HiRISE image. They contain rock fragments of longer dimensions, up to several tens of meters. HiRISE color information reveals at least two different rock compositions (greyish and yellowish). The fragments are incorporated into a bright matrix bounded by the fracture walls. We interpret them as a megabreccia that testifies to brittle deformation.

The minimum shear zone width is estimated to be ~1 km in Ophir Chasma and 3 to 3.5 km in Hebes Chasma (Fig. 1 and Supplementary Figs. 1, 2). Using scaling relationships to evaluate shear zone displacement from their measured width, and then shear zone length from displacement (see Methods section), displacements along these structures may range between a few tens to several hundreds of kilometers, implying, in turn, horizontal shear zone extents of several hundred to perhaps several thousand kilometers (Supplementary Fig. 8).

The relative timing of brittle and brittle-ductile deformation could not be determined from mapping. For instance, cross-cutting relationships between tectonic structures formed in the brittle field (e.g., megabreccia) and the ones formed in the brittle-ductile field (e.g., sigmoidal fabric), or evidence of tectonic structure reactivation, were not observed. However, none of these deformation patterns are seen to extend in the ILD nor on the plateau surrounding the troughs, indicating that they formed earlier than the Hesperian plateau surface and ILD[1]. The Hebes shear zone extends west and, to a lesser extent, north on the Hesperian plateau as a narrow graben system (Fig. 1a and Supplementary Fig. 9). It may suggest reactivation of the shear zone in extension over as much as ~900 km, up to Noctis Labyrinthus, after the deposition of the early Hesperian Tharsis volcanics.

The formation of brittle-ductile shear zones several kilometers below the current surface requires that the Martian crust was wet and weak, in agreement with several works (see Methods section). The available water sources may have included abundant

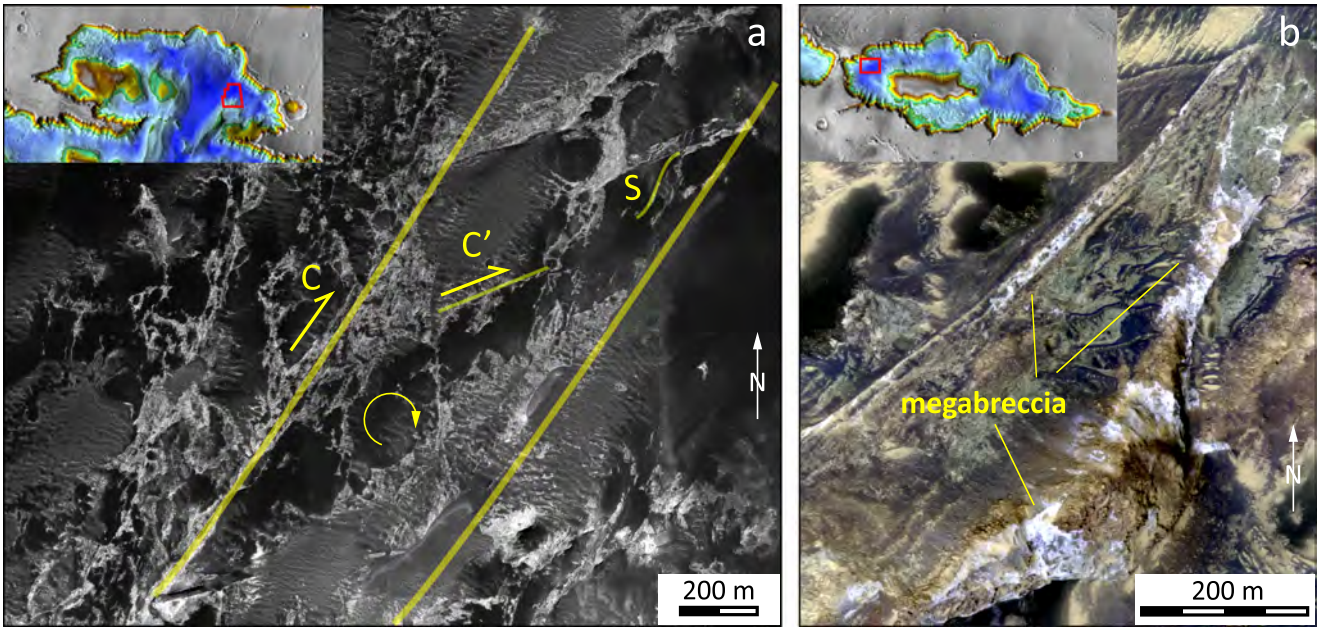

Fig. 3 Deformation patterns in the Ophir and Hebes shear zones. a Main exposure of the Ophir shear zone, highlighting S-C-C' structures indicative of brittle-ductile deformation (HiRISE image ESP_017754_1755). **b** Fault megabreccia exposed along the Hebes shear zone (HiRISE image ESP_040211_1790). Detailed structural mapping and context images are provided in Supplementary Figs. 1, 2. Credit: HiRISE images: NASA/JPL/the University of Arizona.

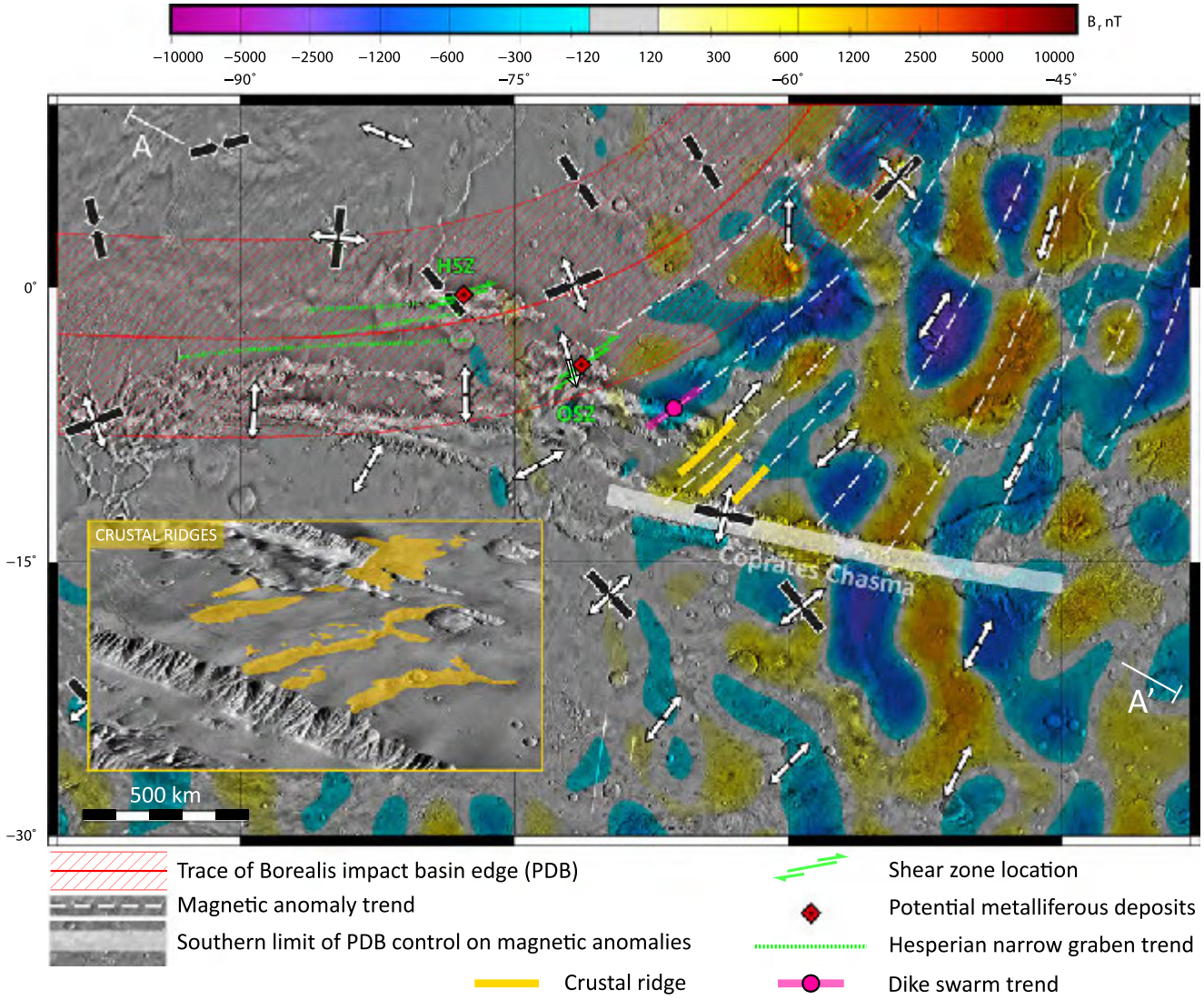

Fig. 4 The Ophir shear zone (OSZ) and Hebes shear zone (HSZ) in the context of the Planetary Dichotomy Boundary (PDB), the radial component of the magnetic anomaly at the surface, and some other tectonic elements. The trace of the Borealis impact basin, located with ±5° of uncertainty, is after Andrews-Hanna[4]. The shear zones and narrow grabens follow the PDB, and are interpreted as reactivated PDB ring structures. The OSZ extends northeastwards between magnetic anomalies of opposite polarity. The circumferential linear magnetic lineations are interpreted as hydrothermal transformation of additional magma-intruded ring structures. Crustal ridges and a NE-trending dike swarm are parallel to magnetic anomalies. The inset shows a 3D view of the largest ridges, the pre-Noachian to early Noachian, in which they are observed in orange. Additional analysis of these ridges and dike swarm is in Supplementary Fig. 12. A–A′ locates the magnetic profile shown in Supplementary Fig. 10. Arrows are simplified principal stress trajectory patterns from the thin-shell flexural model of Andrews-Hanna[4]; comprehensive results obtained in the study area are reproduced in Supplementary Fig. 13. White arrows indicate the tensile horizontal principal stress direction and large tensile stress magnitude. Black arrows indicate the most compressive horizontal principal stress direction and strongly negative tensile stress magnitude. Combined white and black arrows indicate weak tensile stress magnitude. The background is THEMIS Day IR Global Mosaic[92]; the topography is from HRSC (credit: ESA/DLR/Freie Univ. Berlin).

Noachian groundwater[26], crustal serpentinization in relation to PDB formation, then deserpentinization and water release to the surrounding rocks in response to the thermal events associated with the formation of early Tharsis[27], as well as juvenile water from Tharsis magmas. The heat advected by the fluids contributed to warm the surrounding crust, leading to a variable and locally steep thermal gradient during periods of active magmatism[28], perhaps generating crustal strength contrasts at local scales.

Shear zone significance. Our findings and the constraints they yield for an understanding of the evolution of the Valles Marineris region before the chasma opening are the following: (1) The shear zones are located near the PDB, and their trend is parallel (Hebes) or nearly parallel (Ophir) to it (Fig. 4). (2) The Hebes shear zone is associated with megabreccia in a bright matrix within thick fractures (Fig. 3c), and the Ophir shear zone basement unit includes megabreccia facies (Supplementary Figs. 4-6). (3) They are also located in the transitional area between the weakly magnetized lowlands crust in the north and the intensely magnetized highlands crust in the south, thought to mark the margin of the Borealis basin[29] (Fig. 4 and Supplementary Fig. 10). This transition was modified by Tharsis thermal events[30], which started in the Noachian after the Martian dynamo shut down, erasing most of the magnetization in the shear zone area (Supplementary Fig. 11). (4) The trend of the shear zones and the Borealis impact edge is parallel to the orientation of elongated

crustal magnetic anomalies north of Coprates Chasma (Fig. 4). It was inferred that the impact occurred around 4.5 Ga, while the early dynamo was active[31], strengthening the interpretation of a geological connection between them. (5) The westernmost radial magnetic anomalies north of Coprates Chasma are aligned with several crustal ridges of volcanic[25] or tectonic[17] origin up to 1 km high, formed in pre-Noachian to early Noachian terrain (Fig. 4). (6) Circumferential magnetic anomalies are observed around some impact craters and basins on Earth, where they result from the formation of magnetic minerals by impact-induced long-lasting hydrothermal activity[32,33]. (7) We note that the crustal ridges display channels restricted to the Noachian or pre-Noachian terrains, indicating water flows (Supplementary Fig. 12). The ridges also display surface fractures of similar, magnetic anomaly parallel orientation. (8) The NE-trending tectonic fabric is aligned with a NE-trending dike swarm on Candor Chasma walls (Fig. 4, Supplementary Figure 12), revealing intrusive magmatism along these magnetic anomalies. (9) Stress trajectories in the Valles Marineris region in response to PDB flexural loading by Tharsis using a thin-shell approach[4] are adapted to the tectonic deformation observed today. In spite of its simplicity (rock failure, friction, and long-term crustal viscous relaxation, are not taken into account), the model yields several major results. Tensile deviatoric stress is predicted to be high in the crustal portion of the Valles Marineris area between the PDB and Coprates Chasma. The tension axis is approximately parallel to the magnetic lineations (Fig. 4, with detailed analysis in Supplementary Fig. 13): the tectonic and magnetic fabrics are parallel. A major implication is that the magnetic anomaly patterns correspond to tectonic features. This inference is consistent with the observations made at the crustal ridges and the orientation of the Candor Chasma dike swarm. (10) In the Ophir and Hebes shear zone areas, the orientation of the principal stress trajectories in the flexural model[4] is in agreement with the observed right-lateral shear zone kinematics. The expected extensional regime is also consistent with an extension perpendicular to chasma orientation. (11) South of Coprates Chasma, the stress trajectories are no longer aligned with the magnetic anomalies, which perhaps indicates that magnetization is controlled by a crustal structure or composition distinct from those prevailing north of Coprates Chasma.

These elements suggest a model of crustal evolution in Valles Marineris until the opening of the main chasmata (Fig. 5). It explains not only the formation and kinematics of the shear zones, but also a series of geological features, the formation of which has remained elusive. They include the crustal ridges, the chasma-perpendicular dike swarm in Candor Chasma, the peculiar orientation of some narrow grabens between Syria Planum and Hebes Chasma, and the linear nature of magnetic anomalies north of Coprates Chasma.

The relationships between the shear zone, PDB, and anomalies are explained here by basin tectonics[34] applied to the Borealis basin. Formation of the Borealis basin at ~4.5 Ga generated circumferential normal faults filled with megabreccia, and crustal warming propagated from the molten crust in the impact area[9]. Hydrothermal circulation started along the fault pathways (Fig. 5a), mobilizing the water present in the crust, and perhaps also from the impactor. The megabreccia in the Ophir Chasma basement unit may have formed at that time, too, as an impact megabreccia, like the one interpreted around the Hellas basin[18], as well as the Candor Chasma dike swarm as an impact-related ring dike system.

The duration of hydrothermal activity was shorter than the duration of the dynamo (Fig. 5b). It is poorly constrained, but for a Hellas size impact basin, it was estimated to be in the order of 10 My[35]. Uncertainty arises from parameters such as post-impact crustal permeability and water abundance, as well as from the difficulty of modeling fine-scale processes in response to such a large-scale event. The four times larger Borealis basin size, based on gravity and topography[8], may have much lengthened the duration of hydrothermal activity. The dynamo activity lasted until 4.1 Ga or even later in the late Noachian[31], leaving at least 400 My for the hydrothermal activity to gradually stop and record the succession of polarity inversions while cooling to the Curie temperature.

The location and orientation of the Ophir and Hebes shear zones suggest that they may have been segments of ring normal faults. Similar to the other impact basins, many other ring faults should have fractured the crust in response to the impact. The observed elongated magnetic anomalies of alternating polarity may underline these structures. The hydrothermal minerals detected in the basement of the Ophir Chasma shear zone would therefore be the exposed equivalent to currently buried hydrothermal minerals that generated the observed magnetic anomalies.

In the late Noachian, adjustment of the Borealis basin load should have been achieved, through reactivation of the basin faults, decreasing the topographic difference between the highlands and lowlands (Fig. 5c). The geologic context of the Ophir and Hebes chasmata dramatically changed under the combined influence of the growth of the Tharsis load[36] and the major PDB crustal discontinuity. The flexural loading model of Tharsis over the PDB[4] predicts strike-slip reactivation along the basin ring structures in the Ophir and Hebes chasmata, resulting in the observed shear zones (Fig. 4).

The distinct tectonic domain south of Coprates Chasma is coherent with its interpretation as the northern limit of a major Hesperian and Noachian deformation system on the Thaumasia plateau and the Coprates rise[37]. These early Tharsis events may have deformed the crustal magnetic fabric, which would not reflect the orientation of the Borealis basin rim anymore.

The lower Hesperian marks the beginning of flood volcanism in the Tharsis region, specifically centered at Syria Planum[6,25]. The lava flows loaded the crust in the Valles Marineris region prior to the opening of the chasmata (Fig. 5d), with the consequence of increasing the vertical principal stress. Chasma opening by crustal extension may simply result from the permutation between the largest and intermediate principal stresses due to crustal loading by the lavas (Fig. 5d–f). Flood lava emplacement occurred via an intrusive system including a huge dike swarm[6] of mafic composition[38], partly cancelling crustal magnetization. New magnetization could have occurred upon dike cooling in response to the external or to the nearby crustal magnetic field. However, the external field is not stable and unlikely to produce consistent patterns all over the dikes. A new magnetization related to nearby magnetization would be much less intense than the original one and is unlikely to be detected from orbit.

The shear zones identified in the Ophir and Hebes chasmata can therefore be understood in a scenario in which an inherited crustal fabric is reactivated (Fig. 5f, stage 1), additional crustal loading increases the differential stress (stage 2), ending up with nucleation of the main chasma faults in tension (stage 3). The edge of the Borealis basin west of Hebes Chasma is nearly parallel to the Valles Marineris chasmata, which explains why the Hebes shear zone was there reactivated in tension, forming some narrow grabens.

It is apparent from this geological context that the hydrothermal activity identified in the Ophir and Hebes shear zone basement may have been widespread. Coprates Chasma, as a major tectonic and magnetic boundary, may represent the southern end of this hydrothermal system in the highlands crust.

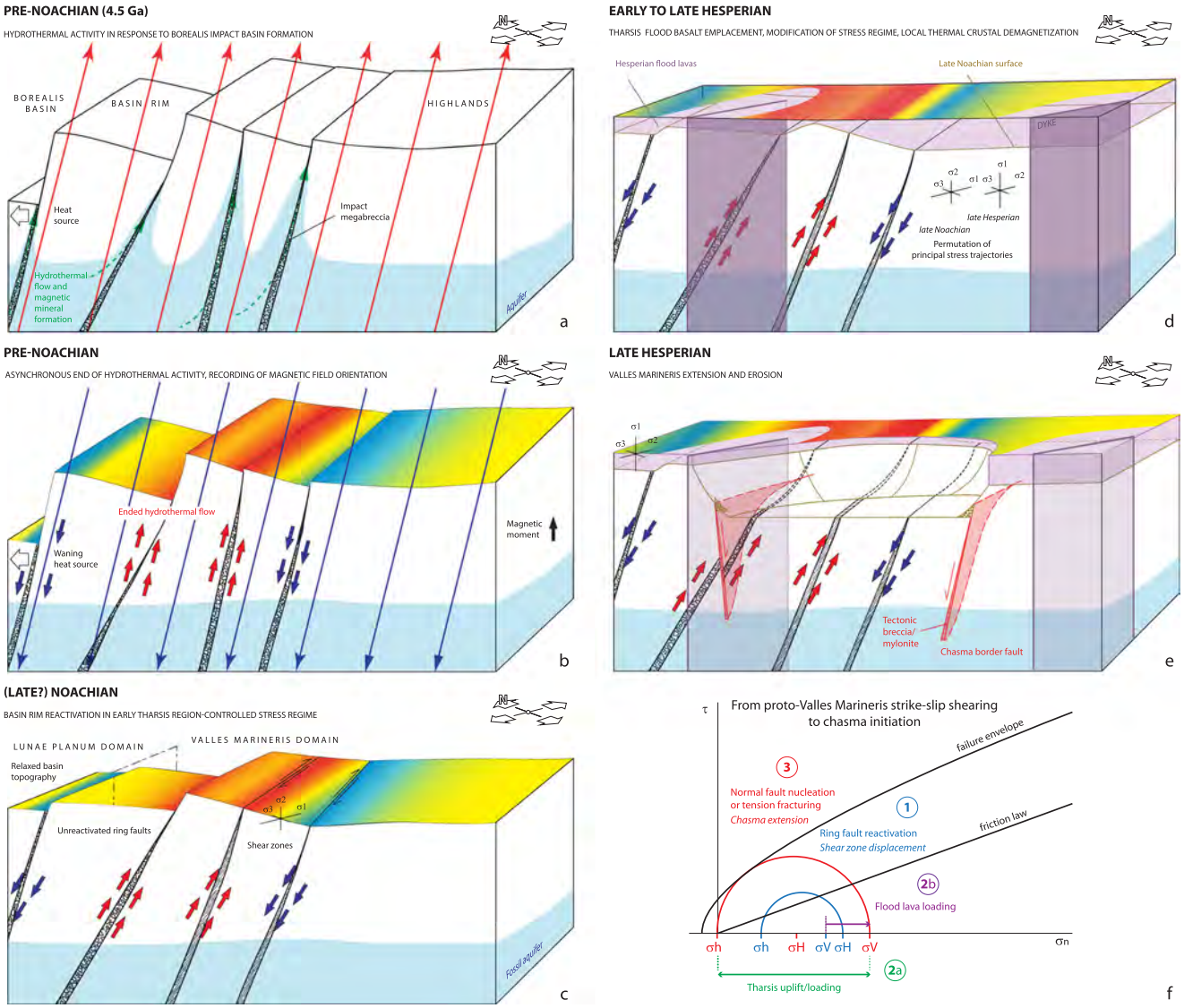

Fig. 5 Proposed scenario of the evolution of the Valles Marineris crust. a–e Crustal evolution stages. **f** Pre-Noachian to Hesperian evolution of stress state and brittle deformation of the Valles Marineris crust in response to Tharsis thermal events.

Evidence of hydrothermal activity at the PDB in the Valles Marineris region suggests that the weak, 10 km thick crustal layer found at the InSight landing site[39], also located at the PDB area, might be a similarly altered mafic basement rock.

Brittle-ductile shear zones are one of the contexts where metalliferous mineralizations can be abundant. Our results show that the Ophir and Hebes shear zones are of exceptional, if not unique, interest to search for such mineralizations. Mesothermal gold deposits on Earth (30% of mined gold) are observed in secondary structures of exhumed brittle-ductile shear zones and their shallow extension to the surface[40]. Au is drained in terrestrial shear zones by hydrothermal fluids, and after a complex path, concentrates in cataclastic quartz veins[41]. The mineralogically expressed Au is associated with As- paragenesis of Sb, W, Bi, Mo, and Pb, and in the quartz veins, with Pb, Ag, and Cu.

Assuming that the primary minerals identified using CRISM reflect the full basement rock composition, the shear zones could be sites to prospect for Ti-V oxides, which are found in terrestrial gabbronorite–troctolite layered intrusions[42]. At different depth levels, stratabound Ni-Cu sulfides and chromite may have settled[43], as well as platinum-group minerals, especially including Pt, Pd, and Au[24]. Although the deep source of metals accumulating in the planetary crust is loosely constrained, the sheared, fluid-charged Noachian and pre-Noachian basement rocks, as well as the neighboring intrusions, may be the most favorable environments to discover such deposits.

The influence of the Borealis basin on the tectonics and hydrothermal activity in the Valles Marineris region, and the implications for mineralizations, open a wealth of new questions of global planetary interest. Did the crustal fabric imposed by the impact influence the evolution of the Tharsis crust in other areas? Did it play a role in the genesis of the large fracture zone that guided the NE-SW orientation of many volcanic edifices that formed on the Tharsis dome? At the opposite, the Tharsis-generated stress field was shown to control the stress system of the whole planet[44]. Did it reactivate other PDB-related structures? Are there other sites where PDB-related hydrothermal activity can be found? Can it be identified elsewhere, without the exceptional exposure conditions in Valles Marineris? The obliquity of the Borealis basin impactor[9] should have generated a crustal fracturing asymmetry[45], did it affect the distribution of basin-generated mineralizations? Hydrothermal minerals were detected in the Nili Fossae and Nilosyrtis highlands[46], next to the

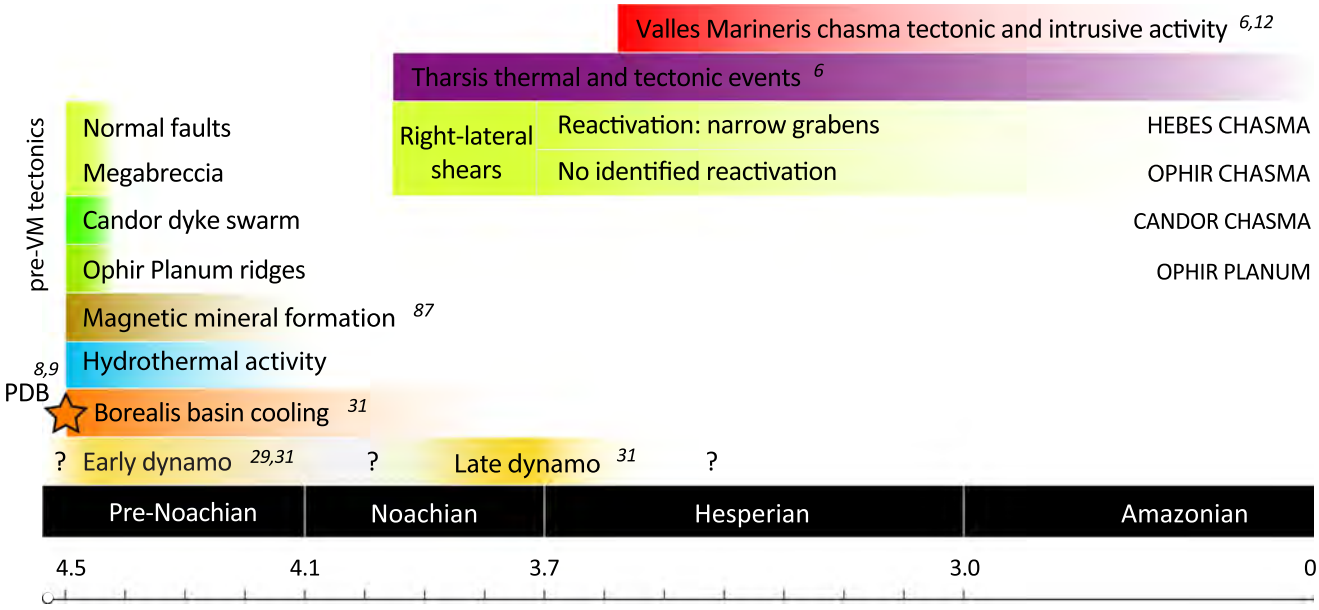

Fig. 6 Chronology of geodynamic and tectonic events in the Valles Marineris region. Large-scale post-Noachian tectonic activity at the shear zones is mainly restricted to the formation of narrow grabens, but as major crustal discontinuities, shear zone structures may have been occasionally active seismically until now. Numbers refer to the cited references.

PDB, which also display breccia ridges[47]. Do these features testify to PDB-related geologic events as well? Were the reactivated basin-related radial faults around the Hellas and Isidis basins[48] also prone to similar mineralizations? Finally, was the duration of hydrothermal activity associated with the Borealis basin long enough to stabilize the environmental conditions and favor the emergence of life? Radiogenic heating might have contributed to maintain a high geothermal gradient for some time[49], making the northern Valles Marineris a preferential region to investigate early life in situ.

Conclusions

Our results show that the influence of the Borealis impact on the later evolution of Mars may have been underestimated (Fig. 6). Large-scale shearing of the pre-Valles Marineris basement rock testifies to major crustal deformation unrecognized before that shall be taken into account in deciphering the early Mars' evolution. From a stress field point of view, this event is consistent with, and prefigures Valles Marineris opening, but does not prefigure the current Valles Marineris geometry. The shears probably initiated as normal faults at the time of the Borealis basin impact, as soon as ~4.5 Ga, the estimated age of the basin, while the early Martian dynamo was active[31]. This very long tectonic activity, combined with deep exhumation, the mafic composition of the sheared basement, and hydrothermal circulation, provide one of the most promising environments for lode deposition and concentration of metals, perhaps of cut-off grade.

The idea that deep faults such as from impact basins were the locus of hydrothermal activity and played a role in crustal magnetization[35,50] is also validated by our analysis. The recognition of early fluid-assisted deformation and identification of alteration products associated with early hydrothermal systems suggest that at least some fundamental Martian faults may have been rheologically weak, and, therefore, susceptible to reactivation and seismic activity, from early Noachian time and perhaps into the present in the current stress field, controlled by the Tharsis load[44]. If still reactivated nowadays, InSight should be able to detect it in a quiet seismic environment. The marsquake of August 25, 2021, measured by InSight in Valles Marineris, of body wave magnitude 4.1-4.2[51], is consistent with such a reactivation as much as the recognized deep chasma border faults[11,12,52]. The deep Valles Marineris troughs should be considered a high-priority target for innovative future exploration missions. It would enable a better understanding of the early Martian dynamics, as well as offer the grounds for in situ identification of rare resources.

Methods

Geologic mapping. Geologic analysis was fully conducted at the HiRISE scale (25 m pixel-1) in Ophir Chasma. In Hebes Chasma, only ~75% of the shear zone area is covered with HiRISE images. Gaps were filled with CTX images (6 m pixel-1). Conventional geologic mapping was conducted with an emphasis on structural analysis. Kinematic analysis of S-C fabric is from e.g., Platt and Vissers[53], following the nomenclature established by ref. [54], and as modeled by ref. [55]. Kinematic analysis of S-C-C' fabric is after ref. [56], who also provide a review of works on this fabric.

Generation of HiRISE DTM using photogrammetry and photoclinometry. Photoclinometry (or Shape-from-Shading, SfS) refers to the process of inferring 3D surface slopes from the intensity variations of a single shaded image. When combined with photogrammetry, as in ref. [57], SfS can be used to resolve 3D details from a given shaded image and merge it with the coarse 3D information inherited from an initial DEM. In this work, we apply the HDEM method[57,58] to HiRISE images (1 m pixel-1) based on HiRISE stereo-derived DEMs (3 m pixel-1), and with a coarse-to-fine strategy, to further refine the DEM results (1 m pixel-1). HDEM SfS takes a single image and a co-registered coarse DEM as inputs, and iteratively refines the coarse input DEM via the minimization of a total cost function. The total cost function comprises three terms. First, the image irradiance term expresses the goodness of fit between the observed image versus its modeling from surface slopes. This modeling combines a surface atmospheric radiative transfer scheme and a realistic spatially varying bidirectional reflectance distribution function. Second, we have the integrability constraint regularization term that connects slopes to the terrain height field. Third, the photogrammetry constraint regularization term ensures the inheritance of large scales from the initial photogrammetrically generated DEM in the refined version. In this work, the spatial BRDF model results from the linear mixing of two endmember terrains, mafic, and sulfate-rich, which spectrophotometric properties are extracted from a near-coincident CRISM multi-angular acquisition sequence (FRT, HRL, HRS, EPF) using the MARS-Reco method[59]. The HDEM numerical scheme is repeatedly executed until a pre-set maximum number of iterations is reached or until the total cost function for the image irradiance equation, integrability constraint, and photogrammetry constraint converges.

Determination of basement mineralogy. We analyzed each ROI with the LinMin algorithm[15], based on Primal-Dual Interior-Point Optimization[60]. This method assumes a linear mixture with positivity and sum-lower-than-one constraints:

$$\mathbf{Y} \sim \mathbf{A}.\mathbf{S} \text{ with } 0 < \mathbf{A} < 1 \text{ and } 0 < \Sigma\mathbf{A} < 1 \quad (1)$$

with **Y**, the ROI spectra, **A** the abundance (that are estimated), and **S** the end-member spectra (assumed to be known). The spectra **S** are from spectral libraries and have been measured in laboratory conditions, as described in Supplementary Methods. We also included flat and slope spectra, as described in ref. [15], to reduce the effect of aerosols and discrepancies between laboratory and remote sensing conditions (grain size, geometry, aerosols in the atmosphere).

In order to improve the fit, we also introduce a nonlinear unmixing based on the fact that grain size changes can be simply modeled by $\mathbf{S}\hat{}\mathbf{e} + \mathbf{C}$, with **e** an exponent factor, specific to each spectrum, and **C** a constant value. This new model can be formulated as:

$$\mathbf{Y} \sim \mathbf{A}.\mathbf{S}\hat{}\mathbf{e} \text{ with } 0 < \mathbf{A} < 1 \text{ and } 0 < \Sigma\mathbf{A} < 1 \quad (2)$$

We solved this problem using the Nelder-Mead Simplex Method[61] to estimate the optimum **e**, including the LinMin algorithm[15], by minimizing the reconstruction RMS. Unfortunately, this nonlinear procedure is much more computationally expensive than LinMin and not possible on a full CRISM cube. Nevertheless, for the ROI spectra selected for this work, this method is perfectly fitted. One has to note that retrieved abundances may differ from actual mineral abundance in the rock. Nevertheless, from the extensive experiments conducted, the detection of minerals from observed spectral features is robust. There is thus high confidence in the mineral assemblage for all ROIs.

A detailed description of the mineralogical analysis leading to the results presented in Fig. 2 is provided in Supplementary Methods. A synthesis of the mineral detections from spectral unmixing experiments is given in Supplementary Table 6. The spectral unmixing outputs are provided in Supplementary Data 1 [16] as plots and ASCII files.

Displacement scaling. Displacement scaling relates the width (w) or length (L) of tectonic structures (such as faults and shear zones) against their maximum displacement (D), along the whole range of rheological conditions in the crust. It is used as one of the tools to constrain the mechanical properties of the fractures and their host rock[62–65]. A broad agreement has been found over the years that for most tectonic structures, both (w) and (L) linearly scale with (D), irrespective of rock composition. However, from measurements reported in the literature, the possibility exists that for shear zones, D/L follows a power law, with an exponent of 1.5[65,66]. In displacement scaling, the size of datasets available in the literature is not large enough to infer statistics, and D/w and D/L scaling cannot be used to predict one of the three parameters from the others accurately. Here we use D/w and D/L plots to evaluate the order of magnitude of displacement at the Ophir and Hebes shear zones from the minimum measured width, inferred from the exposures, then to evaluate the order of magnitude of shear zone length, from the displacement.

In the first step, the width of the Ophir and Hebes shear zones are measured using the spacing major shears that bound the zone of most intense deformation on HiRISE images (see Supplementary Figs. 1 for the Ophir shear zone and 2 for the Hebes shear zone). In Ophir Chasma, the width of the exposed shear zone is 1 km. In Hebes Chasma, the width is between 3 ("Hebes1" in Supplementary Fig. 8) and 3.5 km ("Hebes2"). D/w scaling is done based on a dataset of shear zones of similar dimensions 60. We calculate the average D/w value for this dataset: 63, and assume that the same value applies to the Ophir and Hebes shear zones. One order of magnitude is added as a vertical error bar.

In the second step, this (D) range is used to evaluate the length of the shear zones. Three datasets for shear zones are available in the literature[62,66], among which a continental shear zone dataset is for shear zones of dimensions comparable to the Ophir and Hebes shear zones, which we use in this work[67]. We consider both linear (Supplementary Fig. 8b) and power law scaling with an exponent of 1.5[66,67] (Supplementary Fig. 8c). The average D/L for the continental shear zone dataset is 0.172. Assuming a linear relation between (D) and (L), the scaling line $D = 0.172\ L$ is used as a proxy for the Martian shear zones. Using the (D) range calculated earlier, a (L) range is calculated for the Ophir shear zone by projecting the (D) range along the scaling line. Two (L) ranges are calculated for the Hebes shear zone, corresponding to the 3 and 3.5 km measured widths. A horizontal error of one order of magnitude is attributed to the (L) ranges. As a second option, it is assumed that the continental shear zone dataset follows the power law of exponent 1.5. The (D) ranges are then projected onto this scaling line, and similarly, a horizontal bar of one order of magnitude is applied to the corresponding (L) range.

Determination of potential causes for brittle-ductile crustal deformation at shallow depth in Ophir and Hebes Chasmata. Although we know that wet rheology is more likely for Mars[68], we test it first with dry mafic (diabase) rheology. Assuming that deformation occurred at a depth equal to the current chasma floor depth, ~8500 m below the closest plateaus after MGS/MOLA data, the geothermal gradient required to generate brittle-ductile deformation would be 59–65 °C km^{-1}, assuming brittle-ductile behavior at the failure/creep transition temperature of 500–550 °C, depending on plagioclase abundance[69]. Another composition, such as olivine, or diorite[70] would only marginally change the conclusions. A quartz rheology[71] would make the brittle-ductile behavior even easier to reach, but is not considered here because of the mineralogical information provided by the CRISM data processing (Fig. 2).

Since the Hesperian lava pile covering the Valles Marineris plateau did not exist when the shear zones developed, and part of the floor depth was attained by tectonic stretching, the floor might have been much closer to the topographic surface, perhaps decreasing the required depth by two. This factor is considered as a maximum, because the Noachian pile is exposed at the plateau level at the same elevation as the Hesperian lava pile 430 km away from the Ophir shear zone, at the eastern edge of Candor Chasma[25], with no major change of stratigraphic levels reported along the chasma walls between eastern Candor Chasma and eastern Ophir Chasma. Increasing the required geothermal gradient accordingly yields 120 °C km-1. This value is 5–10 times the average gradient calculated in the Martian highlands during Noachian[72–75] and for the Hesperian extensional deformation observed around Tharsis[76], and four times the gradient found during Noachian rifting south of Valles Marineris, at Thaumasia Planum, up to 33 °C km-1[77]. However, it was suggested recently that radiogenic heating[78] may also have participated in substantially increasing the thermal gradient during the Noachian[49].

The temperatures of 500–550 °C required to make diabase flow may actually not be needed, implying that very high thermal gradients may not be required. There is multiple evidence that crustal strength on terrestrial continents does not exceed ~50 MPa, with ductile creep occurring already at 6 km depth[79]. Equivalently, viscous relaxation of impact basins indicates a weak lower crust, with moderate heat flow[80]. Assuming a mean terrestrial crustal density of 2.7 g cm^{-3}, the corresponding lithostatic pressure would normally be 158 MPa, implying stress reduction by a factor of 3 to 4. On Mars, assuming a basaltic crust of density of 2.9 g cm^{-3}, 50 MPa would be located at 4.7 km depth, and if reduced by 3–4, ductile creep would occur as shallow as 1.2–1.6 km below the surface.

The first reason for such a strength decrease is the presence of free water in the crust[71], which may be testified to by the CRISM detections of hydrated hydrothermal sulfates (szomolnokite and copiapite have respectively 1, and 20 molecules of water in their structure, and jarosite has three hydroxyl groups). The weakening effect of water is major whatever the creep regime, dislocation, or diffusion[81]. Even less than 0.1% of water[79] may decrease rock strength by a factor of 2 to 3[69]. Wet diabase[82,83] is therefore much weaker than dry diabase[69], but perhaps more importantly, the hydrothermal paths not only locally dramatically increase heat flow, but also their pervasive penetration in the crust has a substantial warming effect that adds to the background heat flow[84].

Water may originate from infiltration through Noachian runoff channels[85] as well as volcanic outgassing[86]. The water of metamorphic origin may also weaken the crust; in particular, the correspondence between the edge of the crust showing magnetic anomalies[29] and the geometry of the exposed shear zones (Fig. 4) suggests a genetic link. One of the explanations for crustal magnetization is serpentinization during the Noachian[27,87]. Serpentinization may have weakened the shear zone area in three possible ways. First, during the magnetization itself, mobilizing free water, and incorporating it into mafic minerals transformed to chrysotile[27,87], reducing crustal strength[88] and shifting the portion of the crust exposed in the shear zone areas from the brittle toward the ductile domain. Weakening may proceed to such a point that locally serpentinite may rise through fractures by diapirism[89], providing a potential explanation for intrusions mapped on Supplementary Figs. 1, 2, as an alternative to magmatic intrusions. In that case, the whole magnetized crust being serpentinized, the weak rheology of the shear zone is not an exception, the observation of brittle-ductile structures at this depth is made possible by the denudation of Valles Marineris in the eastern Ophir and western Hebes Chasmata. Secondly, shear zone area weakening may have occurred during the process of crustal serpentinization because the troughs are located near the edge of the Borealis basin, a crustal zone of density contrast where intense fluid circulation is expected to have occurred. The rheology of the shear zones in Valles Marineris would be another tectonic consequence of crustal magnetization. Thirdly, if the shear zones formed later than the crustal magnetization event, crustal weakening could have corresponded to crustal deserpentinization. For instance, under the effect of magmatic heat release at the earliest stages of the Tharsis-Syria Planum magmatic events by the end of Noachian or earliest Hesperian[6], water from chrysotile structure could have been releasing west of eastern Ophir Chasma. It is also possible that partial deserpentinization occurred owing to crustal heating from below, which would explain magnetization depth as shallow as 5–10 km[90]. Whatever the case, the magnetization of the Martian crust by serpentinization, or deserpentinization, is likely to have involved a substantial amount of water, up to 1 km of global equivalent layer[27], which should have contributed to weakening the rheology in the shear zone areas.

Finally, crustal rheology strongly depends on the strain rate; taking the viscous component of the Martian lithosphere rheology into account would decrease lithospheric strength and shallow the brittle-ductile transition depth[79].

In summary, a simple dry crustal rheology cannot explain the observation of brittle-ductile deformation in the Ophir and Hebes shear zones. Several mechanisms have been identified which may explain the formation of brittle-ductile structures at the observed paleo-depth. Crustal hydration is one, and it was noted that in addition to the dramatic and well-known effect of a very small quantity of free water on the rheology of the crust, for which there is evidence in

the Noachian, hydrothermal circulation may have multiplied the geothermal gradients by several times at the scale of the exposed shear zone outcrops, a few tens of km^2 in size. Structural water related to crustal serpentinization or deserpentinization (or other metamorphic reactions) may provide another source of rheological weakening, perhaps in connection with the initiation of the Tharsis-Syria Planum magmatism. All these processes are not exclusive, instead, they may have been added and combined, resulting in brittle-ductile deformation in Ophir and Hebes Chasmata.

Data availability

The HiRISE, CTX, CRISM, THEMIS, MOC, and Viking data were available from the NASA Planetary Data System at https://doi.org/10.17189/1520303, https://doi.org/10.17189/1520266, https://doi.org/10.17189/1519573, https://doi.org/10.17189/1520386, https://doi.org/10.17189/1520255, and https://doi.org/10.17189/1520333, respectively.

The HRSC digital terrain models are available from the ESA Planetary Science Archive (https://doi.org/10.1016/j.pss.2017.07.013).

The Supplementary Data 1 dataset is available in the following public repository: https://gitlab.dsi.universite-paris-saclay.fr/frederic.schmidt/linearunmixing/-/tree/main/results.

Code availability

The CRISM data processing code is available in the following public repository: https://gitlab.dsi.universite-paris-saclay.fr/frederic.schmidt/linearunmixing.

Received: 10 January 2022; Accepted: 1 November 2022;
Published online: 17 November 2022

References

1. Scott, D. H. & Tanaka, K. L. Map showing lava flows in the southeast part of the Amazonis Quadrangle of Mars. U.S. Geological Survey IMAP 1280, scale 1:2,000,000. https://doi.org/10.3133/i1280 (1981).
2. Tanaka, K. L. & Davis, P. A. Tectonic history of the Syria Planum province of Mars. *J. Geophys. Res. Solid Earth* **93**, 14893–14917 (1988).
3. Bouley, S. et al. A thick crustal block revealed by reconstructions of early Mars highlands. *Nat. Geosci.* **13**, 105–109 (2020).
4. Andrews-Hanna, J. C. The formation of Valles Marineris: 2. Stress focusing along the buried dichotomy boundary. *J. Geophys. Res. Planets* **117**, E03006 (2012).
5. Genova, A. et al. Seasonal and static gravity field of Mars from MGS, Mars Odyssey and MRO radio science. *Icarus* **272**, 228–245 (2016).
6. Mège, D. & Masson, P. A plume tectonics model for the Tharsis province, Mars. *Planet. Space Sci.* **44**, 1499–1546 (1996).
7. Ernst, R. E., Grosfils, E. B. & Mège, D. Giant dyke swarms on Earth, Venus and Mars. *Ann. Rev. Earth Planet. Sci.* **29**, 489–534 (2001).
8. Andrews-Hanna, J. C., Zuber, M. T. & Banerdt, W. B. The Borealis basin and the origin of the martian crustal dichotomy. *Nature* **453**, 1212–1215 (2008).
9. Marinova, M. M., Aharonson, O. & Apsphaug, E. Mega-impact formation of the Mars hemispheric dichotomy. *Nature* **453**, 1216–1219 (2008).
10. Mège, D., Cook, A. C., Garel, E., Lagabrielle, Y. & Cormier, M.-H. Volcanic rifting at Martian grabens. *J. Geophys. Res. Planets* **108**, 5044 (2003).
11. Schultz, R. A. Gradients in extension and strain at Valles Marineris, Mars. *Planet. Space Sci.* **43**, 1561–1566 (1995).
12. Mège, D. & Masson, P. Amounts of crustal stretching in Valles Marineris, Mars. *Planet. Space Sci.* **44**, 749–781 (1996).
13. Kite, E. S. et al. Evolution of major sedimentary mounds on Mars: Buildup via anticompensational stacking modulated by climate change. *J. Geophys. Res. Planets* **121**, 2282–2324 (2016).
14. Michalski, J. & Niles, P. Atmospheric origin of Martian interior layered deposits: links to climate change and the global sulfur cycle. *Geology* **40**, 419–422 (2012).
15. Schmidt, F. & Legendre, M. & Le Mouélic, S. Minerals detection for hyperspectral images using adapted linear unmixing: LinMin. *Icarus* **237**, 61–74 (2014).
16. Gurgurewicz, J., Mège, D., Schmidt, F., Douté, S. & Langlais, B. Supplementary Data 1. https://gitlab.dsi.universite-paris-saclay.fr/frederic.schmidt/linearunmixing/-/tree/main/results (2022).
17. Viviano-Beck, C. E., Murchie, S. L., Beck, A. W. & Dohm, J. M. Compositional and structural constraints on the geologic history of eastern Tharsis Rise, Mars. *Icarus* **284**, 43–58 (2017).
18. Rogers, A. D. & Nazarian, A. H. Evidence for Noachian flood volcanism in Noachis Terra, Mars, and the possible role of Hellas impact basin tectonics. *J. Geophys. Res. Planets* **118**, 1094–1113 (2013).
19. Thollot, P. et al. Most Mars minerals in a nutshell: various alteration phases formed in a single environment in Noctis Labyrinthus. *J. Geophys. Res. Planets* **117**, E00J06 (2012).
20. Rapin, W. et al. An interval of high salinity in ancient Gale crater lake on Mars. *Nat. Geosci.* **12**, 889–895 (2019).
21. Chambefort, I., Dilles, J. H. & Kent, A. J. R. Anhydrite-bearing andesite and dacite as a source for sulfur in magmatic-hydrothermal mineral deposits. *Geology* **36**, 719–722 (2008).
22. Hutchinson, M. C. & Dilles, J. H. Evidence for magmatic anhydrite in porphyry copper intrusions. *Econ. Geol* **114**, 143–152 (2019).
23. Roach, L. H. et al. Testing evidence of recent hydration state change in sulfates on Mars. *J. Geophys. Res. Planets* **114**, E00D02 (2009).
24. Ashley, P., Craw, D., MacKenzie, D., Rombouts, M. & Reay, A. Mafic and ultramafic rocks, and platinum mineralisation potential, in the Longwood Range, Southland, New Zealand. *N. Z. J. Geol. Geophys.* **55**, 3–19 (2012).
25. Witbeck, N. E., Tanaka, K. L. & Scott, D. H. Geologic map of the Valles Marineris region, Mars. U.S. Geological Survey Geologic Investigations Series, Map I–2010, scale 1:2,000,000. https://doi.org/10.3133/i2010 (1991).
26. Palumbo, A. M. & Head, J. W. Oceans on Mars: the possibility of a Noachian groundwater-fed ocean in a sub-freezing martian climate. *Icarus* **331**, 209–225 (2019).
27. Chassefière, E., Langlais, B., Quesnel, Y. & Leblanc, F. The fate of early Mars' lost water: The role of serpentinization. *J. Geophys. Res. Planets* **118**, 1123–1134 (2013).
28. Eppelbaum, L., Modelevsky, M. Jr & Pilchin, A. Geothermal investigations in the Dead Sea rift zone, Israel: implications for petroleum geology. *J. Pet. Geol.* **19**, 425–444 (1996).
29. Langlais, B., Thébault, E., Houliez, A., Purucker, M. E. & Lillis, R. J. A new model of the crustal magnetic field of Mars using MGS and MAVEN. *J. Geophys. Res. Planets* **124**, 1542–1569 (2019).
30. Lillis, R. J., Dufek, J., Bleacher, J. E. & Manga, M. Demagnetization of crust by magmatic intrusion near the Arsia Mons volcano: Magnetic and thermal implications for the development of the Tharsis province, Mars. *J. Volcanol. Geotherm. Res.* **185**, 123–138 (2009).
31. Mittelholz, A., Johnson, C. L., Feinberg, J. M., Langlais, B. & Phillips, R. J. Timing of the martian dynamo: new constraints for a core field 4.5 and 3.7 Ga ago. *Sci. Adv.* **6**, eaba0513 (2020).
32. Hawke, P. J., Buckingham, A. J. & Dentith, M. C. Modelling source depth and possible origin of magnetic anomalies associated with the Yallalie impact structure, Perth Basin, Western Australia. *Explor. Geophys.* **37**, 191–196 (2006).
33. Abramov, O. & Kring, D. A. Numerical modeling of impact-induced hydrothermal activity at the Chicxulub crater. *Meteorit. Planet. Sci* **42**, 93–112 (2007).
34. Melosh, H. J. *Planetary Surface Processes* (Cambridge Univ. Press, 2011).
35. Abramov, O. & Kring, D. A. Impact-induced hydrothermal activity on early Mars. *J. Geophys. Res.* **110**, E12S09 (2005).
36. Bouley, S. et al. Late Tharsis formation and implications for early Mars. *Nature* **531**, 344–347 (2016).
37. Dohm, J. M. & Tanaka, K. L. Geology of the Thaumasia region, Mars: plateau development, valley origins, and magmatic evolution. *Planet. Space Sci.* **47**, 411–431 (1999).
38. Flahaut et al. Pristine Noachian crust and key geologic transitions in the lower walls of Valles Marineris: Insights into early igneous processes on Mars. *Icarus* **221**, 420–435 (2012).
39. Knapmeyer-Endrun, B. et al. Thickness and structure of the martian crust from InSight seismic data. *Science* **373**, 438–443 (2021).
40. Jébrak, M. & Marcoux, E. *Geology of Mineral Resources* (Geological Association of Canada, 2015).
41. Bonnemaison, M. & Marcoux, E. Auriferous mineralization in some shear zones: a three-stage model of metallogenesis. *Miner. Depos.* **25**, 96–104 (1990).
42. Pirajno, F. & Hoatson, D. M. A review of Australia's Large Igneous Provinces and associated mineral systems: Implications for mantle dynamics through geological time. *Ore Geol. Rev.* **48**, 2–54 (2012).
43. Hoatson, D. M. Platinum-group element mineralisation in Australian Precambrian layered mafic-ultramafic intrusions. *AGSO J. Aust. Geol. Geophys.* **17**, 139–151 (1998).
44. Phillips, R. J. et al. Ancient geodynamics and global-scale hydrology on Mars. *Science* **291**, 2587–2591 (2001).
45. Tsikalas, F. in *Impact Tectonics* (eds Koeberl, K. & Henkel, H.) (Springer, 2005).
46. Viviano, C. E., Moersch, J. E. & McSween, H. Y. Implications for early hydrothermal environments on Mars through the spectral evidence for

carbonation and chloritization reactions in the Nili Fossae region. *J. Geophys. Res. Planets* **118**, 1858–1872 (2013).
47. Pascuzzo, A. C., Mustard, J. F., Kremer, C. H. & Ebinger, E. The formation of irregular polygonal ridge networks, Nili Fossae, Mars: implications for extensive subsurface channelized fluid flow in the Noachian. *Icarus* **319**, 852–868 (2019).
48. Öhman, T., Aittola, M., Kostama, V.-P. & Raitala, J. in *Impact Tectonics* (eds Koeberl, K. & Henkel, H.) (Springer, 2005).
49. Ojha, L., Karunitillake, S., Karimi, S. & Buffo, J. A magmatic hydrothermal systems on Mars from radiogenic heat. *Nat. Commun.* **12**, 1754 (2021).
50. Solomon, S. C. et al. New perspectives on ancient Mars. *Science* **407**, 1214–1220 (2005).
51. Horleston, A. C. et al. The far side of Mars: two distant marsquakes detected by InSight. *TSR* **2**, 88–99 (2022).
52. Andrews-Hanna, J. C. The formation of Valles Marineris: 1. Tectonic architecture and the relative roles of extension and subsidence. *J. Geophys. Res. Planets* **117**, E03006 (2012).
53. Platt, J. P. & Vissers, R. L. M. Extensional structures in anisotropic rocks. *J. Struct. Geol.* **2**, 397–410 (1980).
54. Lister, G. S. & Snoke, A. W. SC mylonites. *J. Struct. Geol.* **6**, 617–638 (1984).
55. Dennis, A. J. & Secor, D. T. A model for the development of crenulations in shear zones with applications from the Southern Appalachian Piedmont. *J. Struct. Geol.* **9**, 809–817 (1987).
56. Finch, M. A. et al. The ephemeral development of C′ shear bands: a numerical modelling approach. *J. Struct. Geol.* **139**, 104091 (2020).
57. Jiang, C., Douté, S., Luo, B. & Zhang, L. Fusion of photogrammetric and photoclinometric information for high-resolution DEMs from Mars in-orbit imagery. *ISPRS J. Photogramm. Remote Sens.* **130**, 418–430 (2017).
58. Douté, S. & Jiang, C. Small-scale topographical characterization of the Martian surface with in-orbit imagery. *IEEE Trans. Geosci. Remote Sens.* **58**, 447–460 (2020).
59. Ceamanos, X. et al. Surface reflectance of Mars observed by CRISM/MRO: 1. Multiangle approach for retrieval of surface reflectance from CRISM observations (MARS-ReCO). *J. Geophys. Res. Planets* **118**, 514–533 (2013).
60. Chouzenoux, E., Legendre, M., Moussaoui, S. & Idier, J. Fast constrained least squares spectral unmixing using primal-dual interior-point optimization. *IEEE J. Sel. Top. Appl. Earth Obs. Remote Sens.* **7**, 59–69 (2014).
61. Lagarias, J. C., Reeds, J. A., Wright, M. H. & Wright, P. E. Convergence properties of the Nelder-Mead simplex method in low dimensions. *SIAM J. Optim.* **9**, 112–147 (1998).
62. Fossen, H. *Structural Geology* (Cambridge Univ. Press, 2010).
63. Schultz, R. A. & Fossen, H. Displacement–length scaling in three dimensions: the importance of aspect ratio and application to deformation bands. *J. Struct. Geol.* **24**, 1389–1411 (2002).
64. Cowie, P. A. & Scholz, C. H. Physical explanation for the displacement-length relationship of faults using a post-yield fracture mechanics model. *J. Struct. Geol.* **14**, 1133–118 (1992).
65. Schultz, R. A. *Geological Fracture Mechanics* (Cambridge Univ. Press, 2019).
66. Fossen, H. & Cavalcante, G. C. G. Shear zones – A review. *Earth Sci. Rev.* **171**, 434–455 (2017).
67. MacMillan, R. A. The orientation and sense of displacement of strike-slip faults in continental Crust. Unpubl. thesis, Dept. of Geology, Carleton University, Ottawa, 73 pp. (1975), reproduced in Ranalli, G. Correlation between length and offset in strike-slip faults. *Tectonophysics* **37**, T1–T7 (1977).
68. Grott, M. & Breuer, D. The evolution of the martian elastic lithosphere and implications for crustal and mantle rheology. *Icarus* **193**, 503–515 (2008).
69. Mackwell, S. J., Zimmerman, M. E. & Kohlstedt, D. L. High-temperature deformation of dry diabase with application to tectonics on Venus. *J. Geophys. Res. Solid Earth* **103**, 975–984 (1998).
70. Burov, E. B. & Diament, M. The effective elastic thickness (T_e) of continental lithosphere: what does it really mean? *J. Geophys. Res. Solid Earth* **100**, 3905–3927 (1995).
71. Kohlstedt, D. L., Evans, B. & Mackwell, S. J. Strength of the lithosphere: constraints imposed by laboratory experiments. *J. Geophys. Res. Atmos.* **100**, 17587–17602 (1995).
72. Grott, M., Hauber, E., Werner, S. C., Kronberg, P. & Neukum, G. High heat flux on ancient Mars: Evidence from rift flank uplift at Coracis Fossae. *Geophys. Res. Lett.* **32**, L21201 (2005).
73. Ruiz, J., McGovern, P. J. & Tejero, R. The early thermal and magnetic state of the cratered highlands of Mars. *Earth Planet. Sci. Lett.* **241**, 2–10 (2006).
74. McGovern, P. J. et al. Localized gravity/topography admittance and correlation spectra on Mars: Implications for regional and global evolution. *J. Geophys. Res. Planets* **107**, 5136 (2002).
75. Karimi, S., Dombard, A. J., Buczkowski, D. L., Robbins, S. J. & Williams, R. M. Using the viscoelastic relaxation of large impact craters to study the thermal history of Mars. *Icarus* **272**, 102–113 (2016).
76. Solomon, S. C. & Head, J. W. Heterogeneities in the thickness of the elastic lithosphere of Mars: Constraints on heat flow and internal dynamics. *J. Geophys. Res. Solid Earth* **95**, 11073–11083 (1990).
77. Grott, M., Hauber, E., Werner, S. C., Kronberg, P. & Neukum, G. Mechanical modeling of thrust faults in the Thaumasia region, Mars, and implications for the Noachian heat flux. *Icarus* **186**, 517–526 (2007).
78. Brugger, J., Wülser, P.-A. & Foden, J. Genesis and preservation of a uranium-rich paleozoic epithermal system with a surface expression (Northern Flinders Ranges, South Australia): radiogenic heat driving regional hydrothermal circulation over geological timescales. *Astrobiology* **11**, 499–508 (2011).
79. Burov, E. in *Treatise on Geophysics* (ed. Schubert, G.) Ch. 6.03 (Elsevier, 2015).
80. Mohit, P. S. & Phillips, R. J. Viscous relaxation on early Mars: a study of ancient impact basins. *Geophys. Res. Lett.* **34**, L21204 (2007).
81. Karato, S.-I., Paterson, M. S. & FitzGerald, J. D. Rheology of synthetic olivine aggregates: Influence of grain size and water. *J. Geophys. Res. Solid Earth* **91**, 8151–8176 (1986).
82. Shelton, G. & Tullis, J. Experimental flow laws for crustal rocks. *Eos Trans. AGU* **62**, 396 (1981).
83. Caristan, Y. The transition from high temperature creep to fracture in Maryland diabase. *J. Geophys. Res. Solid Earth* **87**, 6781–6790 (1982).
84. Poort, J. & Klerkx, J. Absence of a regional surface thermal high in the Baikal rift; new insights from detailed contouring of heat flow anomalies. *Tectonophysics* **383**, 217–241 (2004).
85. Craddock, R. A. & Maxwell, T. A. Geomorphic evolution of the Martian highlands through ancient fluvial processes. *J. Geophys. Res. Planets* **98**, 3453–3468 (1993).
86. Grott, M., Morschhauser, A., Breuer, D. & Hauber, E. Volcanic outgassing of CO_2 and H_2O on Mars. *Earth Planet. Sci. Lett.* **308**, 391–400 (2011).
87. Quesnel, Y. et al. Serpentinization of the martian crust during Noachian. *Earth Planet. Sci. Lett.* **277**, 184–193 (2009).
88. Yamato, P. et al. Burial and exhumation in a subduction wedge: mutual constraints from thermomechanical modeling and natural P-T-t data (Schistes Lustrés, western Alps). *J. Geophys. Res. Solid Earth* **112**, B07410 (2007).
89. Polonia, A. et al. Lower plate serpentinite diapirism in the Calabrian Arc subduction complex. *Nat. Commun.* **8**, 2172 (2017).
90. Langlais, B., Purucker, M. E. & Mandea, M. Crustal magnetic field of Mars. *J. Geophys. Res. Planets* **109**, E02008 (2004).
91. Malin, M. C. et al. Context camera investigation on board the mars reconnaissance orbiter. *J. Geophys. Res. Planets* **112**, E05S04 (2007).
92. Christensen, P. R., Gorelick, N. S., Mehall, G. L. & Murray, K C. THEMIS public data releases, planetary data system node, Arizona State University. http://themis-data.asu.edu (2006).
93. Smith, D., Zuber, M. T., Neumann G. A. & Jester, P. Mars global surveyor laser altimeter precision experiment data record, NASA Planetary Data System, MGS-M-MOLA-3-PEDR-L1A-V1.0 (2003).

Acknowledgements

This work was funded by OPUS/V-MACS project no. 2015/17/B/ST10/03426 of the National Science Center, Poland, and the EXOMHYDR project. The EXOMHYDR project is carried out within the TEAM program of the Foundation for Polish Science, co-financed by the European Union under the European Regional Development Fund. F.S. and B.L. acknowledge support from the Institut National des Sciences de l'Univers (INSU), the Centre National de la Recherche Scientifique (CNRS), and the Centre National d'Etudes Spatiales (CNES) through the Program National de Planétologie. S.D. is grateful to the Centre National d'Etudes Spatiales (CNES) for supporting his CaSSIS and HiRISE related work through the Program "Exobiologie, protection planétaire et exoplanètes".

The authors are indebted to Richard A. Schultz (Orion Geomechanics LLC) for the suggestion to investigate the relationships between the shear zones in Valles Marineris and the Borealis basin, and for insightful discussions.

Author contributions

J.G. designed and coordinated the study, conducted the mineralogical analysis, contributed to the structural analysis, and wrote most of the manuscript. D.M. obtained the funding for this work, conducted the structural and geophysical analysis, contributed to the mineralogical analysis, and to manuscript writing. F.S. developed the spectral unmixing method and ran the code, and wrote the corresponding method. S.D. generated the HiRISE digital elevation model and wrote the corresponding method. B.L. provided the magnetic dataset, guided its interpretation, and contributed to manuscript writing.

Competing interests

The authors declare no competing interests.

Additional information

Supplementary information The online version contains supplementary material available at https://doi.org/10.1038/s43247-022-00612-5.

Correspondence and requests for materials should be addressed to Joanna Gurgurewicz.

Peer review information *Communications Earth & Environment* thanks Chris Okubo, Bob Myhill and the other, anonymous, reviewer(s) for their contribution to the peer review of this work. Primary Handling Editors: Claire Nichols, Joe Aslin. Peer reviewer reports are available.

Supplementary Figures

Supplementary Figure 1. Tectonic map of the eastern Ophir Chasma study area, and CTX basemap[1]. The two black and white crosses indicate what is considered as the minimum shear zone width (ca. 1 km). Younger deposits may hide other structures amenable to reevaluate this estimate. Credit: HiRISE images (detailed interpretations, insets A, B, C): NASA/JPL/University of Arizona.

Ophir Shear Zone
Tectonic Map

2021

North

Interpreted HiRISE images

ESP_016053_1755
ESP_017754_1755
ESP_039525_1755

1 km

-4500
-4600
-4700
-4800
-4900

A *and Figure 3b*

B

C

Landslide deposits

Interior layered deposits

Striated material (exhumed)

Basement rock

Dunes and textured ground

Thick grey mantle

Pitty grey mantle

Intrusive body or breccia/cataclasite/mylonite

Kinematic indicator, local

Kinematic indicator, regional

Major shear

Fracture

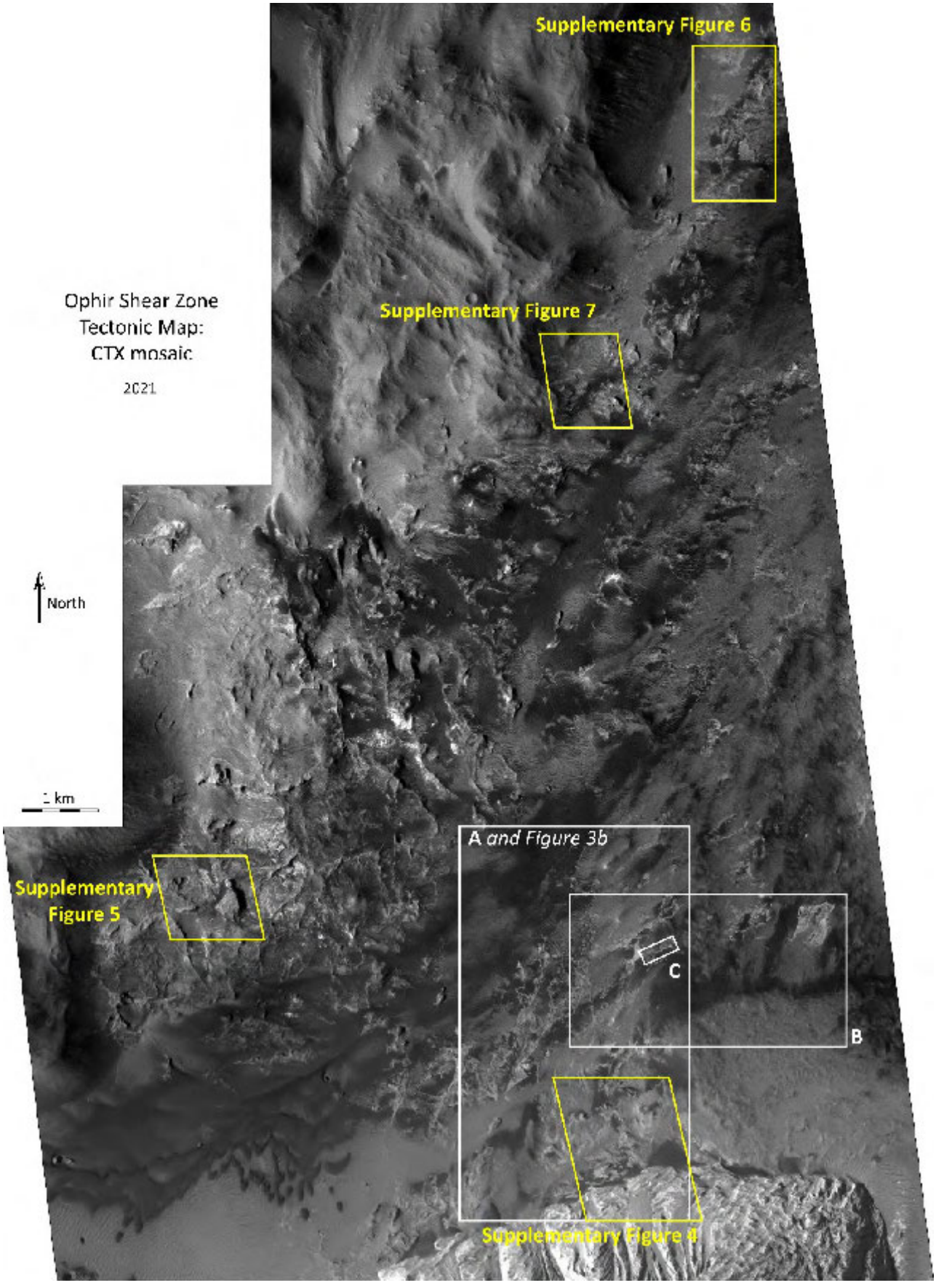
Supplementary Figure 6
Ophir Shear Zone
Tectonic Map:
CTX mosaic
2021
Supplementary Figure 7
North
1 km
A and Figure 3b
Supplementary Figure 5
C
B
Supplementary Figure 4

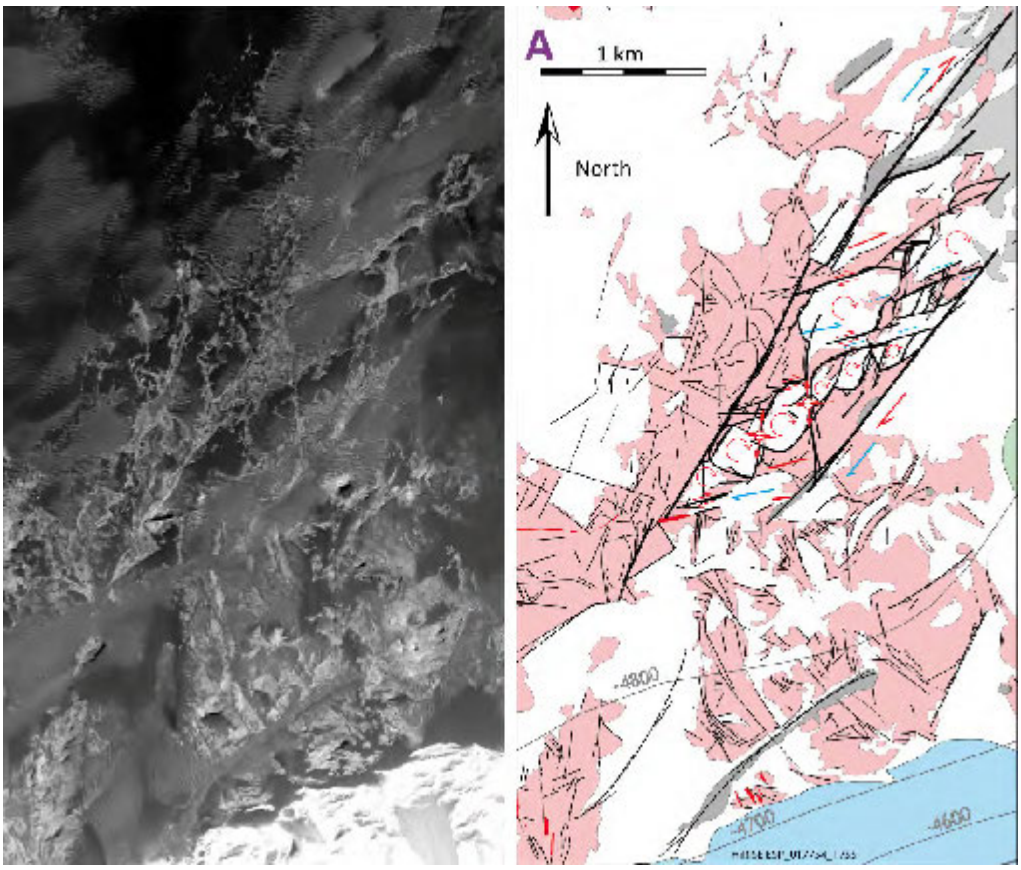
A
1 km
North
-4800
-4700
-4600

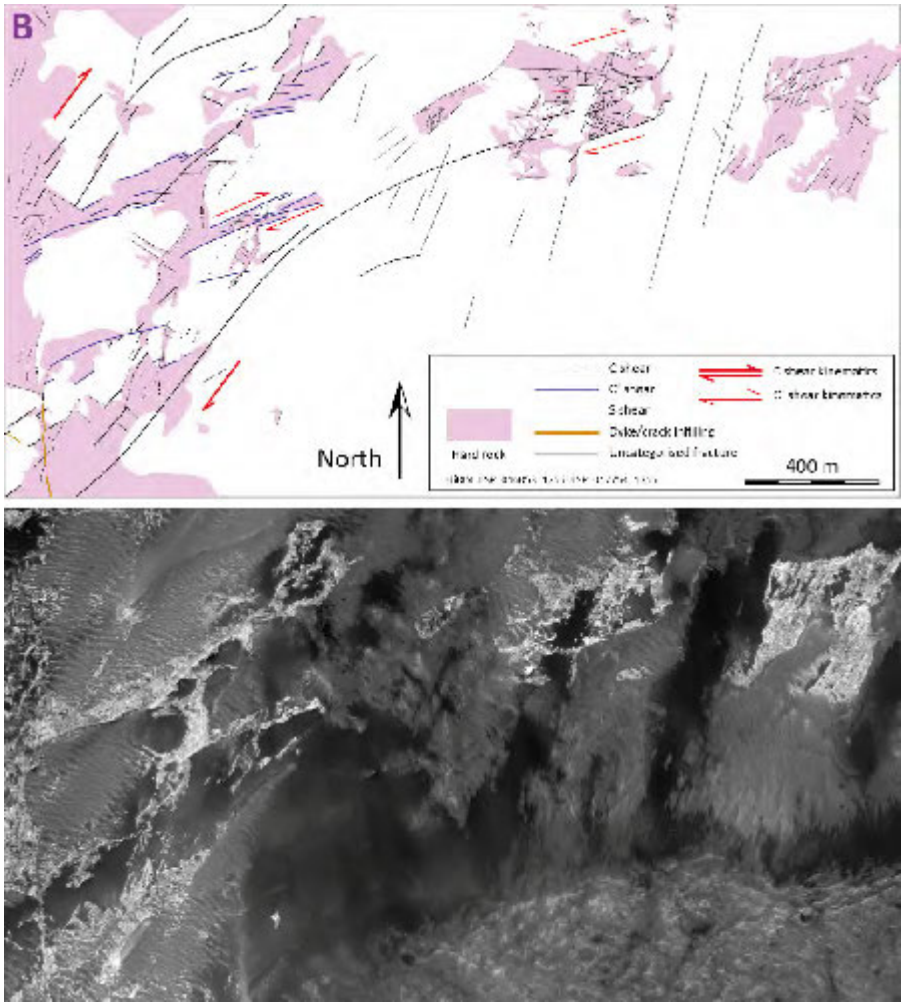
B
North
C-shear
C'-shear
S-shear
Dyke/crack infilling
Hard rock
400 m

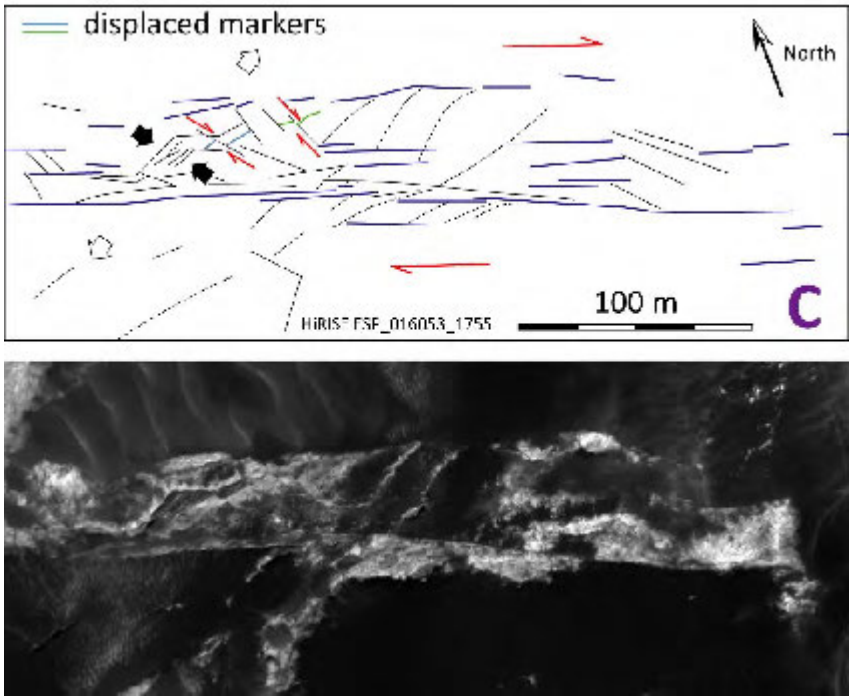
displaced markers
North
100 m
C

Supplementary Figure 2. Tectonic map of the western Hebes Chasma study area with location of the shear zone breccia area shown on Figure 3c, and CTX basemap[1]. The crosses in the tectonic map indicate what is considered as the minimum shear zone width: 3 km (two black and white crosses) to 3.5 km (two grey and white crosses). Younger deposits may hide other structures amenable to reevaluate this estimate. The 3-D view (D) shows CTX image[1] F01_036215_1789_XI_01S077W draped over HiRISE digital terrain model HI_039723_1790_040211_1790-ALIGN-DEM. The HiRISE terrain model was processed with the MarsSI (marssi.univ-lyon1.fr) application funded by the European Union's Seventh Framework Program (FP7/2007-2013), ERC Grant Agreement No. 280168.

Hebes Shear Zone Tectonic Map

2021

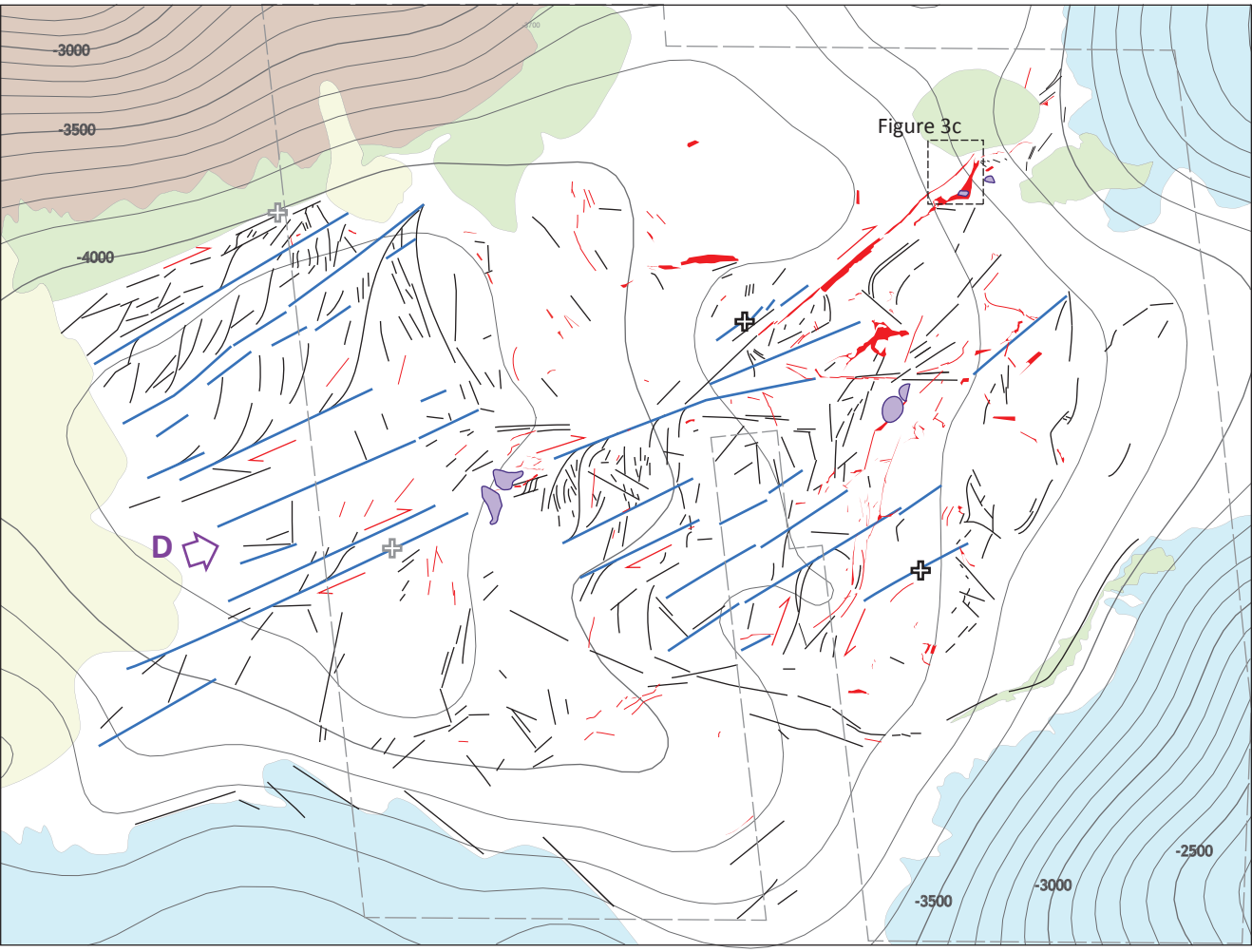

Landslide deposits

Fine-grained mantle

Sand-covered lower ILD

Undifferentiated floor material

Wall rock (basement)

Major shear

Fracture

Plug or intrusion

Intrusive/anatectite/migmatite/mylonite/cataclasite/breccia

Intrusive body or fault infill with mapped margins

Kinematic indicator

Layering plane

2 km

North

Boundary of HiRISE mosaic (ESP_039723_1790; ESP_040211_1790, ESP_042413_1795, ESP_042914_1795, ESP_043692_1795)

Background topography: Mars Express/HRSC digital elevation model of Valles Marineris (dt7.01)

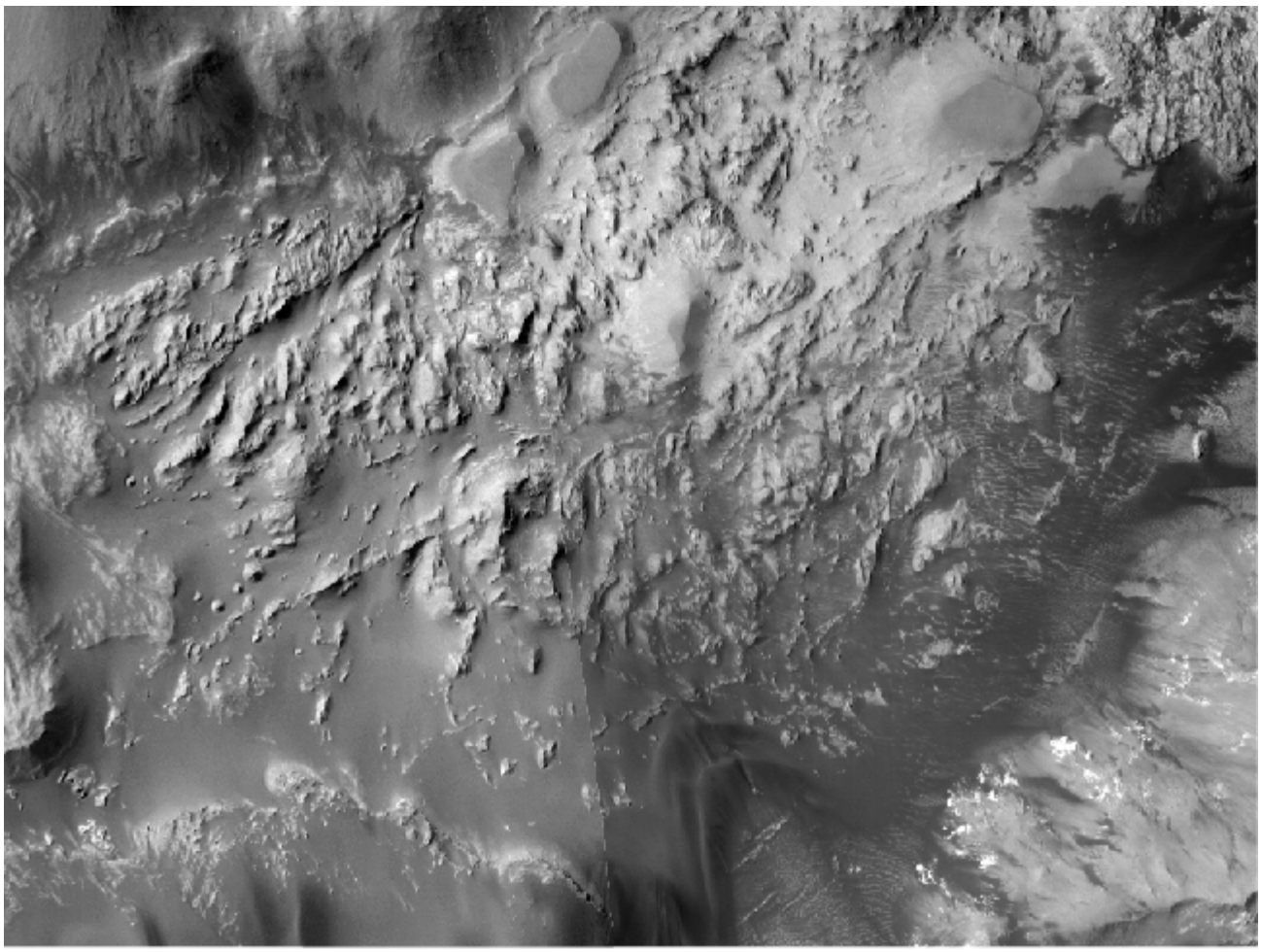
2 km
Hebes Shear Zone Tectonic Map: CTX mosaic
2021
North

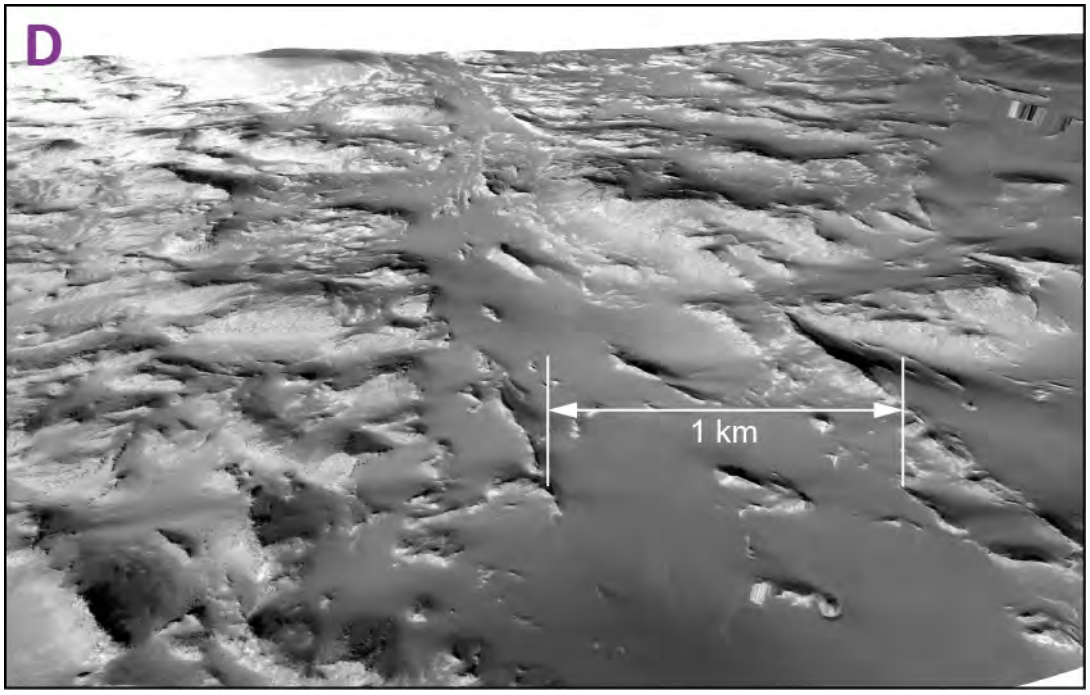
D
1 km

Supplementary Figure 3. A 100 m-high exposure of the exhumed basement south of the Hebes shear zone, and connection with the surrounding units. The basement outcrop is the most spectacular found in Hebes Chasma and Ophir Chasma. (a) HiRISE image ESP_042914_1795 (credit: NASA/JPL/University of Arizona); (b) Geologic map. The contoured digital terrain model combines photogrammetry using the AMES pipeline (HiRISE DTM HI_042413_1795_042914_ 1795) and photoclinometry[2]. Contour spacing: 10 m; (c) Interpreted perspective view. The numbers refer to the stratigraphic succession.

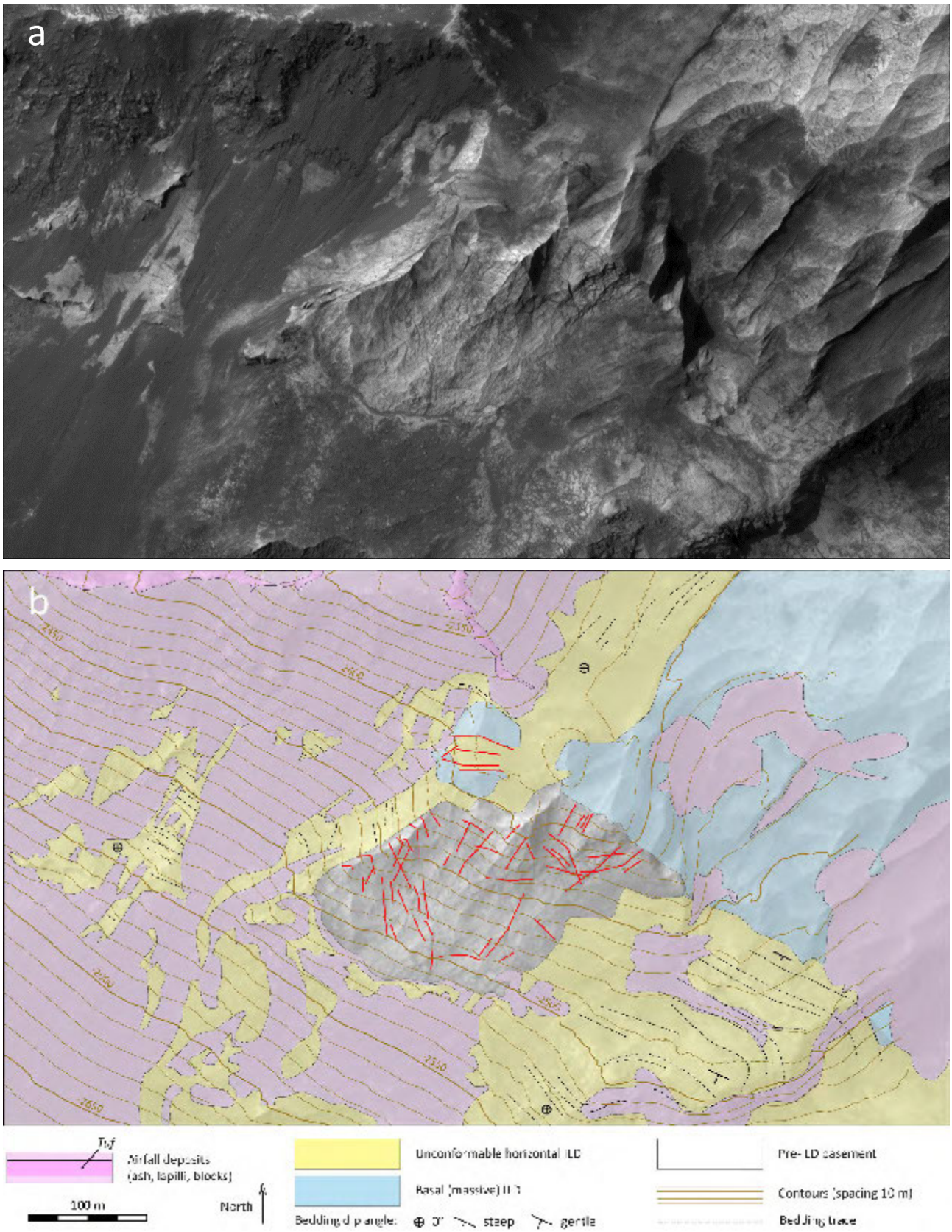

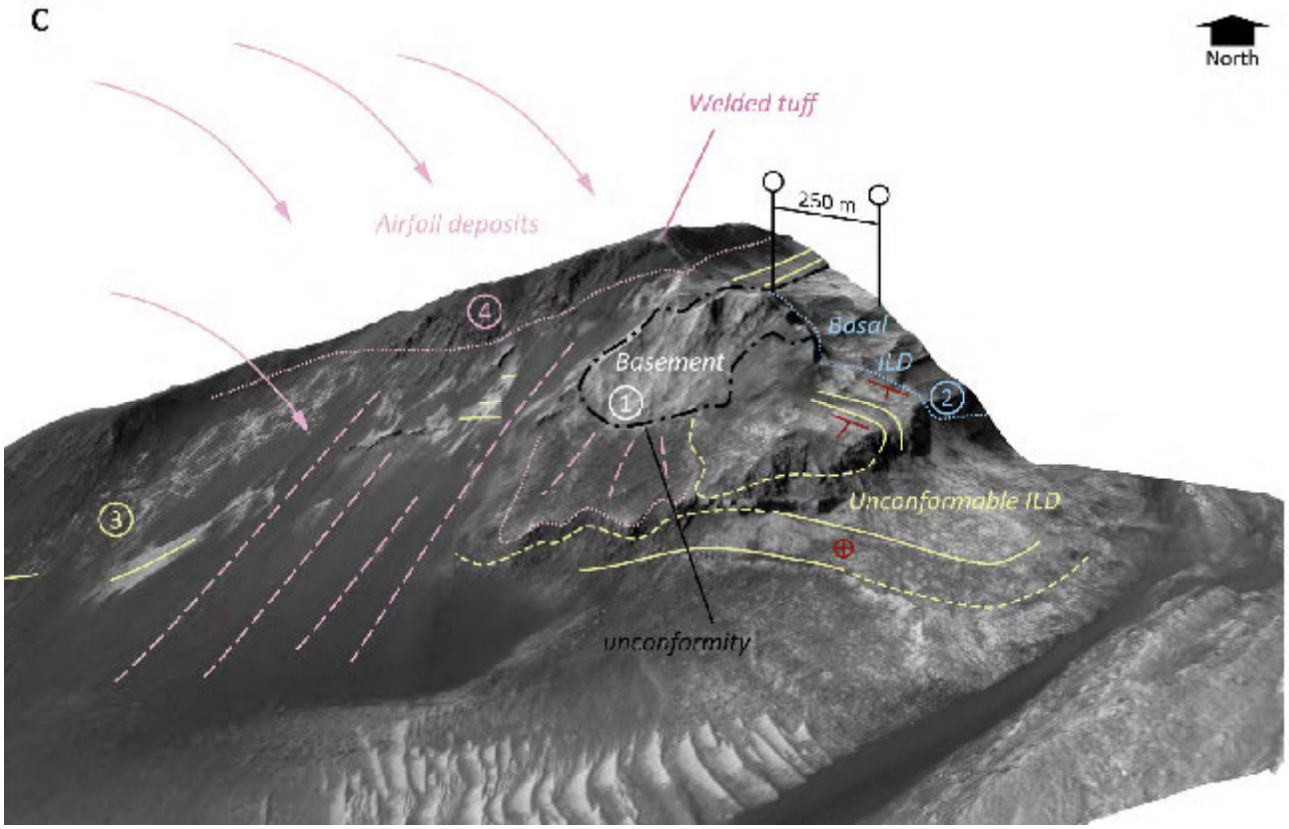
C
North
Welded tuff
Airfoil deposits
250 m
Basal
ILD
Basement
Unconformable ILD
unconformity
1
2
3
4

Supplementary Figure 4. Sample terrains in eastern Ophir Chasma: massive, brecciated, and comparison with the morphology of the nearby Interior Layered Deposits. Megabreccia of Type I have sharp angles, and the matrix contiguous to the blocks is narrow, indicating little relative block displacements. Location on the CTX image mosaic of Supplementary Figure 1. Credit: HiRISE image: NASA/JPL/University of Arizona.

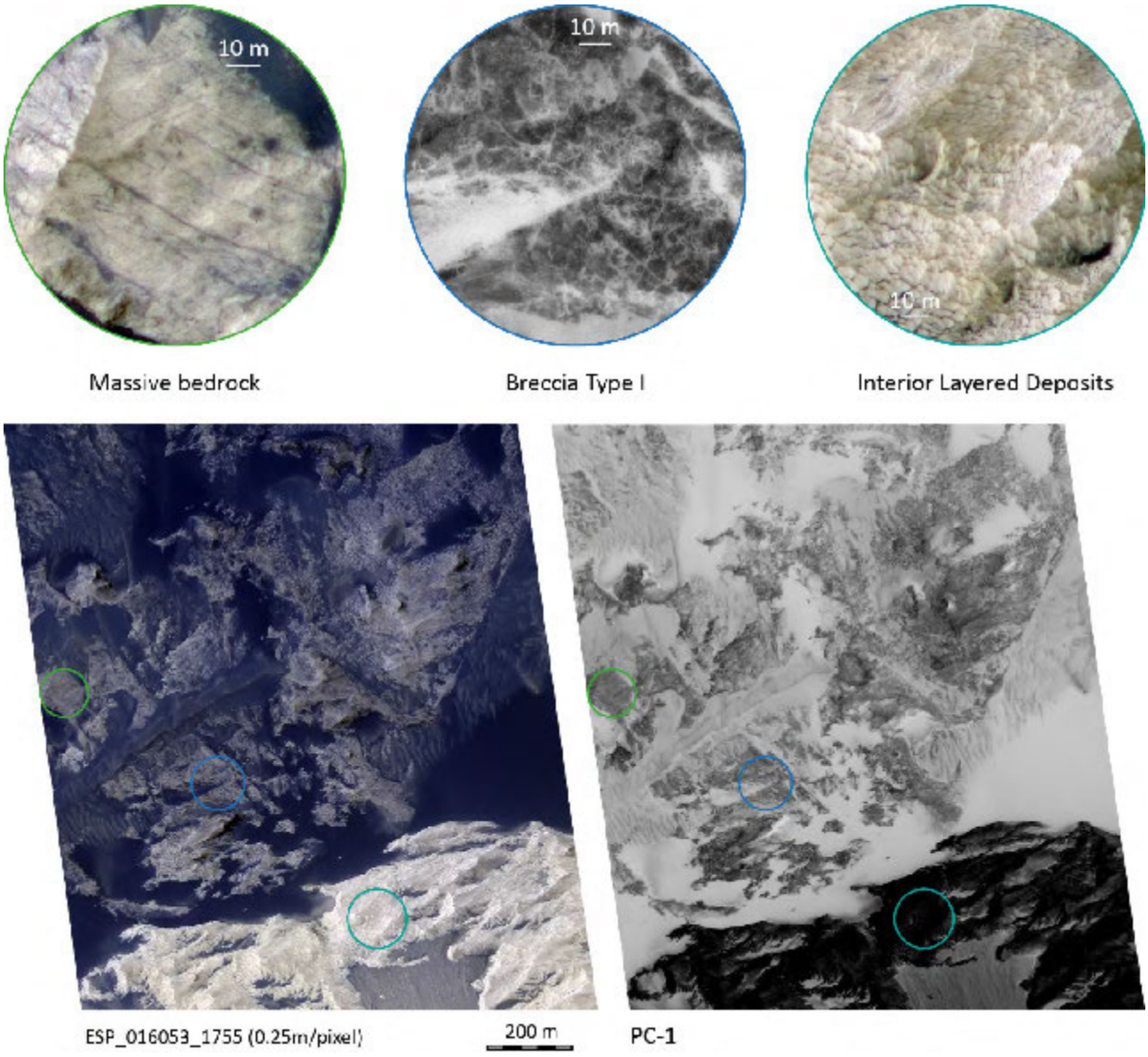

Supplementary Figure 5. Brecciated facies in eastern Ophir Chasma. The matrix of breccia Type II is more abundant than in Type I, and the block are rounded-shaped, indicating higher block mobility. "L" in the upper panel stands for the length of the long axis of the breccia block highlighted by the white circle. Location on the CTX image mosaic of Supplementary Figure 1. Breccia type II are probably made of a material weaker than the matrix, leaving shallow depressions commonly filled by low albedo sedimentary deposits (mottled terrains and dark sands). Credit: HiRISE image: NASA/JPL/University of Arizona.

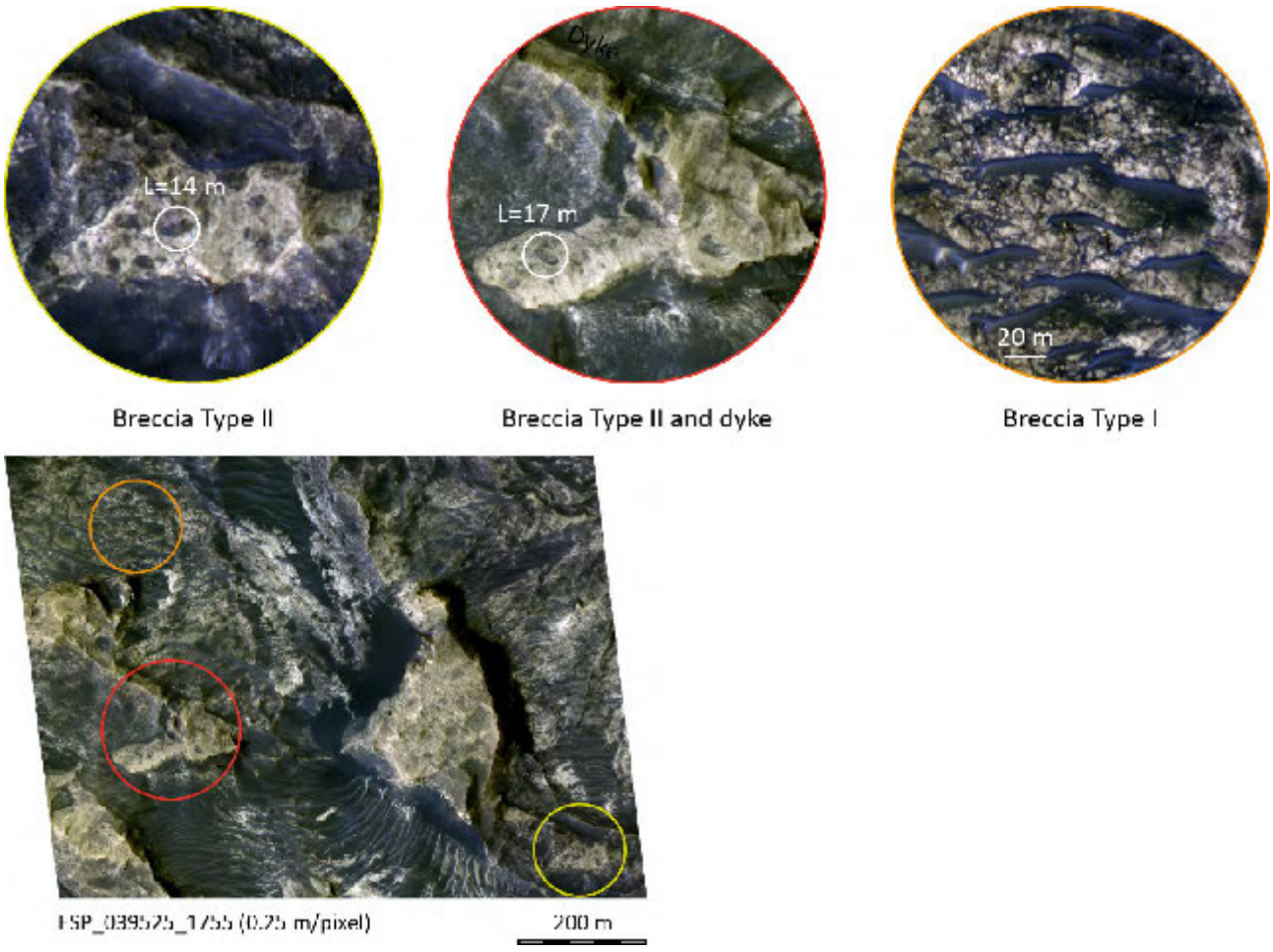

Supplementary Figure 6. Breccia ridge in eastern Ophir Chasma. Location on the CTX image mosaic of Supplementary Figure 1. Credit: HiRISE image: NASA/JPL/University of Arizona.

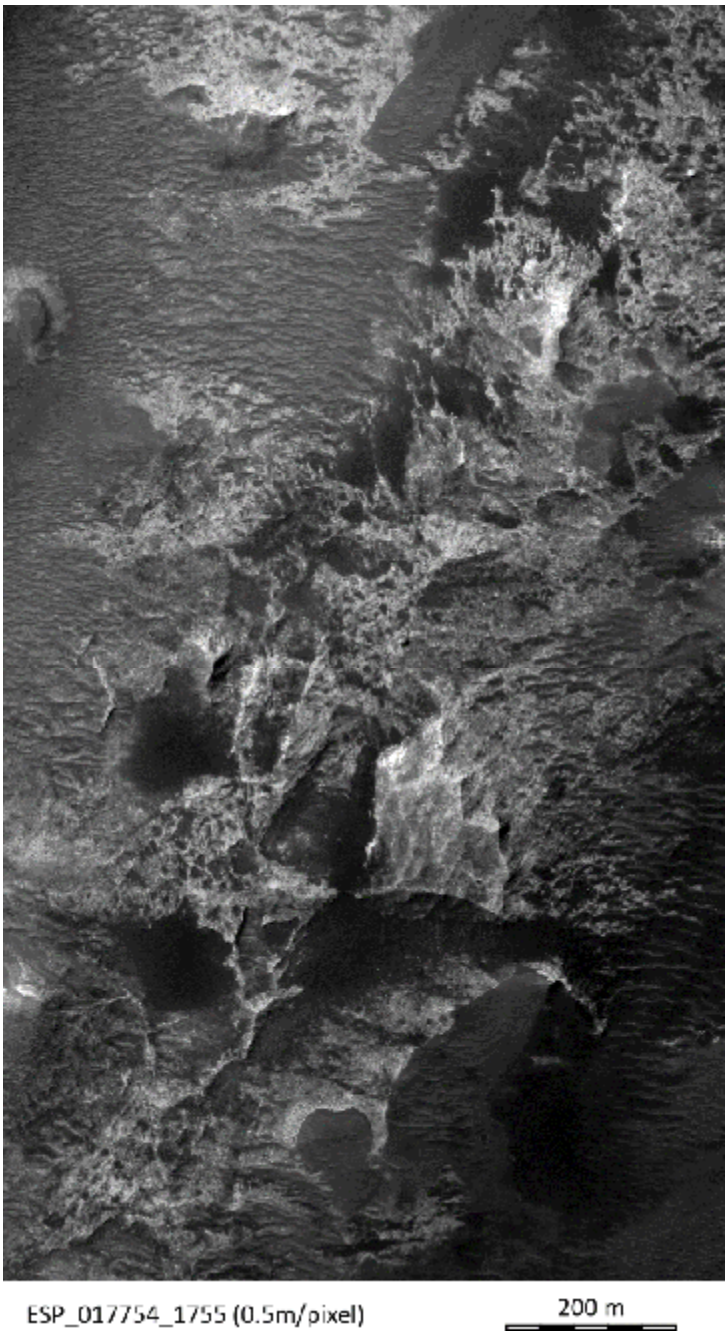

Supplementary Figure 7. Example of an intrusion in the basement rock of eastern Ophir Chasma, and evidence of vertically layered basement. The color image in the lower right is a color-enhanced image of the three first principal components of the HiRISE image shown in the lower left. Location on the CTX image mosaic of Supplementary Figure 1. Credit: HiRISE image: NASA/JPL/University of Arizona.

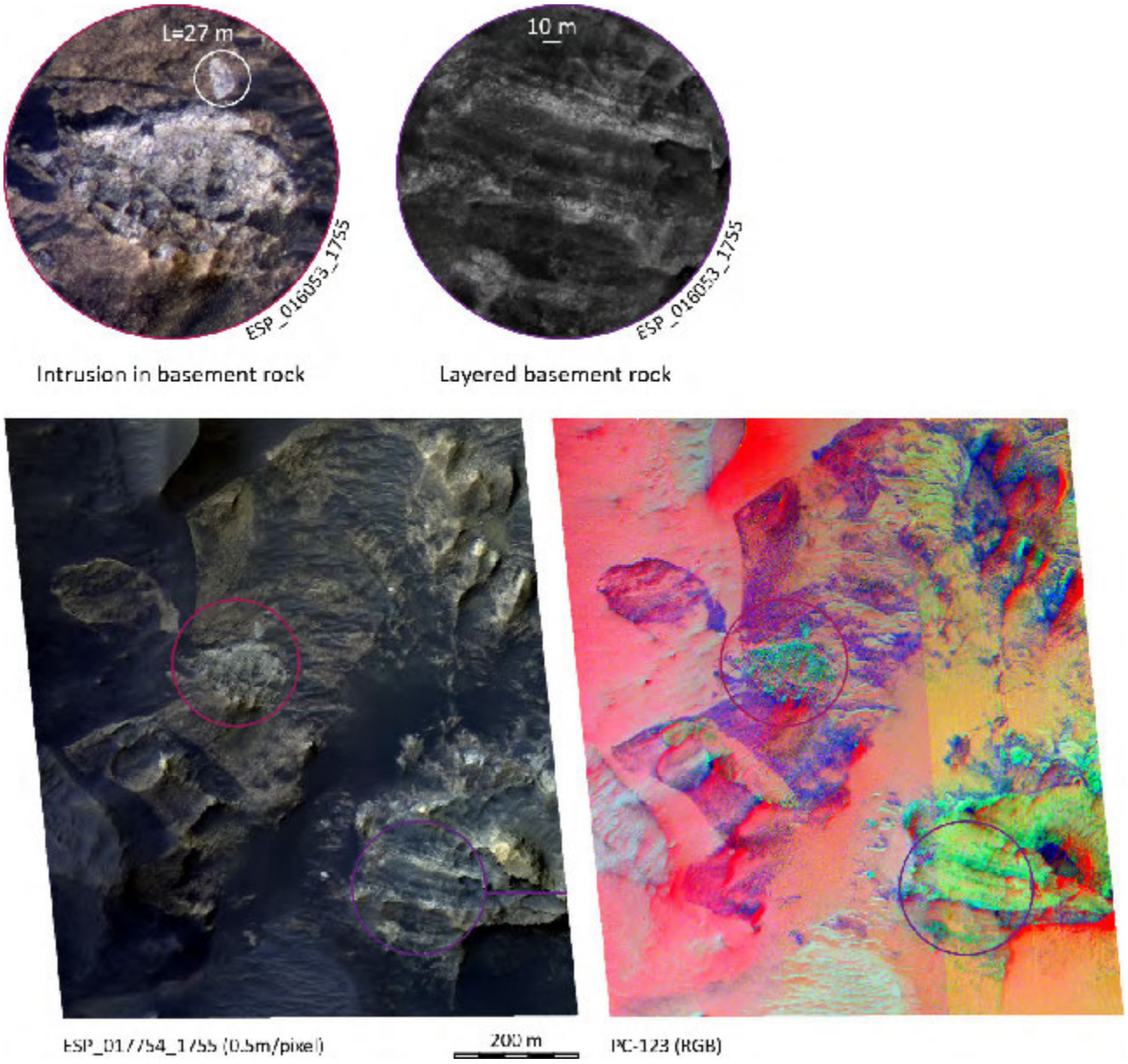

Supplementary Figure 8. Evaluation of shear zone horizontal displacements and lengths.

Ophir and Hebes shear zone maximum displacement inferred from shear zone width (a)[3], and shear zone length inferred from the displacement, assuming a linear relation between shear zone width and maximum displacement (b)[4,5], or a power law relation with the exponent 1.5 (c)[5,6]. The method is described in the Methods section. The number of published datasets available is not sufficient to make predictions; therefore the results shown on these plots are indicative only.

The range of maximum displacement for the two shear zones is between a few tens of kilometers and several hundred kilometers (a). When linear displacement-length scaling is considered (b), the inferred minimum length of the Ophir and Hebes shear zones is a few hundred kilometers and more than 1000 kilometers, respectively, with maximum lengths of several thousands of kilometers. Results are not significantly different when, instead, displacement is related to length following the power law (c).

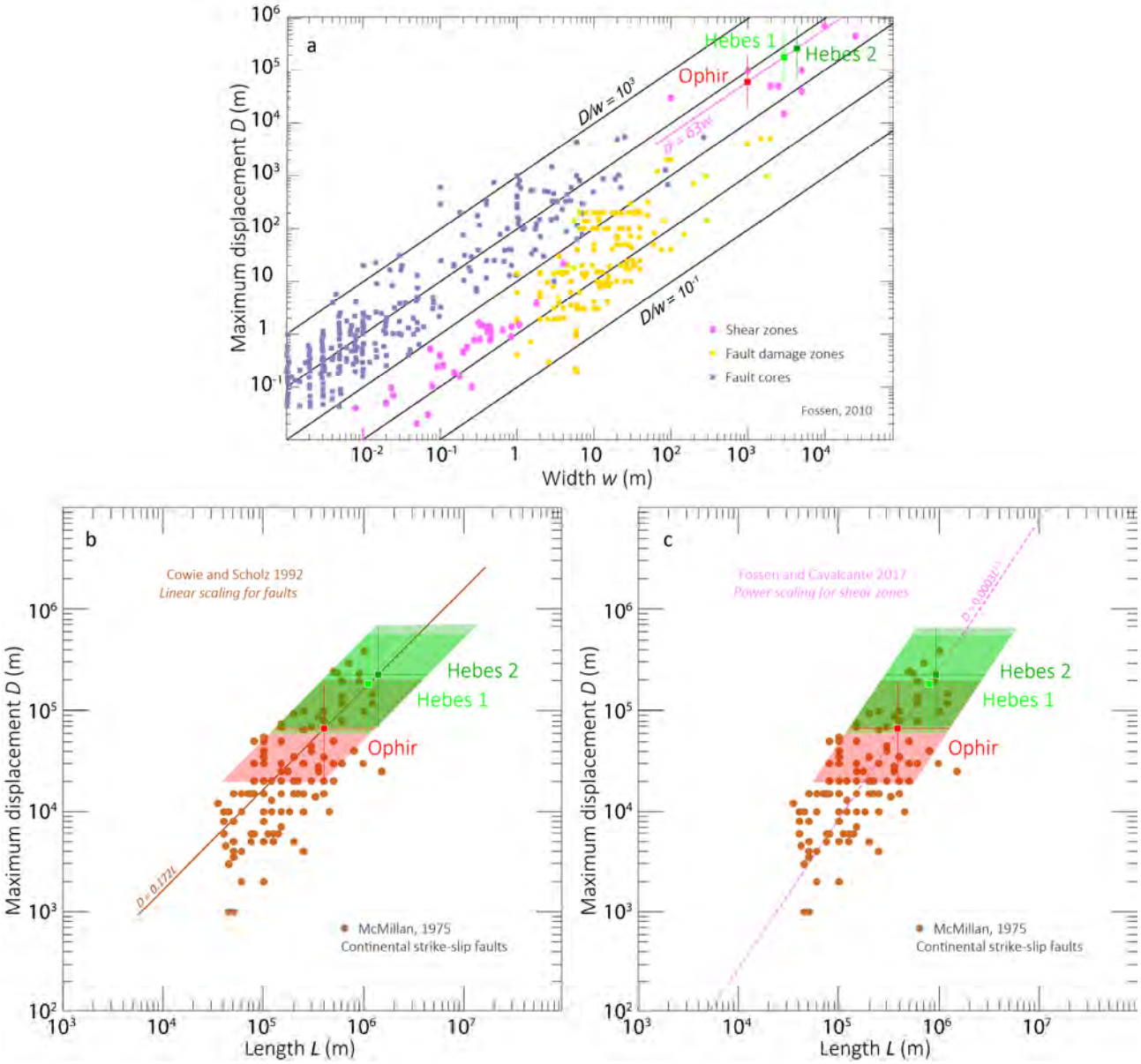

Supplementary Figure 9. Brittle Hesperian and Amazonian tectonic structures coaxial with the Hebes shear zone and the Planetary Dichotomy Boundary (PDB)[7].

Supplementary Figure 9a. Basemap: THEMIS Day IR Global Mosaic[8].

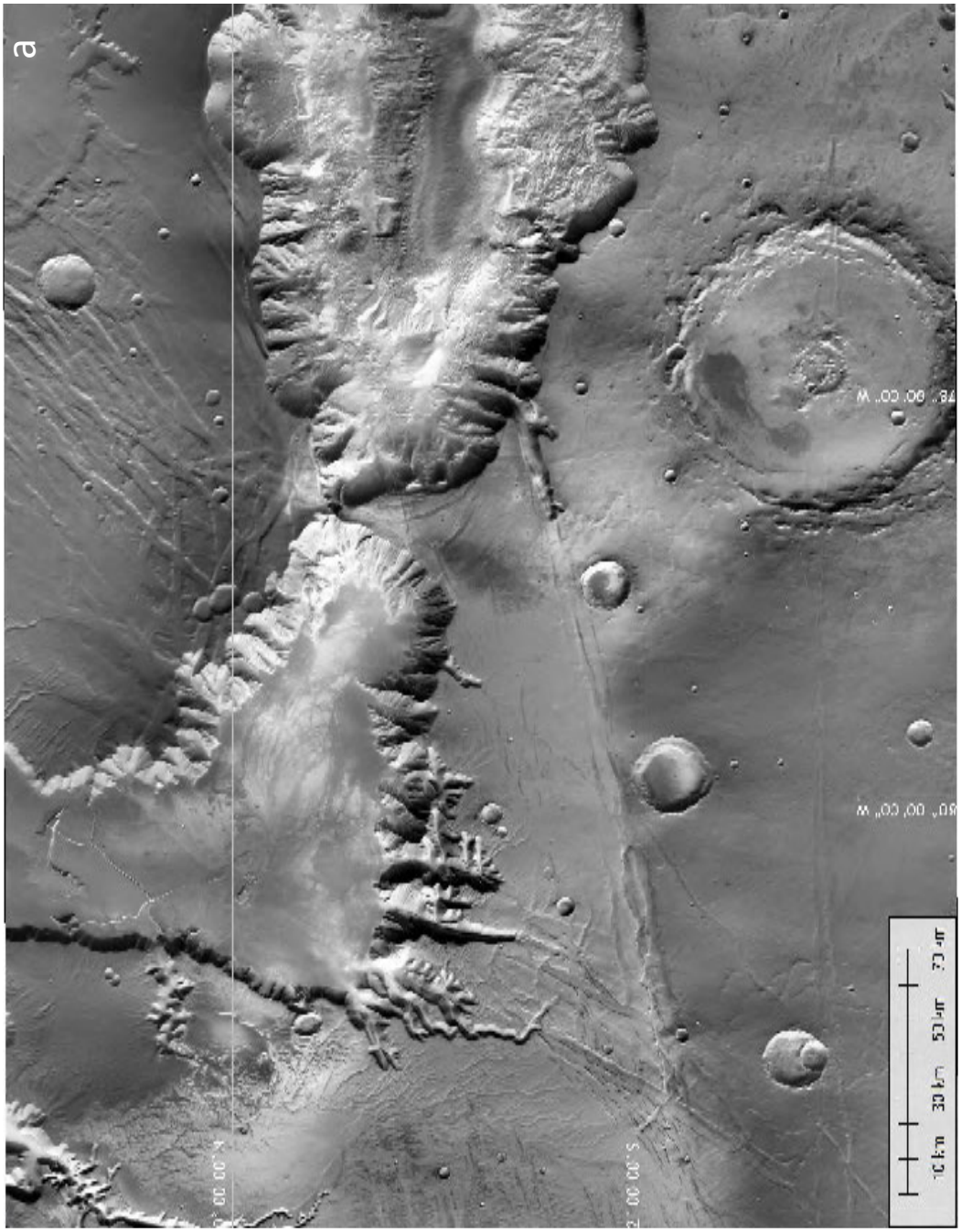

Supplementary Figure 9b. Geologic map. The geological units are slightly modified from earlier maps[9,10]. The basement unit of the Hebes shear zone is in white, and the white dashed line shows the trend of PDB. Blue lines: major shear zone patterns in the Hebes basement unit, and coaxial normal faults cutting Hesperian and Amazonian geological units in Hebes Chasma; red lines: fracture filled with megabreccia: black lines: location of the earliest graben exposed on the plateau. Geologic unit defined in this work: light grey: Basement unit. Geologic units defined by Tanaka et al.[9]: Nhu: Noachian highland undivided unit; eHh: Early Hesperian highland unit; eHv: Early Hesperian volcanic unit; lHt: Late Hesperian transition unit; lHv: Late Hesperian volcanic unit; AHi: Amazonian and Hesperian impact unit; AHv: Amazonian and Hesperian volcanic unit. Geologic units defined by Schmidt et al.[10]: HNw: Wall material; UHtu: Upper ILD Formation; LtHtu: Late ILD; Ab: Slumped wall blocks; Avf: ILD mound flows; Als: Landslide scar; As: Landslide material. The background image is from the THEMIS Day IR Global Mosaic[8]. Contours are after the HRSC digital terrain model of Valles Marineris[11].

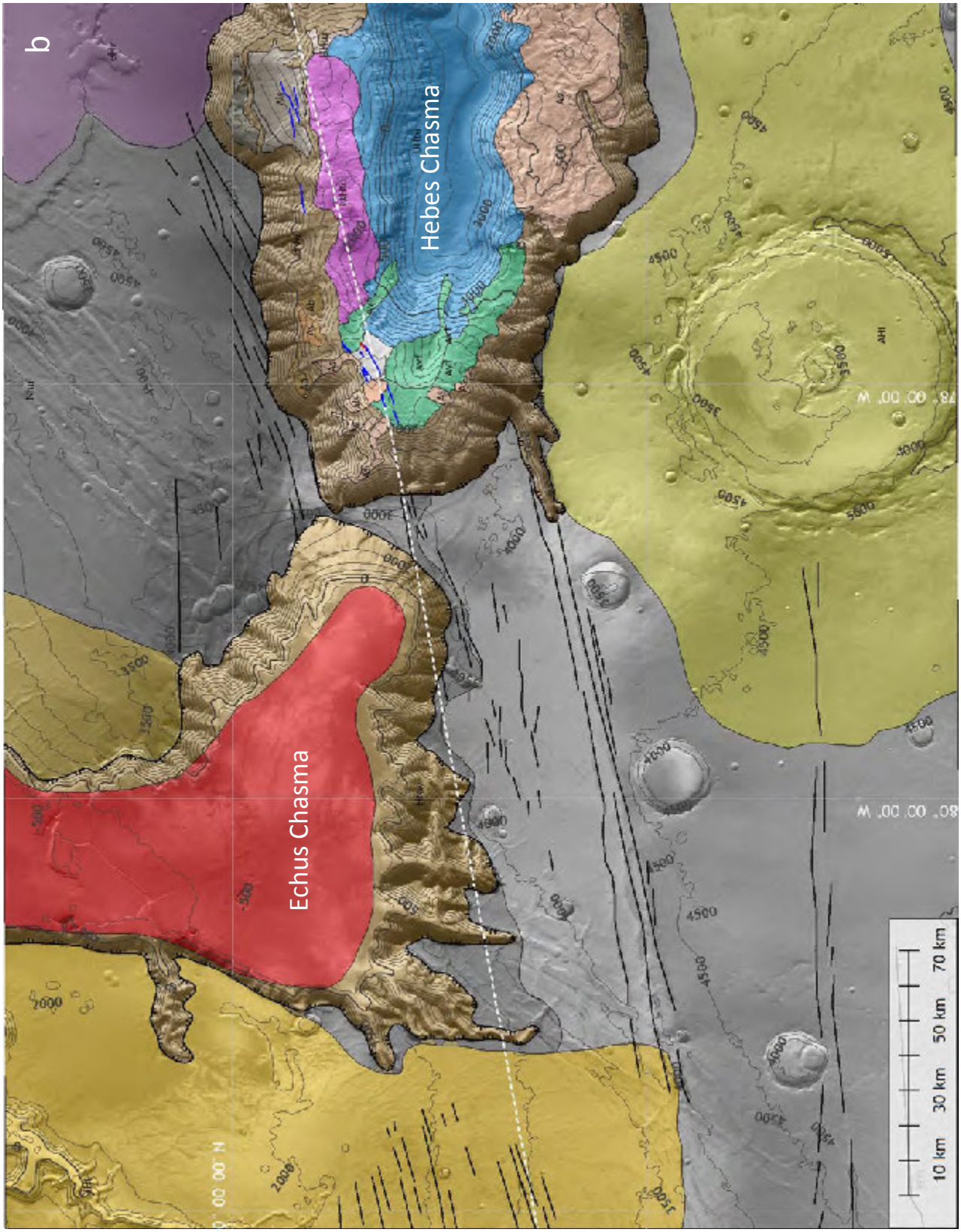
b
Hebes Chasma
Echus Chasma
10 km
30 km
50 km
70 km

Supplementary Figure 10. Magnetic profile across Ophir shear zone (OSZ) and Hebes shear zone (HSZ). The PDB magnetic pattern[12] is a transition between the weak pattern of the Borealis basin and the intense field that characterizes the thicker highlands crust. The profile is located on Figure 4.

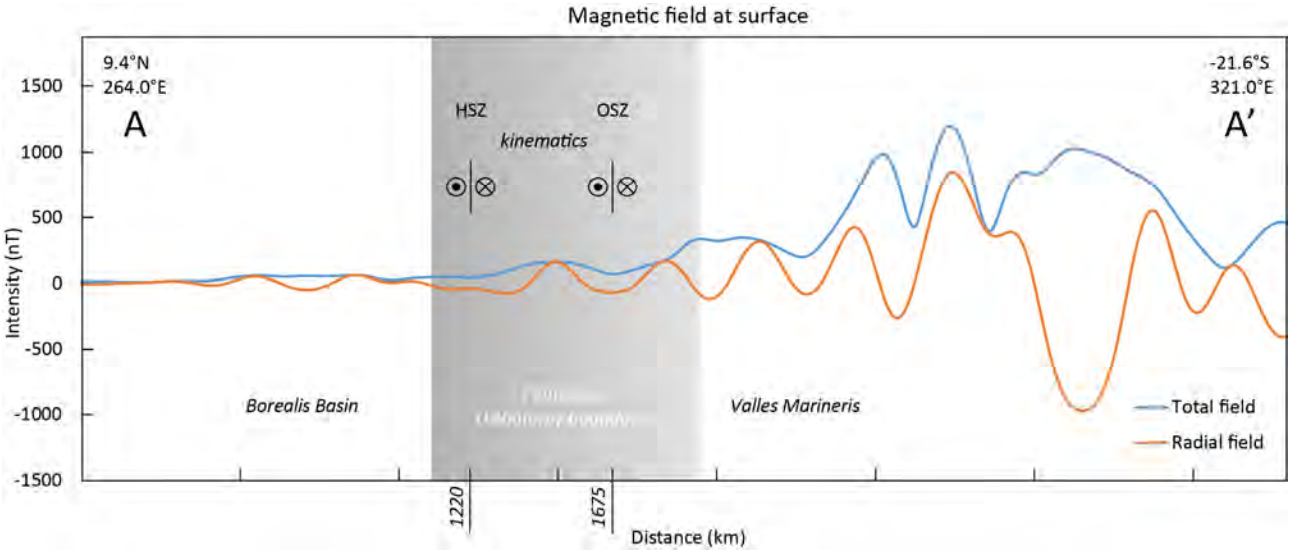

Supplementary Figure 11. Thermal events affecting the measured magnetic field in the Valles Marineris region. The total magnetic field at the surface (B) is from Langlais et al.[12]. The Tharsis thermal events include injection of mafic dykes from Syria Planum[13,14,15,16] (the stress trajectories[13] are updated) and other magmatic intrusions related to the formation of the Tharsis bulge. The origin of the weak magnetization measured in the Borealis basin is discussed by Mittelholz et al.[17]. The trace of the Borealis impact basin, located with ±5° of uncertainty, is after Andrews-Hanna[18]. The age of the Tharsis volcanic flows is after Tanaka et al.[9]. The background image is from the THEMIS Day IR Global Mosaic[8].

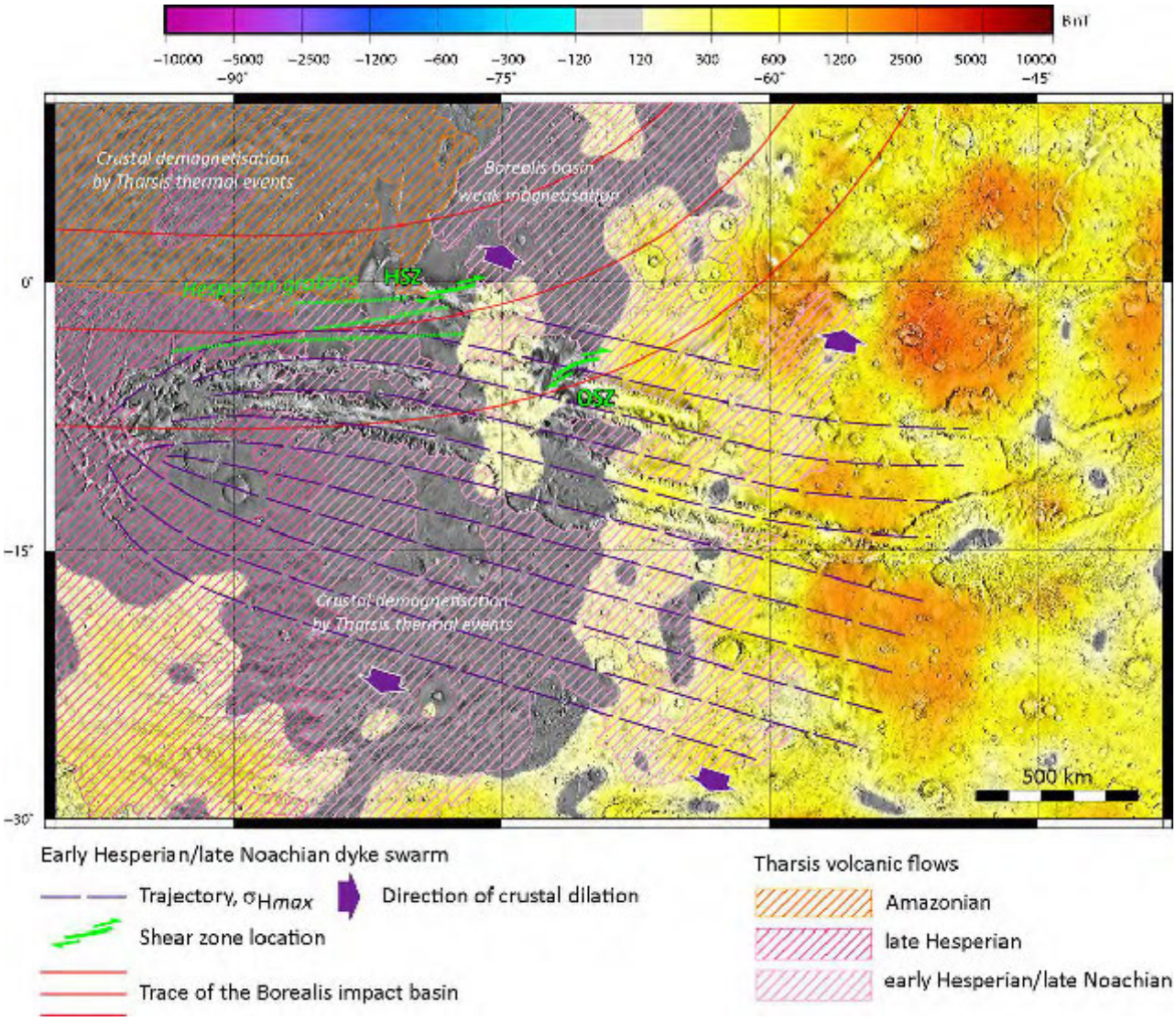

Supplementary Figure 12. Pre-Noachian to early Noachian features related to hydrothermal activity possibly resulting from the Borealis impact and suggested to explain magnetic banding north of Coprates Chasma. Topographic contours (spacing 500 m) are from HRSC (Credit: ESA/DLR/Freie Univ. Berlin).

Magnetic banding parallels a pre-Noachian to early Noachian tectonic fabric. This ancient crust shows evidence of an active hydrologic system. Moreover, HiRISE images of the northern wall of eastern Candor Chasma show that a dike swarm intruded the Valles Marineris plateau parallel to the magnetic banding. The rose diagram was established from 26 representative dykes observed on the eastern Candor Chasma wall; the indicated strike refers to the mean resultant dyke orientation[19]. Magnetic banding in response to hydrothermal activity has been measured at some impact craters and basins on Earth, and based on observations, models[20,21,22], and chemical reactions[23], was attributed to hydrothermal activity. The observations reported here suggest a similar origin.

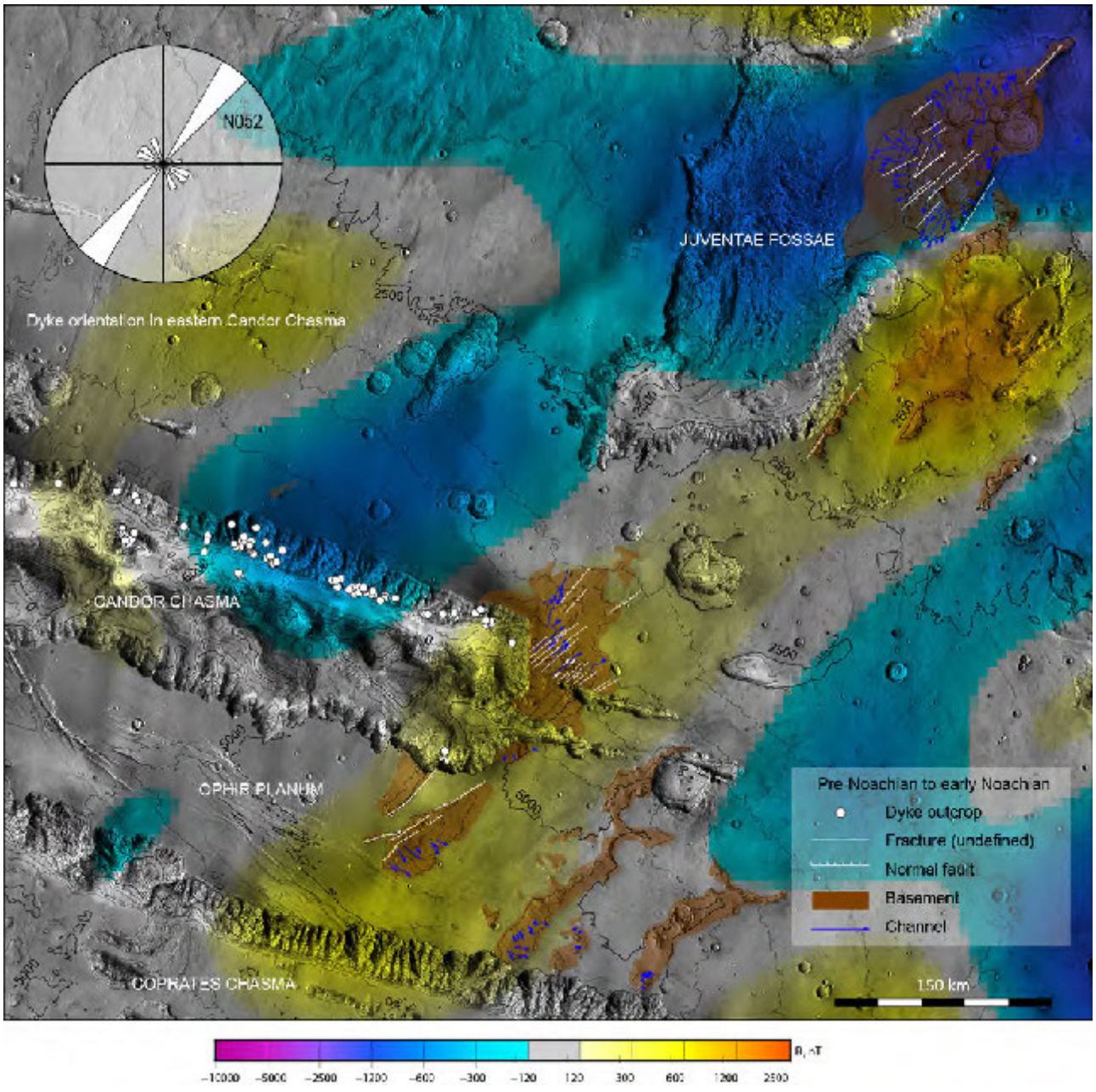

Supplementary Figure 13. Comparison between stress trajectories resulting from thin-shell flexural model of Tharsis loading over the pre-existing planetary dichotomy boundary, from Andrews-Hanna[18], and orientation of the measured radial magnetic field (Br) at the surface, from Langlais et al.[12]. The resolution corresponds to the spherical harmonic degree 134.

Supplementary Figure 13a. The shear zones and magnetic anomalies are shown in the Tharsis loading context, after the pre-Noachian. The trace of the Borealis impact basin, located with ±5° of uncertainty, is after Andrews-Hanna et al.[7]. The thin lines are principal stress trajectories obtained from the thin-shell flexural model of Tharsis loading of the Martian crust affected by the PDB[18]. Black lines indicate the horizontal tensile horizontal principal stress direction and large tensile stress magnitude. White arrows indicate the most compressive horizontal principal stress direction and strongly negative tensile stress magnitude. Combine black and white lines indicate weak tensile stress magnitude. The magnetic anomaly IDs refer to the numbers on Supplementary Figure 13b. The background is from the THEMIS Day IR Global Mosaic[8].

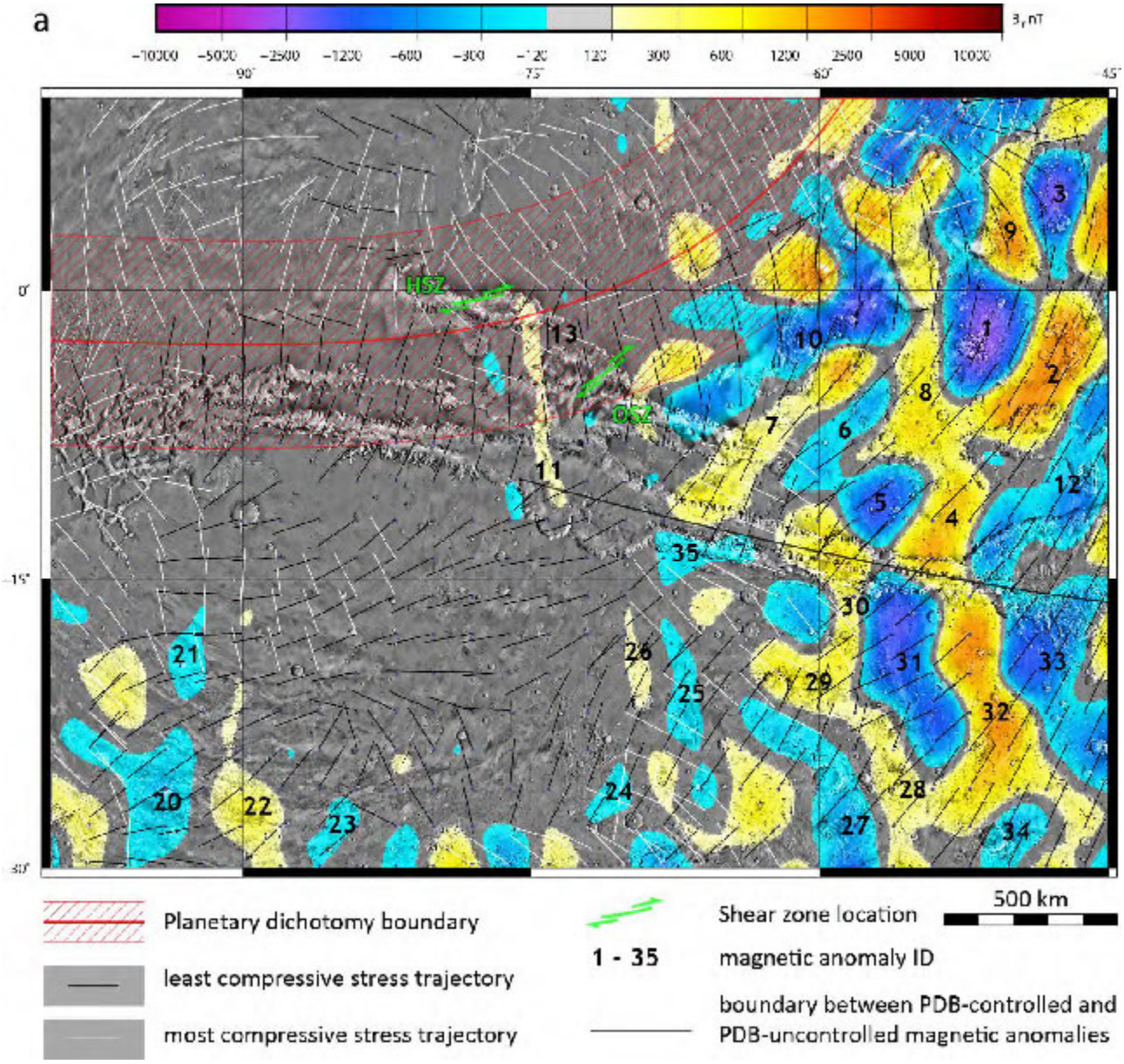

Supplementary Figure 13b. Comparison between the direction of the magnetic anomalies in the radial magnetic field, and the direction of the least compressive stress in the thin-shell flexural model[18]. The directions are usually similar north of Valles Marineris, and usually different south of Valles Marineris.

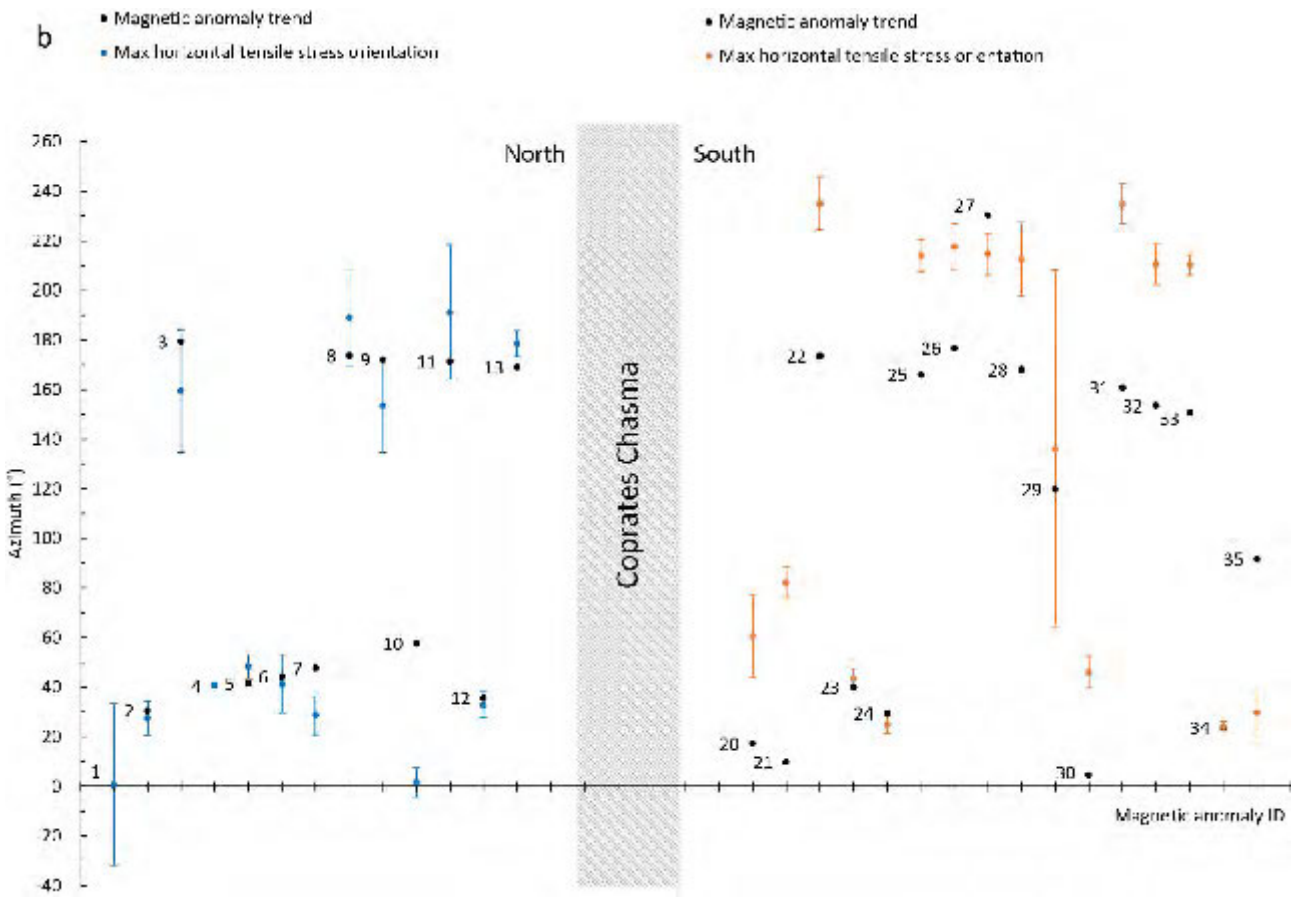

Mapping of the shear zone areas: comparison with earlier works

The mapping presented in this paper required reevaluation of earlier geological maps, which did not show the shear zones identified here, and were proposing an Amazonian age for their hosting rocks.

1. Datasets and interpretations

Shear zone identification requires HiRISE images, which were acquired between 2009 and 2020, mainly after 2015. The first geological map of Valles Marineris data[24] and Ophir and Candor Chasmata[25] were based on Viking images, of much coarser resolution (Supplementary Table 1).

Camera	Shear zone	Images	Acquisition date	Map projected scale (m)	Scaled pixel width (m)
HiRISE	Ophir	ESP_066505_1755	03/10/2020	0.25	
HiRISE	Ophir	ESP_057208_1755	10/10/2018	0.25	
HiRISE	Ophir	ESP_049019_1755 stereo 1	10/01/2017	0.25	
HiRISE	Ophir	ESP_048518_1755 stereo 1	02/12/2016	0.25	
HiRISE	Hebes	ESP_042914_1795 stereo 3	22/09/2015	0.5	
HiRISE	Hebes	ESP_042413_1795 stereo 3	14/08/2015	0.5	
HiRISE	Hebes	ESP_040211_1790 stereo 2	23/02/2015	0.5	
HiRISE	Hebes	ESP_039723_1790 stereo 2	16/01/2015	0.25	
HiRISE	Ophir	ESP_039525_1755	01/01/2015	0.25	
CTX	Hebes	F01_036215_1789_XI_01S077W	18/04/2014		5.32
THEMIS VIS	Hebes	V51823001	20/08/2013		17.8
CTX	Hebes	B21_018018_1790_XN_01S078W	31/05/2010		5.37
HiRISE	Ophir	ESP_017754_1755	10/05/2010	0.5	
CTX	Ophir	B18_016620_1758_XN_04S070W	11/02/2010		5.4
HiRISE	Ophir	ESP_016053_1755	29/12/2009	0.25	
CTX	Ophir	B01_010172_1756_XN_04S071W	27/09/2008		6.24
THEMIS VIS	Hebes	V16841001	30/09/2005		17.8
THEMIS VIS	Ophir	V12086001	04/09/2004		17.4
MOC	Ophir	R1900102	02/07/2004		3.03
MOC	Ophir	R1200203	02/12/2003		4.54
MOC	Ophir	E0100323	05/02/2001		5.74
MOC	Hebes	M0204091 (southern end)	26/06/1999		5.75
Viking	Hebes	919A03	23/12/1978		67.1
Viking	Ophir	913A11	17/12/1978		65.6
Viking	Hebes	738A64	25/06/1978		32

Supplementary Table 1. List of images covering the two shear zones. The list is complete for HiRISE and MOC, only examples of CTX and THEMIS images are indicated due to their abundance, and only Viking images of pixel size < 70 m are indicated.

Supplementary Figure 14 shows the central part of the Ophir shear zone with HiRISE and the earlier images, highlighting the impossibility of tectonic interpretation with the latter. Supplementary Figure 15 shows the same for the Hebes shear zone.

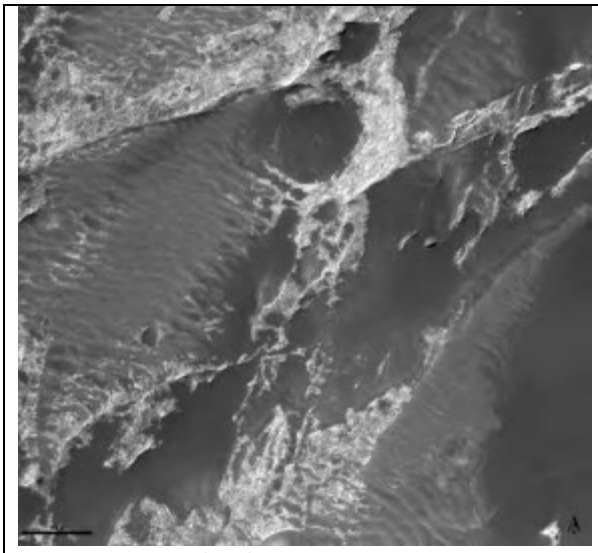

(a) HiRISE (NASA/JPL/University of Arizona)

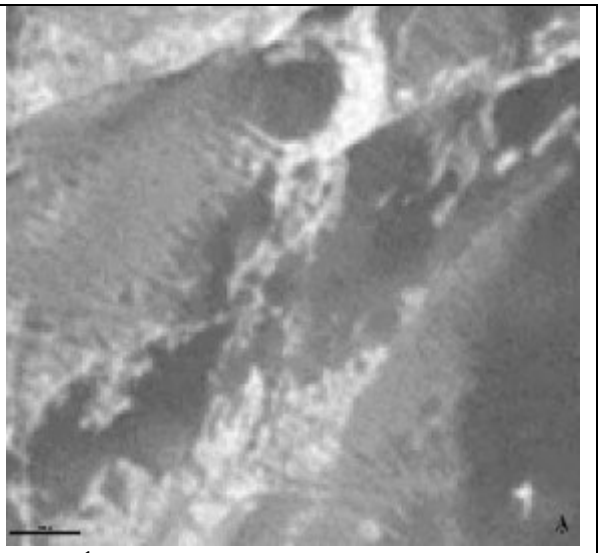

(b) CTX[1]

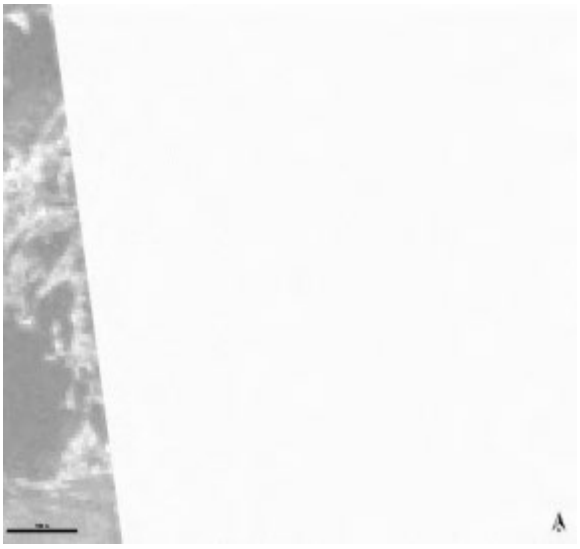

(c) MOC[30]

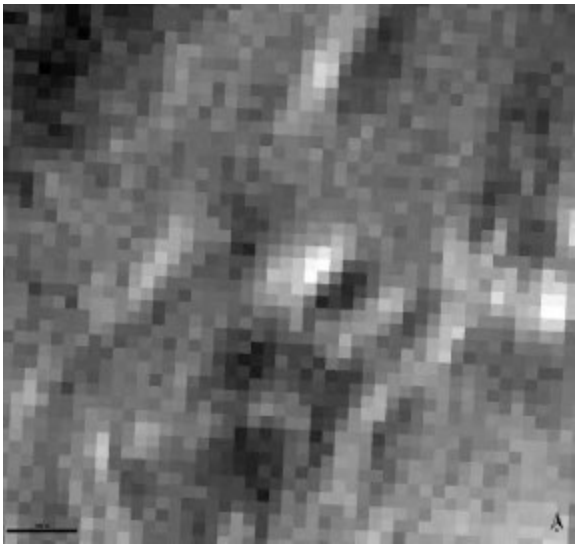

(d) THEMIS[8]

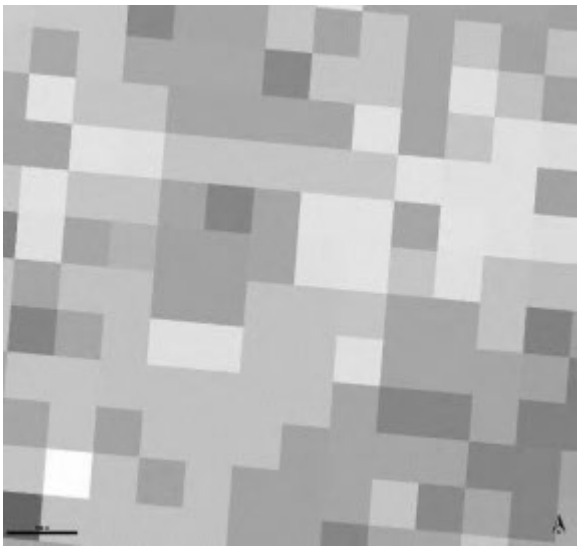

(e) Viking (NASA/JPL/USGS)

Supplementary Figure 14. View of the central part of the Ophir shear zone with HiRISE imagery and earlier datasets. Images are provided at full resolution, with contrast enhancement (0.1%). The scale bar shows 100 m (131072 pixels/degree). After JMARS[29].

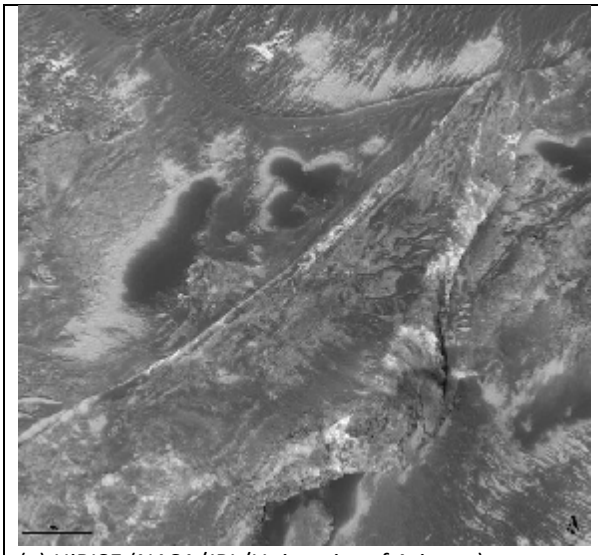

(a) HiRISE (NASA/JPL/University of Arizona)

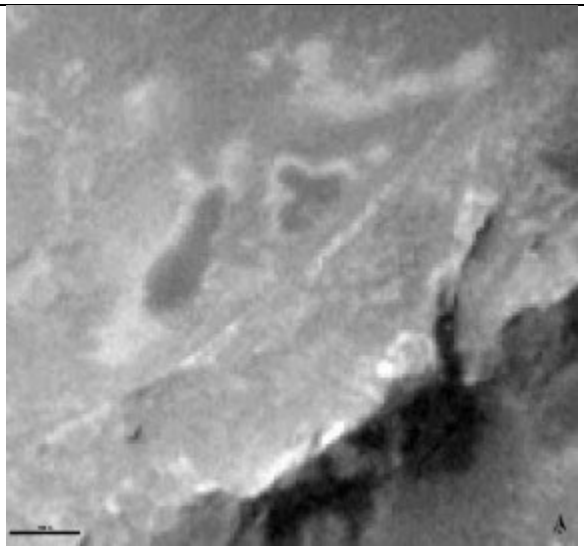

(b) CTX[1]

(c) MOC (no data)

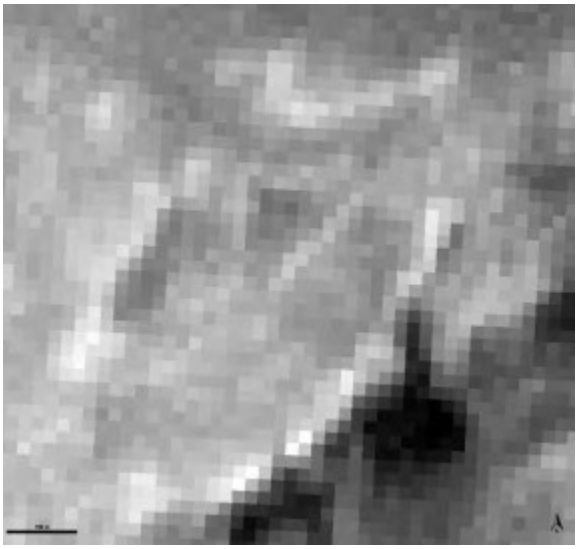

(d) THEMIS[8]

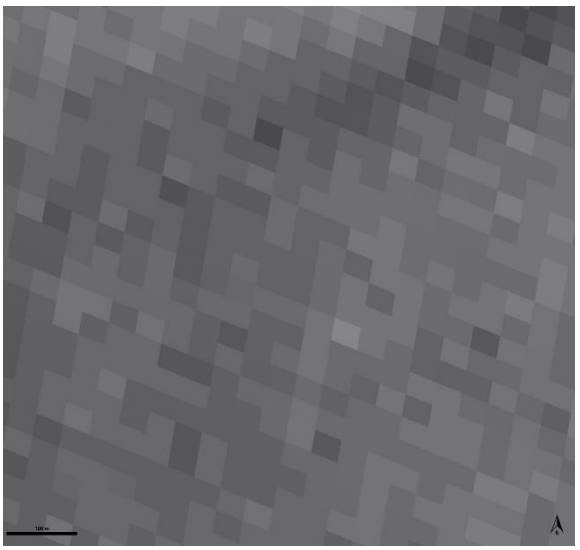

(e) Viking (NASA/JPL/USGS)

Supplementary Figure 15. View of the megabreccia area in the Hebes shear zone with HiRISE imagery and earlier datasets. Images are provided at full resolution, with contrast enhancement (0.1%). The scale bar shows 100 m (131072 pixels/degree). After JMARS[29].

Supplementary Figure 16 shows geological interpretations given to the shear zone area in Ophir Chasma on earlier maps, as well as the Viking image that initially guided these interpretations (Supplementary Figure 16a). Witbeck et al.[24] partly mapped the Ophir shear zone as "channel material of Ophir Chasma" (Acho, Supplementary Figure 16b), a general wording that covers most landforms visible at Viking times and interpreted to be witnesses of large flows of water that conveyed chasma deposits from the northernmost chasmata southward, triggered by the large Ophir Chasma landslides. Supplementary Figure 16 supports the view that in the absence of more precise data, channel material is a viable interpretation of the Viking imagery (Supplementary Figure 16a). Part of the shear zone is also interpreted as "Slide material" (As), owing to the framing of the shear zone by two large landslides. Lucchitta[25] interpreted the Ophir shear zone as Amazonian "smooth material" of diverse origin (Afs), cut by a scarp that marks the boundary of a large landslide in central Ophir Chasma (Supplementary Figure 16c). Part of the shear zone area is therefore a unit that is part of, or mantles, the surface of the landslide. HiRISE images now show that the smoothness of this terrain corresponds to an abundance of mottled dark material between the tectonic structures. Ophir shear zone mapping reveals that the mottled terrain is thin, perhaps not more than one or a few meters at most, because buried patterns are frequently visible across them, forming subdued light-toned features.

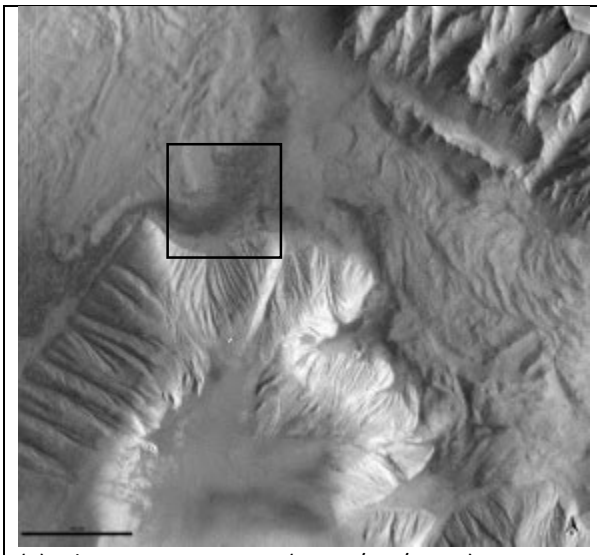

(a) Viking image 913A11 (NASA/JPL/USGS)

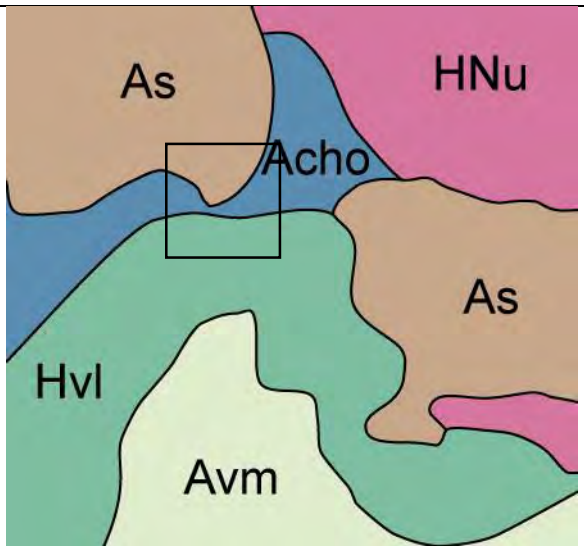

(b) Witbeck et al.[24], redrawn

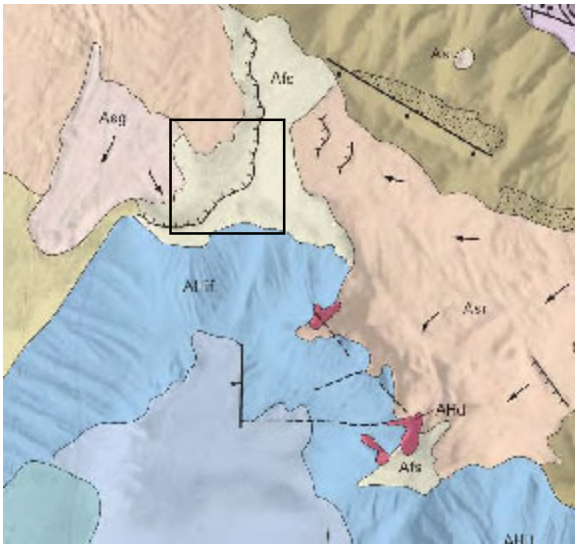

(c) Lucchitta[25]

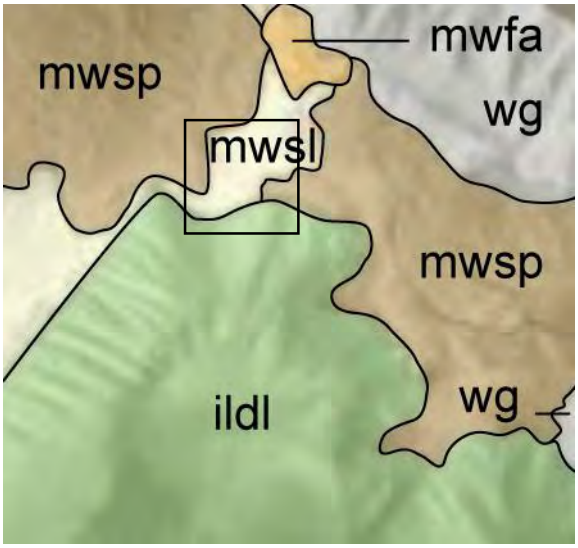

(d) Fortezzo et al.[26], redrawn

Supplementary Figure 16. Viking highest resolution image and interpretation of the Ophir shear zone in earlier maps. The shear zone is in the box. The scale bar in (a) shows 10 km. The symbols of the shear zone area are explained in the text, the others can be found in the cited references.

Fortezzo et al.[26] keep the landslide-related material interpretation of Lucchitta[25] (mwsl, "Debris, rotational, rock planer, and translational slide types"), but simplifies it owing to the smaller mapping scale (Supplementary Figure 16d).

In Hebes Chasma, Witbeck et al.[24] mapped the shear zone area partly as "Slide material" (As) and "rough floor material" (Avfr), which correctly depicts the contorted morphology and knobs observed on Viking imagery (Supplementary Figure 17). Using the more recent datasets, Fortezzo et al.[26] and Schmidt et al.[10] included the Hebes shear zone into a broader unit. Fortezzo et al.[26] fully included it into a unit of "Debris, earth, and rock fall types" (mwfa). Schmidt et al.[10] interpreted the area as "moraines and low energy lobate flows of ILD material possibly driven by freezes-thaw creep". The lobate features, already noted by Witbeck et al.[24], probably correspond to the sigmoidal schistosity interpreted in our mapping. The interpretation of moraines is consistent with the requirement that the shear zone areas underwent significant abrasion, leading to exhumation of an ancient floor, and the more general finding that glacial erosion played a critical role in shaping the Valles Marineris chasmata[27,28].

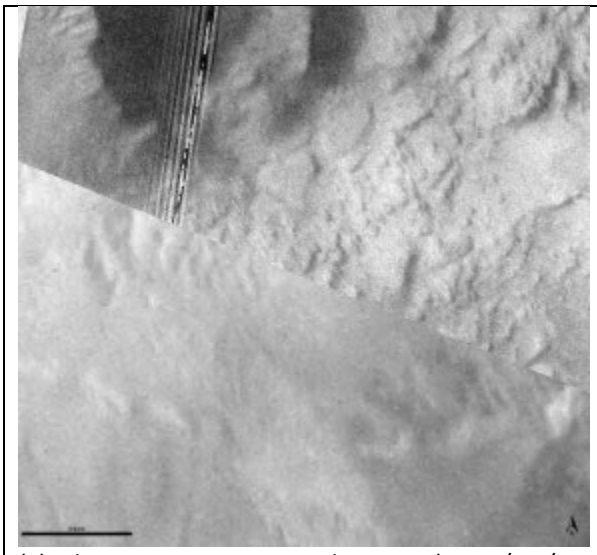

(a) Viking images 738A64 and 919A03 (NASA/JPL/USGS)

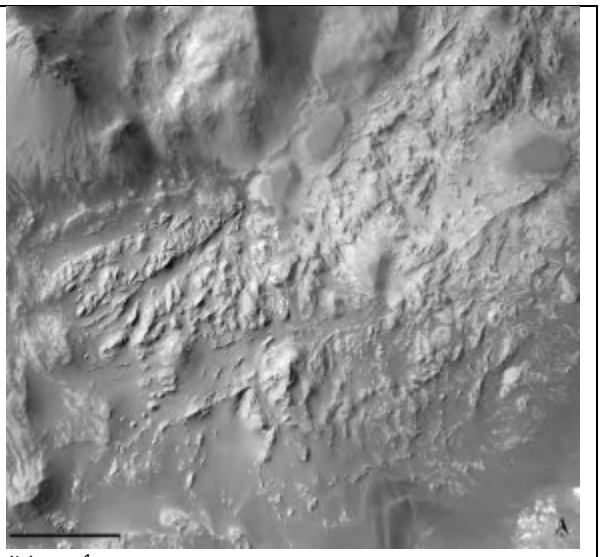

(b) CTX[1] image mosaic

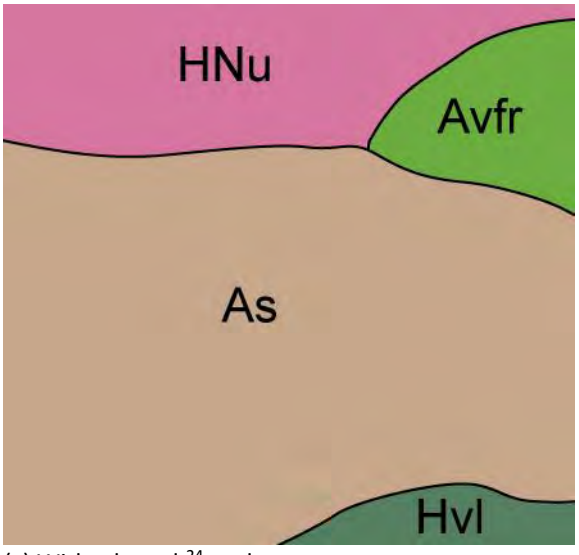

(c) Witbeck et al.[24], redrawn

Supplementary Figure 17. Viking highest resolution image mosaic, CTX image mosaic, and interpretation of the Hebes shear zone by Witbeck et al.[24]. The scale bar in (a) and (b) shows 2.5 km. The map by Fortezzo et al.[26] and Schmidt et al.[10] are not shown because the whole shear zone area is covered by a single unit. The symbols of the shear zone area are explained in the text, the others can be found in the cited references.

2. Age of sheared terrain

Earlier mapping[10,24,25] ascribed the shear zone areas an Amazonian age. We argue in the paper that such recent deposits are probably present, but discontinuously overly much older, probably pre-Noachian basement. Dating of the shear zone areas through crater retention age determination is made difficult by their small size (50 km^2 in Ophir Chasma and 100 km^2 in Hebes Chasma, which also include mottled terrains and dune fields of arguably Amazonian age). Our work indicates that the shear zone surface has been exhumed, for instance by glacial erosion, removing most evidence of impact craters. HiRISE mapping reveals, however, the presence of possible impact craters in the Ophir shear zone, subdued by the dark mottled terrain between the shear zone basement rocks. Due to uncertainty in their interpretation, and in order to not increase map complexity, these features are not shown on the maps presented in the Supplementary Figures.

Detailed description of the mineralogical identification scheme

1. Criteria used for selection of spectral library minerals

1.1. Inferences from literature

Similar rocks to the bright rocks of the Valles Marineris shear zone host rock (HRSZ) have been identified in Valles Marineris and elsewhere on Mars, and primary rock mineral compositions have been identified (Supplementary Table 2).

Geological environment	Instruments used	Mineralogical identification	Rock interpretation
Valles Marineris			
Chasma walls[51]	MOC		Intrusive rock (cumulate?)
Chasma walls[52]	CRISM, HiRISE	LCP	Igneous rock
Chasma walls[53]	CRISM, HiRISE	Ol, LCP, HCP, Pl	
Ophir central valley[54]	OMEGA, CRISM	S	"Sulfate-bearing ridge"
Other regions			
Volcanic plains[42]	THEMIS	Fsp, Px, Ol, High-Si; S, C, Qz	Volcanic
Crater central peak[55]	CRISM, HiRISE	Ol, LCP, Pl	Bedrock, incl. massive fractured and impact megabreccia± clast-rich
Bedrock plains[43]	THEMIS, HiRISE	Ol and/or Px	Friable: Pyroclastic, impact-generated, or detrital

Ol: Olivine; Px: Pyroxene; LCP: Low-Ca pyroxene; HCP: High-Ca pyroxene; Fsp: feldspar; Pl: Plagioclase; S: Sulfates; C: Carbonates; Qz: Quartz

Supplementary Table 2. Composition of some potential HRSZ analogues

1.2.Suggestions from structure and geomorphology

The HRSZ is massive, and shows fracture patterns reminiscent of plutonic bodies (Supplementary Figures 3a and 4). Moreover, brittle-ductile shear zone does not develop in some rocks, such as basalt, peridotite, and clays. Color, fracturing together, and rheological constraints are consistent with plutonic rock, especially of felsic to intermediate composition; metamorphic rock (gneiss, mylonite, migmatite, marble, quartzite), and anhydrite. Sulfates, which may be either of in situ hydrothermal alteration of this rock, or transported by wind from neighboring Interior Layered Deposits (ILD)[31], may also contribute to the bright color.

1.3. Results from spectral indices

The CRISM cube FRT00018b55 covers most of the Ophir shear zone. Spectral indices have been published to assist in detection of minerals and volatiles[32,33,34,35]. They help evaluate cube noise at a glance, its potential in detecting minerals, and give ideas that help to constrain the initial steps of spectral unmixing by identification of minerals to be placed in the input spectral library.

Supplementary Table 3 provides a summary of an analysis using the selected spectral indices. The table shows that the major minerals to look for are olivine, hydrated sulfates, and hydrated minerals in general.

Carbonates also need to be checked. Supplementary Figure 18 shows results obtained for the studied cube using selected spectral indices.

Spectral index	Used for	Caveats	Detection in HRSZ
Magmatic rock minerals			
OLINDEX3	Ol, Px	HCP, Fe-phyllosilicates	++
VAR	Ol, Px	Ices	++
HCPINDEX2	Px, favors high-Ca	Low-Ca Px	--
LCPINDEX2	Px, favors low-Ca	*not identified*	--
BD1300	Pl with Fe^{2+} substitution	Fe-Ol	--
BDI2000	Px	Ices	--
Sulfates			
BD2100_2	1·H_2O sulfates	Alu, Srp	++
SINDEX2	1·H_2O and *x*·H_2O sulfates	Ices	++
BD1750_2	Gp, Alu	-	=
BD2230	(-OH) Fe(III) sulfates	Other Al-OH minerals	=
BD2265	Jrs (also Gbs, acid-leached Ntr)	*not identified*	-
Carbonates			
BD2500_2	Mg-Cb	Zeo	+
CINDEX2	Cb	*not identified*	+
BD3400_2	Cb	*not identified*	=
MIN2295_2480	Mg-Cb	Silicate (-OH) + Zeo mixtures	--
MIN2345_2537	Ca,Fe-Cb	Prh, Srp, Si (-OH) + Zeo mixtures	--
Hydrothermal/Low grade metamorphic minerals			
BD2355	Chl, Prh, Pmp	Cb, Srp	-
Hydrated or hydroxylated minerals			
BD1900_2	*x*·H_2O except 1·H_2O sulfates	*not identified*	++
BD1435	CO_2 ice, some (·H_2O)	*not identified*	+
BD2165	Prl, Kln	Bei, All, Img	+
BD3000	·H_2O	*not identified*	+
BD1400	·H_2O or -OH	*not identified*	=
BD2210_2	Al-OH	Gp, Alu	=
BD2190	Bei, All, Img	Kln	-
MIN2200	Kln	*not identified*	-
BD2290	Mg,Fe-OH minerals	Mg-C	-
D2200	Al-OH	Chl, Prh	--
MIN2250	Opl	*not identified*	--
D2300	(-OH) Fe,Mg silicates	Mg-C	--
Various			
R1330	IR albedo	*not identified*	++
ISLOPE1	Fe^{3+} coating on dark rock	Shaded slopes illuminated by atmospheric scatter	++
BDI1000IR	Crystalline Fe^{2+} silicates	*not identified*	+
BD1500_2	H_2O ice	*not identified*	+
BD2600	H_2O vapor	*not identified*	=
BD3100	H_2O ice	*not identified*	=
BD3200	CO_2 ice	*not identified*	=
ICER1_2	CO_2 (+) H_2O (-) ice mixtures	*not identified*	=
ICER2_2	CO_2 (+) vs H_2O ice/soil (-)	*not identified*	-

Supplementary Table 3. Summary of mineral detections inferred from selected spectral indices defined in Viviano-Beck et al.[35]. All: Allophane; Alu: Alunite; Bei: Beidellite; Cb: Carbonate group; Chl: Chlorite; Gbs: Gibbsite; Gp: Gypsum; Img: Imogolite; Jrs: Jarosite; Kln: Kaolinite group; Ntr: Nontronite; Ol: olivine; Opl: Opal; Pl: plagioclase group; Prh: Prehnite; Pmp: Pumpellyite; Px: pyroxene group; Prl: Pyrophillite; Srp: Serpentine; Zeo: zeolite group. Columns 1-3 are after Viviano-Beck et al.[35]. Detection in HRSZ compared to cube average: '++': strongly more positive; '+': a little more positive; '=': no detection, equal to background; '-': a little more negative; '--': strongly more negative.

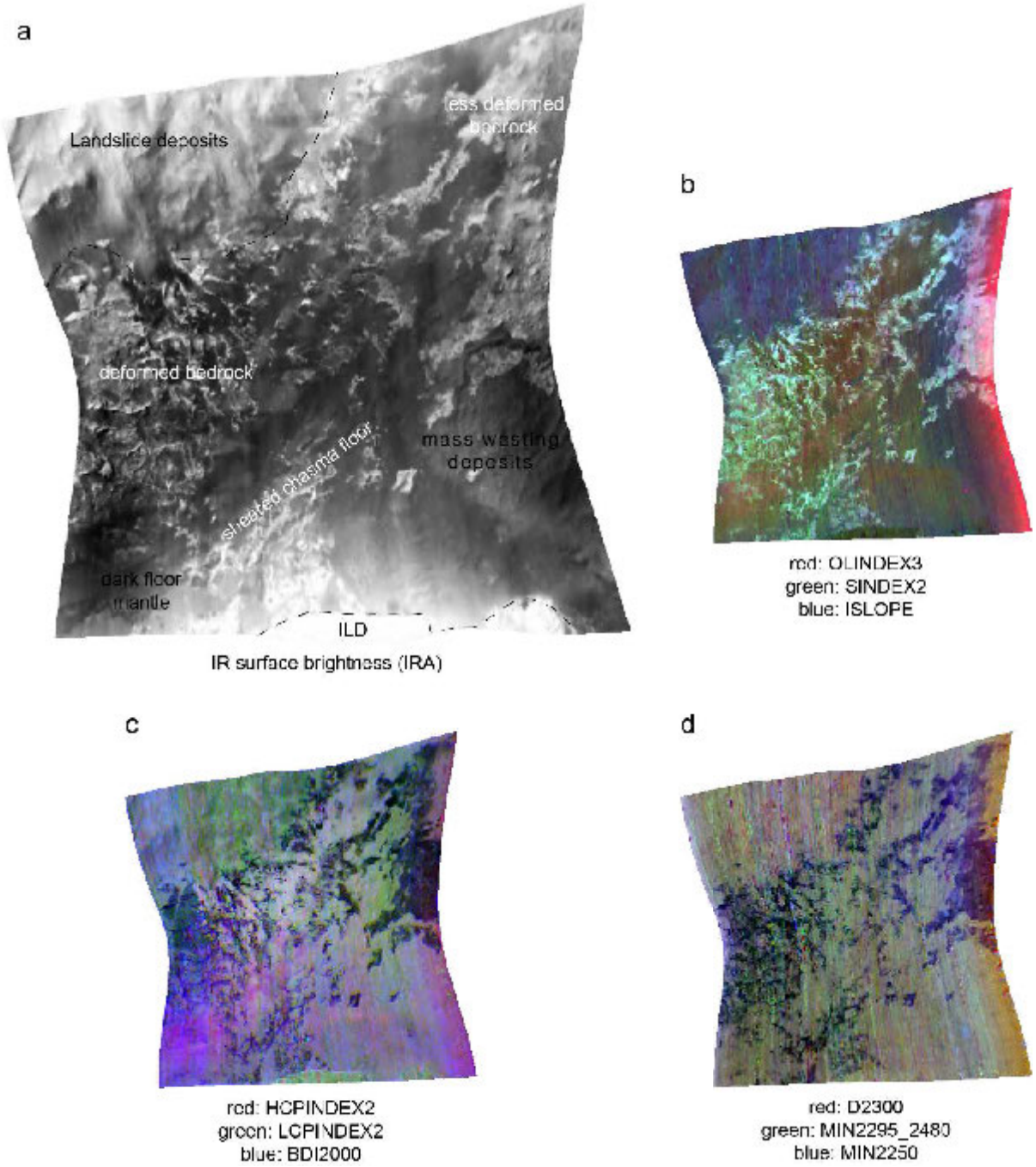

Supplementary Figure 18. Selected spectral indices applied to the CRISM cube FRT00018b55: (a) rough location map of the main geological units, based on geomorphological and structural analysis; (b) olivine (red), hydrated sulfates (green), and ferric coatings on dark rock (blue) are expected to be important contributors to the signal; (c) pyroxene (red), and specifically, high-Ca (green) and low-Ca (blue) pyroxene are not detected; (d) hydroxylated Fe,Mg silicates (mainly phyllosilicates, red), Mg-carbonates (green), and opal (blue) are not detected; (b) to (d): see more detailed description and caveats of mineral identification for these indices in Supplementary Table 3. Credit: CRISM data: NASA/Johns Hopkins University Applied Physics Laboratory.

2. Spectral unmixing

2.1. Spectral libraries

The spectra used to build input spectral libraries were collected from the following spectral libraries:

- USGS[36]
- CRISM[37]
- ECOSTRESS[38,39]
- RELAB[40]

Library #1 and **Library #2** are large libraries (33 and 58 minerals, respectively) used to seek the occurrence of the minerals potentially present in the HRSZ as from the previous works (Section 1.1), geomorphological and structural observations (Section 1.2), and the spectral indices (Section 1.3).

- **Library #1** includes the primary minerals of igneous rocks, as well as hydrated sulfates, following the main results from the previous works and the spectral index detections. From the geomorphology of outcrops (Section 1.2), the detected sulfates would be the product of magmatic rock alteration, rather than deposited sediments. Therefore, sulfates which are found in volcanic environments have been selected.
- **Library #2** extends Library #1 with minerals which are found in metamorphic rocks and in hydrothermal environments.

Library #3 is medium-sized (17 minerals) and narrows the previous libraries to the minerals that were detected using Libraries #1 and #2. Olivine, however, is removed in order to investigate the occurrence of minerals having a spectrum made difficult to detect by olivine masking. Three additional spectra were also added: basaltic glass, gypsum and opal.

- **Library #3a** (14 minerals) is a broad subsample of Library #3 which contains most of its minerals.
- **Library #3b** is small subsample (4 minerals) used to evaluate the possibility of an ILD-type sulfate composition, given that ILD are next to the HRSZ.
- **Library #3c** is another small subsample (4 minerals) used to evaluate a tonalitic composition for the HRSZ. Pyroxene is not included because its presence appears likely anyway from most experiments. Investigation of tonalite was justified by its light-tone color and structure, which match the HRSZ, and early planetary crust evolution (Archean, pre-plate tectonic terrestrial environment).
- **Libraries #3d** and **#3e** are small subsamples (3 and 2 minerals, respectively) designed to test the influence of kieserite in the unmixing.
- **Libraries #3f** and **#3g** (6 and 7 minerals, respectively) only differ by the presence or absence of olivine, and is used to evaluate the influence of olivine on masking plagioclases bands.
- **Libraries #3h**, **#3i**, and **#3j** (4, 5, and 4 minerals, respectively) are small subsamples designed to clarify the detectability of plagioclase versus olivine.

Library #4 is a medium-sized library (20 minerals plus water ice) designed to proceed toward final ROI mineralogical conclusions, building on the tests conducted in earlier experiments that used libraries 1-3.

- **Library #4a** (20 minerals) includes some minerals detected using Library #2 in the HRSZ, as well as a suite of mono- and polihydrated sulfates in order to determine whether additional sulfates are present in addition to the commonly detected kieserite and anhydrite and in some experiments, jarosite or coquimbite. **Library #4m** is equivalent of #4a, with thenardite removed. In **Library #4n**, both thenardite and biotite are removed. Library **#4c** (19 minerals) adds water ice to #4n.

- **Library #4b** (12 minerals) is a subset of Library #4a in which the primary minerals were removed, to determine whether the new sulfates still make them necessary.
- Library #4 is then subset to libraries customized to each of the three HRSZ ROIs. **Library #4d** (11 minerals) is a subset adapted to the positive and most potential detections so far in ROI1 and ROI3. **Libraries #4e-f** (10 minerals each) are two versions adapted to ROI2.

Library #5 includes only the minerals that have been detected using libraries #4d-f. **Libraries #5a-c** (7, 6 and 8 minerals, respectively) are individually designed for ROI1, ROI2, and ROI3.

2.2. Linear and nonlinear unmixing

A preliminary investigation was conducted in which mineral identification was done using linear spectral unmixing. Unmixing was done using the LinMin tool[41]. In the next, main step, a nonlinear unmixing was implemented (see the Methods section). Nonlinear unmixing allows to overcome discrepancies in grain size. For each experiment, linear unmixing was systematically run in addition to nonlinear unmixing.

2.3. Whole cube analysis

Whole cube analysis were done using spectral libraries #1, #2 and #3a (Supplementary Table 4). The overall conclusion of these experiments is that minerals of mafic or transitional rocks and sulfates are detected. Sulfate unmixing alone does not satisfactorily fit the measured spectra. A tonalitic composition can also be ruled out.

Experiment and Library used	Detections
C1 / Library #1 Primary minerals of volcanic rocks and sulfates as the potential products of alteration	Clinopyroxene (augite) and olivine, and kieserite.
C2 / Library #2 Library #1 plus metamorphic/hydrothermal minerals	The same as C1, but olivine dominates in all areas. No evidence of metamorphic rock mineralogy is found.
C3 / Library #3a Narrowed library	Clinopyroxene (augite), sulfates: hydrated (kieserite) and non-hydrated (anhydrite), in some areas accompanied by plagioclase (anorthite) and orthopyroxene (hypersthene).
C4 / Library #3b ILD mineralogy	Library narrowing to only sulfates worsens the fit between the modelled and measured spectra.
C5 / Library #3c Tonalite mineralogy	Anorthite is detected, but not the other minerals.

Supplementary Table 4. Whole cube analysis results

2.4. Regions of interest (ROI) investigations

2.4.1. ROI definition

Three samples of HRSZ on the floor of Ophir Chasma were studied. The averaged spectra of three ROIs are used as the input to the algorithm instead of individual pixels in order to minimize the noise level in experiments E1-47. The ROIs (Supplementary Figure 19) were defined using the following criteria:

- covered by CRISM cube FRT00018b55
- covered by at least one of the following HiRISE images: ESP_051999_1755, ESP_017754_1755, ESP_048518_1755, ESP_0160531755, ESP_039525_1755
- representativeness of HRSZ outcrops
- geomorphological homogeneity on HiRISE images as well as geographic extent
- large areal extent (number of CRISM cube pixels).

These exposures are light-toned and are distinguished from interior layered deposits (ILD) by the absence of layering and brittle intense fracturing. Their structure is reminiscent of some ancient terrains elsewhere on Mars, such as bedrock plains and some rocks exposed at central peaks[42,43].

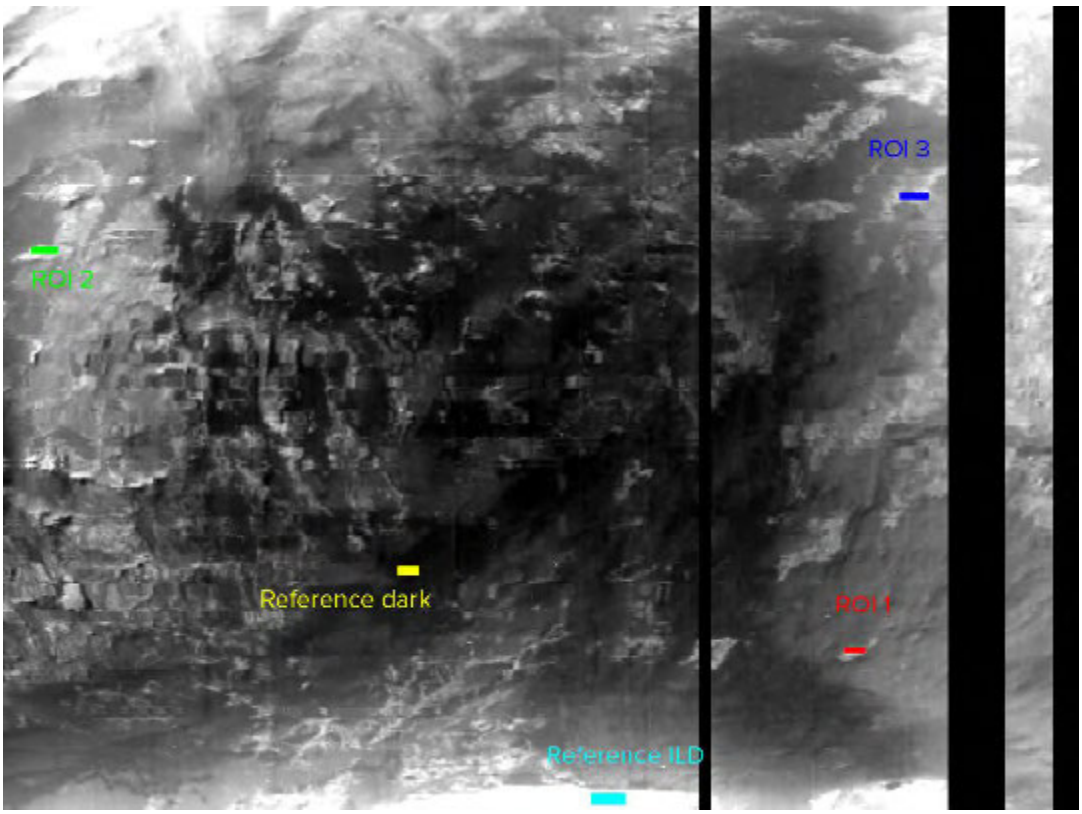

Supplementary Figure 19. Location of the three ROIs and the two reference areas on the non-projected CRISM cube FRT00018b55. ROIs size: ROI1 – 36 pixels, ROI2 – 60, ROI3 – 64, reference dark – 60, reference ILD – 133. North is toward the top. Black area corresponds to corrupted data. Credit: CRISM data: NASA/Johns Hopkins University Applied Physics Laboratory.

Two reference ROIs were defined (Supplementary Figure 19). First reference ROI was selected in the nearest ILD exposure in order to establish the spectral difference between ILD and the Ophir Chasma light-toned rocks, and investigate whether spectral ratioing of ROIs 1-3 by the ILD reference ROI improves the detections (Experiment E1i; Supplementary Figure 20, Supplementary Tables 5 and 6). Another reference ROI was selected in the dark flat areas surrounding HRSZ. If the dark material is polluting the full scene, one could reduce its contribution by ratioing ROI to the dark reference spectra (Experiment E1d; Supplementary Figure 20, Supplementary Tables 5 and 6). This strategy of ratioing was widely used to stress the faint spectral features (e.g., Bibring et al.[44]).

2.4.2. Atmospheric corrections

The standard volcano-scan approach has been used to correct for the gas absorption. We used the implementation of CAT 3. This approach is only performing a first order correction and some residues may be present. We also take into account the potential residue of atmosphere absorption by including an atmospheric gas absorption spectra from Douté et al.[45] in the unmixing libraries. Starting from Experiment E6 (Supplementary Figure 20, Supplementary Tables 5 and 6), atmosphere reference was changed to one from Planetary Spectrum Generator[46], but it did not improve results significantly.

Two flat levels added to the libraries account for surface albedo modification by aerosols. In half of the experiments two slopes spectra were added to the library, one negative and one positive, in order to possibly improve the aerosols modeling. Details are provided in Combe et al.[47], Schmidt et al.[41] and in the Methods section. The aerosol content of this particular CRISM cube (FRT00018B55) is estimated with 0.54 +/- 0.06 optical thickness of mineral aerosols and 0.27 +/- 0.05 optical thickness of water ice aerosols[48,49], which is low. According to the results presented in Figure 5 of Schmidt et al.[41], it should not significantly affect mineral detections.

2.4.3. Interpretation of unmixing results

For each experiment, apart from Experiment E1, results were obtained for linear and nonlinear unmixing. The spectral fit has always been significantly better with nonlinear experiments than with the linear ones, therefore the linear unmixing experiments are not discussed here.

Experiment justification, results, and other comments

Experiment description and purpose	Result
E1/Library #3a The HRSZ is located next to large ILD exposures and are surrounded by dark floor material. The first experiment was designed to determine first whether ratioing the HRSZ spectra with one of these potential spectral contaminants enhances the quality of the mineral detections. This was done by running Experiment E1 without ratioing (E1n), and by ratioing using the ILD (E1i) and dark material (E1d) reference areas.	Ratioing decreases the quality of the detections, as anticipated by Schmidt et al.[41].
E2-3/Library #3a Compared to E1n, E2 and E3 account for Mie scattering of aerosol particles in the atmosphere. E2 adds two flat levels to the library in order to correct for surface albedo modification by aerosols. E3 additionally includes a positive and a negative slope to take into account spectral slope continuum modification by aerosols[41,47]. Linear and nonlinear unmixing have been performed in parallel. Starting from E2, only results of nonlinear unmixing are given in Supplementary Table 6.	**Augite, anhydrite and kieserite are detected in all the ROIs.** Nonlinear unmixing yields better fit than linear unmixing. Accounting for both surface albedo and aerosol scattering effects and accounting for surface albedo effect only in the unmixing is not observed to yield significant spectral fit (RMS) difference.
E4/Library #3d; E5/Library #3e Following the results of E2 and E3, only the minerals that were systematically detected are switched on for detection in E4. Kieserite is one of the most commonly identified minerals in ILD, and might be present only in marginal abundance in the HRSZ, for instance due to aeolian dusting by the neighboring ILD. In order to determine how much kieserite is critical in the spectral mixture, it was removed in E5.	Comparison of E4 and E5 shows that all bands, including kieserite ones, are necessary to explain the observed spectra of the three ROIs. Adding more spectra improves the fit but also adds non-essential component. It is observed from the fit that there are still some important components missing,
E6/Library #3f; E7/Library #3g For improving the fit, plagioclases (2 anorthite and 1 oligoclase) and olivine spectra, were added to the minerals that were found dominant in the previous experiments. They were added gradually (olivine in E7), in order to evaluate the masking effect of olivine on plagioclase.	In the three ROIs, olivine is seen to mask plagioclases. The RMS of the spectral fit is higher in the case of plagioclase and olivine than in the case of plagioclase alone, implying that all primary minerals: pyroxenes, plagioclases and olivine are necessary for better fit.
E8/Library #3h; E9/Library #3i The libraries used in E6-7 are modified so as to keep only that plagioclase among the three ones that were detected, to confirm the olivine masking effect.	E8-9 confirm the results obtained in E6-7.
E10/Library #3j By removing plagioclase from E9 library, it is investigated whether in the study area the fit is better with plagioclase and olivine, or with olivine alone.	Without plagioclase in the library, olivine detection itself, or augite (depending on the ROI), may questioned, without substantially affecting the RMS of the spectral fit.
E11/Library #3h; E12/Library #3i; E13/Library #3j E11-13 are equivalent of E8-10, except that Mie scattering of aerosol particles in the atmosphere is not taken into account.	The results are qualitatively similar to those obtained when aerosol particle scattering is taken into account (E8-10). However, not taking this effect into account systematically yields lower spectral fit RMS.
Olivine, plagioclase, pyroxene (augite) and sulfates (anhydrite, kieserite) are likely to be present in the study area.	
E14-15/Library #2 After identification of some major minerals in the series of experiments described above, the large library #2 is used to confirm their presence and constrain the mineralogy of the HRSZ in more detail by diversifying the range of minerals potentially detected. E14 takes surface albedo change by aerosol particles into account, to which the scattering effect is added in E15.	In addition to olivine, augite and kieserite, already commonly detected in earlier experiments, coquimbite, and perhaps magnesite, are also detected. E14-15 allowed to notice local mineralogical differences between three ROIs, initially selected as representative of the same rock outcrop. Na plagioclase (albite) is detected in ROI2 only. Anhydrite is detected in ROI3, but not in ROI1 nor ROI2. Conversely, augite is detected in ROI1 and ROI3 only.

	The RMS of the spectral fits are good, which is interpreted as both a good understanding of the overall mineralogy, and an effect of the large number of spectra in the library.
E16, E18/Library #4b; E17, E19/Library #4a The content of the library was enriched by adding a suite of sulfates (mono- and polyhydrated) and several metamorphic rock minerals selected among ones used in previous libraries. Two concurrent HRSZ mineralogical compositions, one with the primary minerals of igneous rocks detected in earlier experiments (E17, E19), and one without them (E16, E18), are investigated. E18-19 take atmospheric scattering by aerosols into account, in contrary to E16-17.	It is possible to obtain a good spectral fit with and without primary minerals; however, primary minerals significantly increase the fit RMS. Whether atmospheric scattering by aerosols is accounted for does not yield any significant differences in the spectral fit; however, scattering modifies pyroxene and plagioclase detections in ROI1 and ROI3.
E21, E23/Library #4m E21 and E23 are equivalent of E17 and E19, except that thenardite (Na sulfate) is removed from the library, in the absence of an identified source of Na.	Comparison between E17, E19 and E21, E23 shows that thenardite removal from the library increases the detection of copiapite and coquimbite. Copiapite and coquimbite (Fe sulfates) are more likely to be present than thenardite, since in the HRSZ mineralogical context, it is easier to mobilize Fe than Na.
E24-25/Library #4n E24-25 are equivalent of E21 and E23, except that biotite is removed from the library. The shape of biotite and olivine spectra are close, and biotite has not been clearly observed so far in the unmixing spectra.	Removing biotite improves the positive detection of olivine in ROI1, and the RMS of the spectral fit. In ROI2 it does not change the list of positively detected minerals nor the RMS of the spectral fit, suggesting that it is not a significant component of the mixture.
E26-27/Library #4c E26-27 adds water ice to the previous experiment.	Water ice is not detected.
Libraries are shortened to the minerals that were positively or questionably detected in each ROI so far, in order to increase the accuracy of their spectral contribution. ROI1 and ROI3 share the same new library.	
E28-29/Library #4d/ROI1, ROI3	The minerals present in Library #4d of abundance <0.1%: anorthite, anhydrite, copiapite, and coquimbite (for ROI1), and augite and coquimbite (for ROI3) will be removed from the final library. In ROI3, with Library #4, hypersthene has been observed only, and consistently, when aerosol scattering correction is taken into account, suggesting a bias when applying this correction (see Section 2.4.2). Therefore, hypersthene is also removed from the final library for ROI3.
E30-31/Library #4e/ROI2	Similarly to E28-29, the following minerals present in Library #4e will be removed from the final library: anorthite, augite, anhydrite, and coquimbite.
E32-33/Library #4f/ROI2 In E32-33, kieserite is replaced by polyhalite in an effort to improve the fit in the spectral range around 1.5 µm, where the HRSZ has an absorption common to polyhalite but difficult to generate in mixtures that include kieserite.	The experiment was to test polyhalite instead of jarosite, but none of them is detected. Therefore, it does not add constraints to the determination of the mineralogy of the HRSZ.
Final mineralogical composition; the minerals of abundance <0.1% are removed from the libraries.	
E44/Library #5a/ROI1	Olivine, albite, augite, hypersthene, kieserite, szomolnokite, jarosite
E45/Library #5b/ROI2	Olivine, albite, kieserite, szomolnokite, copiapite, jarosite
E47/Library #5c/ROI3	Olivine, albite, anorthite, anhydrite, kieserite, szomolnokite, copiapite, jarosite

Supplementary Table 5. Spectral unmixing experiment justification and results

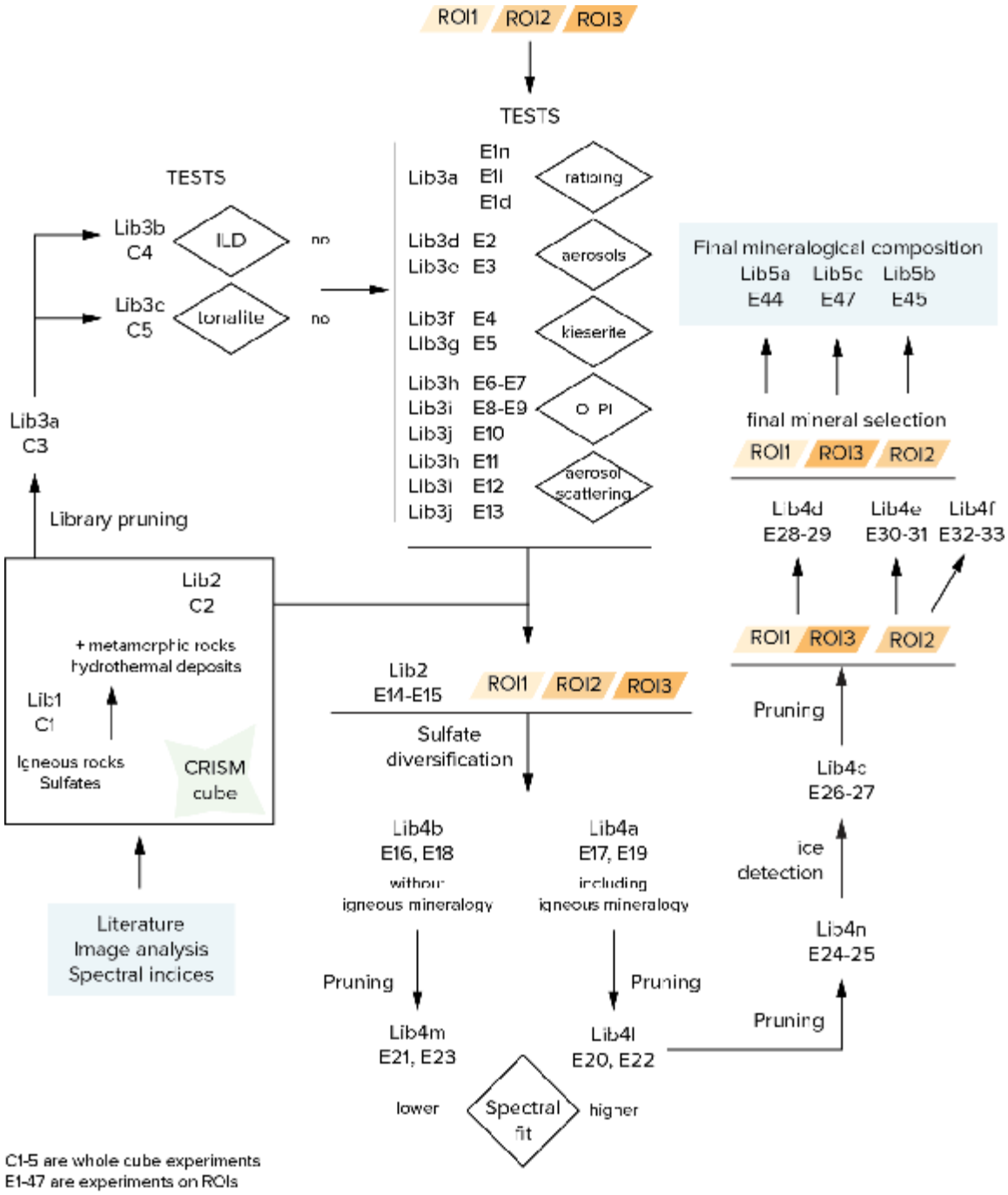

Supplementary Figure 20. Spectral unmixing flow chart

Plots and associated ancillary data (Supplementary Data 1[50])

The **mineral unmixing plots** provide the spectra of the minerals in the selected library that contribute by 0.1% at least to the modelled spectrum (plots include atmosphere absorption and if relevant, aerosol effects, in addition to mineral spectral abundance). In a given experiment, the modelled spectrum is the one that gives the best fit to the ROI spectrum, following the algorithm explained in the Methods section. The mineral unmixing plots also provide the ROI spectrum. The spectra shown on mineral unmixing plots are also provided as ASCII files.

The **spectral abundance plots** give the contribution of each mineral, the atmosphere, and aerosols, to the modelled spectrum. The numerical values of mineral abundances are provided as ASCII files.

The **best fit plots** provide the ROI spectrum and the output spectrum of the unmixing algorithm. The relative RMS is indicated.

Plot interpretation

In Supplementary Table 6**, a given detection is marked positive** when the spectral shape of a mineral on the unmixing plot is observed to significantly contribute to the modelled spectrum.

A detection is marked **questionable** in two cases. One is when the mineral spectrum is displayed on this plot but almost featureless, or is not seen to provide an unique contribution to the unmixed spectrum compared to other minerals. In the second case, its contribution to the modelled spectrum is less than 0.1% and the mineral is therefore not displayed on this plot, but its contribution on the spectral abundance plot is quantitatively seen to be distinctly higher than the minerals having a null contribution (0% or numerically very close to 0%).

A detection is marked **negative** when its contribution is null.

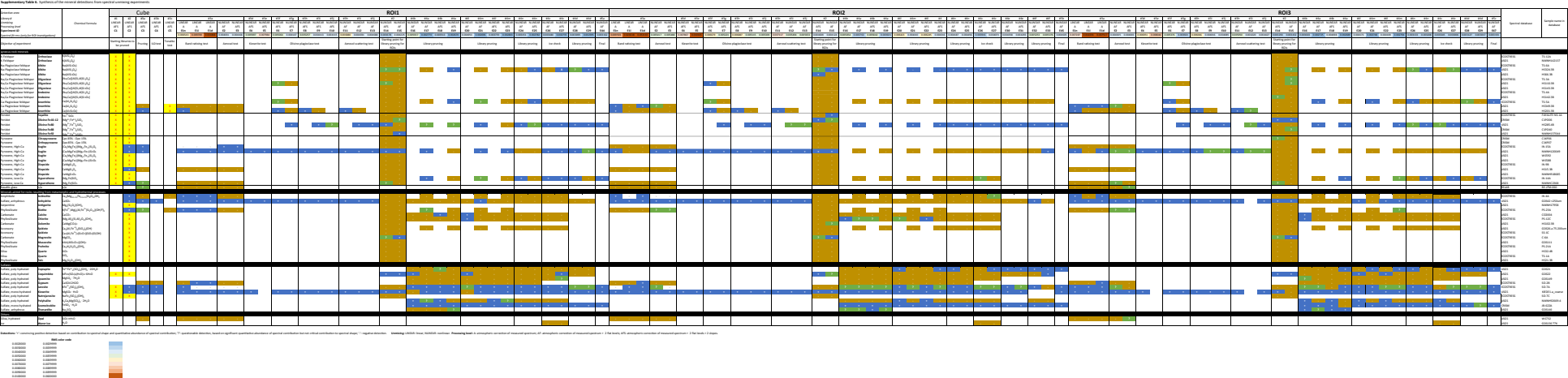

Supplementary Table 6. Synthesis of the mineral detections from spectral unmixing experiments

Detection area		Chemical formula	Cube					ROI1			Spectral database	Sample name in database
Library #			#1	#2	#3a	#3b	#3c	#3a				
Unmixing			LINEAR	LINEAR	LINEAR	LINEAR	LINEAR	LINEAR	LINEAR	LINEAR		
Processing level			AFS	AFS	AFS	AFS	AFS	A	A	A		
Experiment ID			**C1**	**C2**	**C3**	**C4**	**C5**	**E1n**	**E1i**	**E1d**		
Spectral fit rms (only for ROI investigations)								0.006543	0.009709	0.031868		
Objective of experiment			Starting libraries to be pruned		Pruning	ILD test	Tonalite test	Band ratioing test				
Igneous rock minerals												
K-Feldspar	**Orthoclase**	K(AlSi$_3$O$_8$)	x	x							ECOSTRESS	TS-12A
K-Feldspar	**Orthoclase**	K(AlSi$_3$O$_8$)	x	x							USGS	NMNH142137
Na-Plagioclase feldspar	**Albite**	Na(AlSi$_3$O$_8$)	x	x							ECOSTRESS	TS-6A
Na-Plagioclase feldspar	**Albite**	Na(AlSi$_3$O$_8$)	x	x							USGS	HS324.3B
Na-Plagioclase feldspar	**Albite**	Na(AlSi$_3$O$_8$)	x	x							USGS	HS66.3B
Na,Ca-Plagioclase feldspar	**Oligoclase**	(Na,Ca)[Al(Si,Al)Si$_2$O$_8$]	x	x							ECOSTRESS	TS-3A
Na,Ca-Plagioclase feldspar	**Oligoclase**	(Na,Ca)[Al(Si,Al)Si$_2$O$_8$]	x	x							USGS	HS110.3B
Na,Ca-Plagioclase feldspar	**Oligoclase**	(Na,Ca)[Al(Si,Al)Si$_2$O$_8$]	x	x							USGS	HS143.3B
Na,Ca-Plagioclase feldspar	**Andesine**	(Na,Ca)[Al(Si,Al)Si$_2$O$_8$]	x	x							ECOSTRESS	TS-4A
Na,Ca-Plagioclase feldspar	**Andesine**	(Na,Ca)[Al(Si,Al)Si$_2$O$_8$]	x	x							USGS	HS142.3B
Ca-Plagioclase feldspar	**Anorthite**	Ca(Al$_2$Si$_2$O$_8$)	x	x							ECOSTRESS	TS-5A
Ca-Plagioclase feldspar	**Anorthite**	Ca(Al$_2$Si$_2$O$_8$)	x	x	-		x	-	-	-	USGS	HS349.3B
Ca-Plagioclase feldspar	**Anorthite**	Ca(Al$_2$Si$_2$O$_8$)	x	x	+		x	+	-	-	USGS	HS201.3B
Peridot	**Fayalite**	Fe$_2^{2+}$SiO$_4$	x	x							ECOSTRESS	FAYALITE NS-1A
Peridot	**Olivine Fo10-12**	(Mg^{2+},Fe^{2+})$_2$SiO$_4$	x	x							CRISM	C1PO06
Peridot	**Olivine Fo80**	(Mg^{2+},Fe^{2+})$_2$SiO$_4$	x	x							USGS	HS285.4B
Peridot	**Olivine Fo88**	(Mg^{2+},Fe^{2+})$_2$SiO$_4$	x	x							CRISM	C1PO40
Peridot	**Olivine Fo92**	(Mg^{2+},Fe^{2+})$_2$SiO$_4$	x	x							USGS	NMNH137044
Pyroxene	**Clinopyroxene**	Cpx 85% - Opx 15%	x	x							CRISM	C1XP06
Pyroxene	**Orthopyroxene**	Opx 85% - Cpx 15%	x	x							CRISM	C1XP07
Pyroxene, High-Ca	**Augite**	(Ca$_x$Mg$_y$Fe$_z$)(Mg$_{y1}$Fe$_{z1}$)Si$_2$O$_6$	x	+	+			-	-	-	ECOSTRESS	IN-15A
Pyroxene, High-Ca	**Augite**	(Ca$_x$Mg$_y$Fe$_z$)(Mg$_{y1}$Fe$_{z1}$)Si$_2$O$_6$	x	+	+			+	+	+	USGS	NMNH120049
Pyroxene, High-Ca	**Augite**	(Ca$_x$Mg$_y$Fe$_z$)(Mg$_{y1}$Fe$_{z1}$)Si$_2$O$_6$	x	x							USGS	WS592
Pyroxene, High-Ca	**Augite**	(Ca$_x$Mg$_y$Fe$_z$)(Mg$_{y1}$Fe$_{z1}$)Si$_2$O$_6$	x	x							USGS	WS588
Pyroxene, High-Ca	**Diopside**	CaMgSi$_2$O$_6$	x	x							ECOSTRESS	IN-9B
Pyroxene, High-Ca	**Diopside**	CaMgSi$_2$O$_6$	x	+	-			-	-	-	USGS	HS15.3B
Pyroxene, High-Ca	**Diopside**	CaMgSi$_2$O$_6$	x	x							USGS	NMNHR18685
Pyroxene, Low-Ca	**Hypersthene**	(Mg,Fe)SiO$_3$	x	x							ECOSTRESS	IN-14A
Pyroxene, Low-Ca	**Hypersthene**	(Mg,Fe)SiO$_3$	x	+	?			-	-	-	USGS	NMNHC2368
Basaltic glass	n/a	n/a			?			-	-	-	RELAB	BE-JFM-060
Minerals added for rocks resulting from metamorphic and hydrothermal processes												
Amphibole	**Actinolite**	Ca$_2$(Mg$_{4.5-2.5}$Fe$_{0.5-2.5}$)Si$_8$O$_{22}$OH$_2$		+	-		-	+	+	+	ECOSTRESS	IN-4A
Sulfate, anhydrous	**Anhydrite**	CaSO$_4$		+	+	+		+	+	+	USGS	GDS42 <250um
Serpentine	**Antigorite**	Mg$_3$(Si$_2$O$_5$)(OH)$_4$		x							USGS	NMNH17958
Phyllosilicate	**Biotite**	K(Fe^{2+},Mg)$_2$(Al,Fe^{3+})Si$_3$O$_{10}$(OH/F)$_2$		+	?		-	+	+	+	ECOSTRESS	PS-23A
Carbonate	**Calcite**	CaCO$_3$		x							USGS	CO2004
Phyllosilicate	**Chlorite**	(Mg,Al)$_6$(Si,Al)$_4$O$_{10}$(OH)$_8$		x							ECOSTRESS	PS-12C
Carbonate	**Dolomite**	CaMg(CO$_3$)$_2$		x							USGS	HS102.3B
Accessory	**Epidote**	Ca$_2$(Al,Fe^{+3})$_3$(SiO$_4$)$_3$(OH)		x							USGS	GDS26.a 75-200um
Accessory	**Epidote**	Ca$_2$(Al,Fe^{3+})$_3$(Si$_2$O$_7$)(SiO$_4$)O(OH)		x							ECOSTRESS	SS-1C
Carbonate	**Magnesite**	MgCO$_3$		x							ECOSTRESS	C-6A
Phyllosilicate	**Muscovite**	KAl$_2$(AlSi$_3$O$_{10}$)(OH)$_2$		x							USGS	GDS111
Phyllosilicate	**Prehnite**	Ca$_2$Al$_2$Si$_3$O$_{10}$(OH)$_2$		x							ECOSTRESS	PS-21A
Silica	**Quartz**	SiO$_2$		x							USGS	HS32.4B
Silica	**Quartz**	SiO$_2$		x							ECOSTRESS	TS-1A
Phyllosilicate	**Talc**	Mg$_3$Si$_4$O$_{10}$(OH)$_2$		x							USGS	HS21.3B
Sulfates												
Sulfate, poly-hydrated	**Copiapite**	Fe^{2+}Fe$^{3+}_4$(SO$_4$)$_6$(OH)$_2$ · 20H$_2$O									USGS	GDS21
Sulfate, poly-hydrated	**Coquimbite**	AlFe$_3$(SO$_4$)$_6$(H$_2$O)$_{12}$·6H$_2$O	x	x							USGS	GDS22
Sulfate, poly-hydrated	**Epsomite**	MgSO$_4$ · 7H$_2$O									USGS	GDS149
Sulfate, poly-hydrated	**Gypsum**	CaSO4·2H2O			-	-		-	+	+	ECOSTRESS	SO-2B
Sulfate, poly-hydrated	**Jarosite**	KFe$^{3+}_3$(SO$_4$)$_2$(OH)$_6$	x	+	+	+		+	-	-	ECOSTRESS	SO-7A
Sulfate, mono-hydrated	**Kieserite**	MgSO$_4$ · H$_2$O	x	+	+	+		+	+	+	USGS	KIEDE1.a_coarse
Sulfate, poly-hydrated	**Natrojarosite**	NaFe$_3$(SO$_4$)$_2$(OH)$_6$	x	x							ECOSTRESS	SO-7C
Sulfate, poly-hydrated	**Polyhalite**	K$_2$Ca$_2$Mg(SO$_4$)$_4$ · 2H$_2$O									USGS	NMNH92669-4
Sulfate, mono-hydrated	**Szomolnokite**	FeSO$_4$ · H$_2$O									CRISM	JB-622A
Sulfate, anhydrous	**Thenardite**	Na$_2$SO$_4$									USGS	GDS146
Others												
Silica, hydrated	**Opal**	SiO$_2$·nH$_2$O			-			-	-	-	USGS	WS732
Ice	**Warer ice**	H$_2$O									USGS	GDS136 77K

Detections: '+': convincing positive detection based on contribution to spectral shape and quantitative abundance of spectral contribution; '?': questionable detection, based on significant quantitative abundance of spectral contribution but not critical contribution to spectral shape; '-': negative detection. **Unmixing:** LINEAR: linear; NLINEAR: nonlinear. **Processing level:** A: atmospheric correction of measured spectrum; AF: atmospheric correction of measured spectrum + 2 flat levels; AFS: atmospheric correction of measured spectrum + 2 flat levels + 2 slopes.

RMS color code		
0.0020000	0.0029999	
0.0030000	0.0039999	
0.0040000	0.0049999	
0.0050000	0.0059999	
0.0060000	0.0069999	
0.0070000	0.0079999	
0.0080000	0.0089999	
0.0090000	0.0099999	
0.0100000	0.0600000	

Supplementary References

1. Malin, M. C. et al. Context Camera Investigation on board the Mars Reconnaissance Orbiter. *J. Geophys. Res. Planets* **112**, E05S04 (2007).

2. Jiang, C., Douté, S., Luo, B. & Zhang, L. Fusion of photogrammetric and photoclinometric information for high-resolution DEMs from Mars in-orbit imagery. *ISPRS J. Photogramm. Remote Sens.* **130**, 418–430 (2017).

3. Fossen, H. *Structural Geology Ch. 15.1* (Cambridge University Press, Cambridge, 2010).

4. Cowie, P. A. & Scholz, C. H. Physical explanation for the displacement-length relationship of faults using a post-yield fracture mechanics model. *J. Struct. Geol.* **14**, 1133–118 (1992).

5. MacMillan, R. A. The orientation and sense of displacement of strike-slip faults in continental Crust. Unpubl. thesis, Dept. of Geology, Carleton University, Ottawa, 73 pp. (1975), reproduced in Ranalli, G. Correlation between length and offset in strike-slip faults. *Tectonophysics* **37**, T1–T7 (1977).

6. Fossen, H. & Cavalcante, G. C. G. Shear zones – A review. *Earth-Sci. Rev.* **171**, 434–455 (2017).

7. Andrews-Hanna, J. C., Zuber, M. T. & Banerdt, W. B. The Borealis basin and the origin of the Martian crustal dichotomy. *Nature* **453**, 1212–1215 (2008).

8. Christensen, P. R., Gorelick, N. S., Mehall, G. L. & Murray, K C. THEMIS Public Data Releases, Planetary Data System node, Arizona State University. http://themis-data.asu.edu (2006).

9. Tanaka, K. L. et al. Geologic Map of Mars. U.S. Geological Survey Scientific Investigations Map 3292, scale 1:20,000,000. https://dx.doi.org/10.3133/sim3292 (2014).

10. Schmidt, G., Fueten, F., Stesky, R., Flahaut, J. & Hauber, E. Geology of Hebes Chasma, Mars: 1. Structure, stratigraphy, and mineralogy of the interior layered deposits. *J. Geophys. Res. Planets* **123**, 2893–2919 (2018).

11. Gwinner, K. et al. The High Resolution Stereo Camera (HRSC) of Mars Express and its approach to science analysis and mapping for Mars and its satellites. *Planet. Space Sci.* **126**, 93–138 (2016).

12. Langlais, B., Thébault, E., Houliez, A., Purucker, M. E. & Lillis, R. J. A new model of the crustal magnetic field of Mars using MGS and MAVEN. *J. Geophys. Res. Planets* **124**, 1542–1569 (2019).

13. Mège, D. & Masson, P. A plume tectonics model for the Tharsis province, Mars. *Planet. Space Sci.* **44**, 1499–1546 (1996).

14. Mège, D., Cook, A. C., Garel, E., Lagabrielle, Y. & Cormier, M.-H. Volcanic rifting at Martian grabens. *J. Geophys. Res. Planets* **108**, 5044 (2003).

15. Huang, J. et al. Identification and mapping of dikes with relatively primitive compositions in Thaumasia Planum on Mars: Implications for Tharsis volcanism and the opening of Valles Marineris. *Geophys. Res. Lett.* **39**, L17201 (2012).

16. Brustel, C., Quantin, C., Flahaut, J., Michaut, C. & Davis, G. R. Valles Marineris tectonic and volcanic history inferred from dikes in eastern Coprates Chasma. *J. Geophys. Res. Planets* **122**, 1353–1371 (2017).

17. Mittelholz, A., Johnson, C. L., Feinberg, J. M., Langlais, B. & Phillips, R. J. Timing of the Martian dynamo: New constraints for a core field 4.5 and 3.7 Ga ago. *Sci. Adv.* **6**, eaba0513 (2020).

18. Andrews-Hanna, J. C. The formation of Valles Marineris: 2. Stress focusing along the buried dichotomy boundary. *J. Geophys. Res. Planets* **117**, E03006 (2012).

19. Mège, D. & Gurgurewicz, J. On Mars, location and orientation of dykes exposed along the Valles Marineris walls reveal expected and unexpected stress fields. *Acta Geol. Sin.-Engl.* **90**, 177-179 (2016).

20. Pilkington, M. & Hildebrand, A. R. Three-dimensional magnetic imaging of the Chicxulub crater. *J. Geophys. Res. Solid Earth* **105**, 23479–23491 (2000).

21. Hawke, P. J., Buckingham, A. J. & Dentith, M. C. Modelling source depth and possible origin of magnetic anomalies associated with the Yallalie impact structure, Perth Basin, Western Australia. *Explor. Geophys.* **37**, 191–196 (2006).

22. Abramov, O. & Kring, D. A. Numerical modeling of impact-induced hydrothermal activity at the Chicxulub crater. *Meteorit. Planet. Sci.* **42**, 93–112 (2007).

23. Osinski, G. R., Spray, J. G. & Lee, P. Impact-induced hydrothermal activity within the Haughton impact structure, arctic Canada: Generation of a transient, warm, wet oasis. *Meteorit. Planet. Sci.* **36**, 731–745 (2011).

24. Witbeck, N. E., Tanaka, K. L. & Scott, D. H. Geologic map of the Valles Marineris region, Mars. U.S. Geological Survey Geologic Investigations Series, Map I–2010, scale 1:2,000,000. https://doi.org/10.3133/i2010 (1991).

25. Lucchitta, B. K. Geologic map of Ophir and central Candor Chasmata (MTM–05072) of Mars. U.S. Geological Survey Geologic Investigations Series I–2568, scale 1:500,000. https://pubs.usgs.gov/imap/i2568/ (1999).

26. Fortezzo, C., Gullikson, A., Huff, A., Platz, T. & Kumar, S. Geologic mapping of central Valles Marineris (CVM), Mars. https://astrogeology.usgs.gov/search/map/Docs/PlanetaryDataWorkshop/Presentations2017/Tuesday/Fremont/Fortezzo_PGM2017_CVM (2017).

27. Mège, D. & Bourgeois, O. Equatorial glaciations on Mars revealed by gravitational collapse of Valles Marineris wallslopes. *Earth Planet. Sci. Lett.* **310**, 182–191 (2011).

28. Gourronc, M. et al. One million cubic kilometers of fossil ice in Valles Marineris: relicts of a 3.5 Gy old glacial landsystem along the Martian equator. *Geomorphology* **204**, 235–255 (2014).

29. Christensen, P. R. et al. JMARS – A Planetary GIS. http://adsabs.harvard.edu/abs/2009AGUFMIN22A..06C (2009).

30. Malin, M. C. et al. The Mars Observer Camera. *J. Geophys. Res.* **97**, 7699–7718 (1992).

31. Chojnacki, M., Jakosky, B. M. & Hynek, B. M. Surficial properties of landslides and surrounding units in Ophir Chasma, Mars. *J. Geophys. Res. Planets* **111**, 1–17 (2006).

32. Ehlmann, B. L. et al. Identification of hydrated silicate minerals on Mars using MRO-CRISM: Geologic context near Nili Fossae and implications for aqueous alteration. *J. Geophys. Res. Planets* **114**, 1–33 (2009).

33. Pelkey, S. M. et al. CRISM multispectral summary products: Parameterizing mineral diversity on Mars from reflectance. *J. Geophys. Res. Planets* **112**, 1–18 (2007).

34. Salvatore, M. R., Mustard, J. F., Wyatt, M. B. & Murchie, S. L. Definitive evidence of Hesperian basalt in Acidalia and Chryse planitiae. *J. Geophys. Res. Planets* **115**, 1–16 (2010).

35. Viviano-Beck, C. E. et al. Revised CRISM spectral parameters and summary products based on the currently detected mineral diversity on Mars. *J. Geophys. Res. Planets* **119**, 1403–1431 (2014).

36. Kokaly, R. F. et al. USGS Spectral Library Version 7: Data Series 1035, 61 p. https://doi.org/10.3133/ds1035 (2017).

37. CRISM Spectral Library. https://pds-geosciences.wustl.edu/missions/mro/spectral_library.htm.

38. Baldridge, A. M., Hook, S. J., Grove, C. I. & Rivera, G. The ASTER spectral library version 2.0. *Remote Sens. Environ.* **113**, 711–715 (2009).

39. Meerdink, S. K., Hook, S. J., Roberts, D. A. & Abbott, E. A. The ECOSTRESS spectral library version 1.0. *Remote Sens. Environ.* **230**, 111196 (2019).

40. Milliken, R. The RELAB Spectral Library Bundle. https://doi.org/10.17189/1519032 (2020).

41. Schmidt, F., Legendre, M. & Le Mouélic, S. Minerals detection for hyperspectral images using adapted linear unmixing: LinMin. *Icarus* **237**, 61–74 (2014).

42. Rogers, A. D. & Nazarian, A. H. Evidence for Noachian flood volcanism in Noachis Terra, Mars, and the possible role of Hellas impact basin tectonics. *J. Geophys. Res. Planets* **118**, 1094–1113 (2013).

43. Rogers, A. D., Warner, N. H., Golombek, M. P., Head, J. W. & Cowart, J. C. Areally extensive surface bedrock exposures on Mars: Many are clastic rocks, not lavas. *Geophys. Res. Lett.* **45**, 1767–1777 (2018).

44. Bibring, J.-P. et al. Global mineralogical and aqueous Mars history derived from OMEGA/Mars Express data. *Science* **312**, 400–404 (2006).

45. Douté, S. et al. South Pole of Mars: Nature and composition of the icy terrains from Mars Express OMEGA observations. *Planet. Space Sci.* **55**, 113–133 (2007).

46. Villanueva, G. L., Smith, M. D., Protopapa, S., Faggi, S. & Mandell, A. M. Planetary Spectrum Generator: An accurate online radiative transfer suite for atmospheres, comets, small bodies and exoplanets. *J. Quant. Spectrosc. Radiat. Transf*. **217**, 86–104 (2018).

47. Combe, J. P. et al. Analysis of OMEGA/Mars Express data hyperspectral data using a Multiple-Endmember Linear Spectral Unmixing Model (MELSUM): Methodology and first results. *Planet. Space Sci.* **56**, 951–975 (2008).

48. Wolff, M. J. et al. Wavelength dependence of dust aerosol single scattering albedo as observed by the Compact Reconnaissance Imaging Spectrometer. *J. Geophys. Res. Planets* **114**, E00D04 (2009).

49. Wolff, M. J. et al. Mapping water ice clouds on Mars with MRO/MARCI. *Icarus* **332**, 24–49 (2019).

50. Gurgurewicz, J., Mège, D., Schmidt, F., Douté, S. & Langlais, B. Supplementary Data 1. https://gitlab.dsi.universite-paris-saclay.fr/frederic.schmidt/linearunmixing/-/tree/main/results (2022).

51. Williams, J. P., Paige, D. A. & Manning, C. E. Layering in the wall rock of Valles Marineris: Intrusive and extrusive magmatism. *Geophys. Res. Lett.* **30**, 1623 (2003).

52. Flahaut, J. et al. Pristine Noachian crust and key geologic transitions in the lower walls of Valles Marineris: Insights into early igneous processes on Mars. *Icarus* **221**, 420–435 (2012).

53. Viviano-Beck, C. E., Murchie, S. L., Beck, A. W. & Dohm, J. M. Compositional and structural constraints on the geologic history of eastern Tharsis Rise, Mars. *Icarus* **284**, 43–58 (2017).

54. Wendt, L. et al. Sulfates and iron oxides in Ophir Chasma, Mars, based on OMEGA and CRISM observations. *Icarus* **213**, 86–103 (2011).

55. Ding, N. et al. The central uplift of Ritchey crater, Mars. *Icarus* **252**, 255–270 (2015).